DOI:10.14753/SE.2014.1974

Atomistic Origins of Fracture Toughness of Bioactive Glass Cement During Setting

Ph.D dissertation

Tian Kun

Doctoral School of Clinical Medicine
Semmelweis University

Supervisor:	Dr. Dobó Nagy, Csaba, professor, Ph.D
Head of doctoral school of clinical medicine:	Dr. Varga, Gábor, professor, doctor of the HAS, Ph.D
Official reviewers:	Dr. Turzó, Kinga, associate professor, Ph.D Dr. Kellermayer, Miklós, professor, doctor of the HAS, Ph.D
Head of the final examination committee:	Dr. Hermann, Péter, professor, Ph.D
Members of the final examination committee:	Dr. Hegedűs, Csaba, professor, Ph.D Dr. Fábián, Gábor, associate professor, Ph.D

Budapest
2014

DOI:10.14753/SE.2014.1974

TABLE OF CONTENTS

DOI:10.14753/SE.2014.1974

DOI:10.14753/SE.2014.1974

DOI:10.14753/SE.2014.1974

ABBREVIATIONS AND SYMBOLS

ART	Atraumatic Restorative Treatment
ASPA	AluminoSilicate PolyAcrylic
ASTM	American Society for Testing Materials
BS	British Standard
CGIC	Conventional Glass Ionomer Cement
COO^-	Carboxylate Anion
CTS	Coherent Terahertz Spectroscopy
DFT	Density Functional Theory
DGDZVP	DGauss Double-Zeta Valence Polarization
DINS	Deep Inelastic Neutron Scattering
DSC	Differential scanning calorimetry
ENS	Elastic Neutron Scattering
FSDP	First Sharp Diffraction Peak
FTIR	Fourier Transform Infrared spectroscopy
GIC	Glass Ionomer Cement
HEMA	2-hydroxyethyl methacrylate
IA	Itaconic Acid and Impulse Approximation
ILL	Institut Laue Langevin
IR	Infrared spectroscopy
ISI	Institute for Scientific Information
ISO	International Organization for Standardization
KE	Kinetic Energy
KHN	Knoop Hardness Number
MAS	Magic Angle Spinning
MGA	Methacryloyl Glutamic Acid
NCS	Neutron Compton Scattering
NIMROD	Near and InterMediate Range Order Diffractometer
NMR	Nuclear Magnetic Resonance
NVP	N-VinylPyrrolidone
N/A	Not Available
OF	(Harmonic) Oscillator Frequency
PA	PolyAcid
PAA	PolyAcrylic Acid
PVPA	poly vinyl phosphonic acid
QO	Quasi-Optical
RMGIC	Resin Modified Glass Ionomer Cement
SANS	Small Angle Neutron Scattering
SEM	Scanning Electron Microscopy
SEN	Single-Edge-Notch test
SMI	Structure Model Index
TEM	Transmission Electron Microscope
TOF	Time Of Flight
VNA	Vector Network Analyzer
VOI	Volume of Interest

WANS	Wide Angle Neutron Scattering
XRD	X-Ray Diffraction
YAP	Yttrium Aluminium Perovskite
μCT	X-ray micro Computed Tomography
2-D	2 Dimensional
v	Poisson's ratio
K_C	Fracture toughness, also called critical stress intensity factor
Q	Magnitude of the momentum transfer vector of a scattered neutron
$F(Q)$	Total structure factor, used in neutron diffraction
$S(Q)$	Structure factor, is a mathematical description of how a material scatters
r	Displacement in SANS, also a symbol for inter-atomic distance/bond
$g(r)$	Total radial distribution function
$D(r)$	Differential pair correlation function
C_p	Isobaric (constant pressure) heat capacity
dB	Insertion loss (decibel) used in Thz spectroscopy, equivalent to intensity
T_g	Glass transition temperature
Δ	Delta, Greek letter, denotes change
d	Latin letter, denotes derivatives and differentials
pH	Is a measure of the acidity or basicity of an aqueous solution
$n(p)$	Momentum distribution
In situ	Latin for "in position," to examine the phenomenon exactly in place where
In vivo	Latin for "within the living," is experimentation using a whole, living
Pa	Pascal, pressure unit
Å	Angstrom, length unit, equals 10^{-10} meter
N	Newton, force unit
m	Meter, length unit; milli, unit prefix, 10^{-3}
m^2	Square meter, area unit
fm	Femto, unit prefix, equals 10^{-15}
μ	Micro, unit prefix, equals 10^{-6}
c	Centi, unit prefix, equals 10^{-2}
k	Kilo, unit prefix, equals 10^3
M	Mega, unit prefix, equals 10^6
G	Giga, unit prefix, equals 10^9
T	Tera, unit prefix , equals 10^{12}
eV	Electron volt, energy unit, the amount of energy gained (or lost) by the
V	Volt, unit for electric potential
%	Percentage sign, fraction of 100
sec/s	Second, time unit
min	Minute, time unit, equals 60 seconds
hr/h	Hour, time unit, equals 60 minutes
d	Day, time unit, equals 24 hours
m	Month, time unit, equals 30/31 days
Hz	Hertz, frequency unit, the number of cycles per second of a periodic
Amp	Ampere, electric current unit
L	Litre, volume unit
ppm	Parts per million, denotes one part per 1,000,000 parts

DOI:10.14753/SE.2014.1974

PREAMBLE

The history of implanting foreign materials into the human body can be traced back to ancient civilisations seeking replacements for missing or damaged teeth. The earliest known example for which there is firm archeological evidence involves endosseous implants dating back to ~600 AD [1] by the Maya [~2000 BC – 1697 AD]. These included fossils of human mandibles adorned with three tooth-shaped pieces of shell placed into the sockets of three missing lower incisor teeth. Further analyses showed effective and pronounced osseointegration (bone forming and fusing with the foreign material), providing evidence of the procedure being well optimised and widespread use geared to improving the quality of life of the population. Likewise, numerous samples dating to 7th century China have been recovered of teeth filled with a form of mercury-silver amalgam very similar to present day compositions. These examples are both preceded by Egyptian artifacts recovered from archaeological excavations at a Neolithic cemetery at Gebel Ramlah (on the western banks of the Nile river, at the Egyptian-Sudanese border), yielding shells carved to be identical in shape and size to a human tooth dating to ~3000 BC and intended to be used as a dental implant; although none were found implanted into bodies [2]. Similarly, ocular implants made of bitumen and dating back to ~2000 BCE have been found along the Iran-Afghan border, indicating that implanting was well-under way thousands of years ago, in many cultures worldwide.

As civilisations evolved and technology developed, more implants were created with differing functions, aiding recovery from injury or loss of other body parts (**Figure 1**). Often these materials were made from natural composites, including mollusk & sea shells, wood, ivory and animal horns. The industrial age gave way to inorganic and metallic materials being used more often as dental, bone and limb prosthetics. Synthetic polymers entered into use around the time of WWII, when supplies routes were cut to German dominated production of glassy ocular implants, with American production of acrylic-based ‘eyes’ filling the void. The 1950s through 1970s saw an explosion of metal-based implants (i.e. cochlear) and most recently, electronics and ‘meta-materials’ are becoming progressively more prevalent. These activities have given rise to an age of wide-acceptance of foreign materials in the body, so much so that non-essential implants (i.e. ‘piercings’) have become normality in fashion.

Ironically, and despite the developments of synthetic technologies over the past 50 years, state-of-the art implant and prosthetics based on natural materials are making a comeback. In many cases, natural composites (or analogue materials modeled on their composition and structures) are now characterised as providing the best compromise between desirable mechanical properties and biocompatibility, cost & aesthetics.

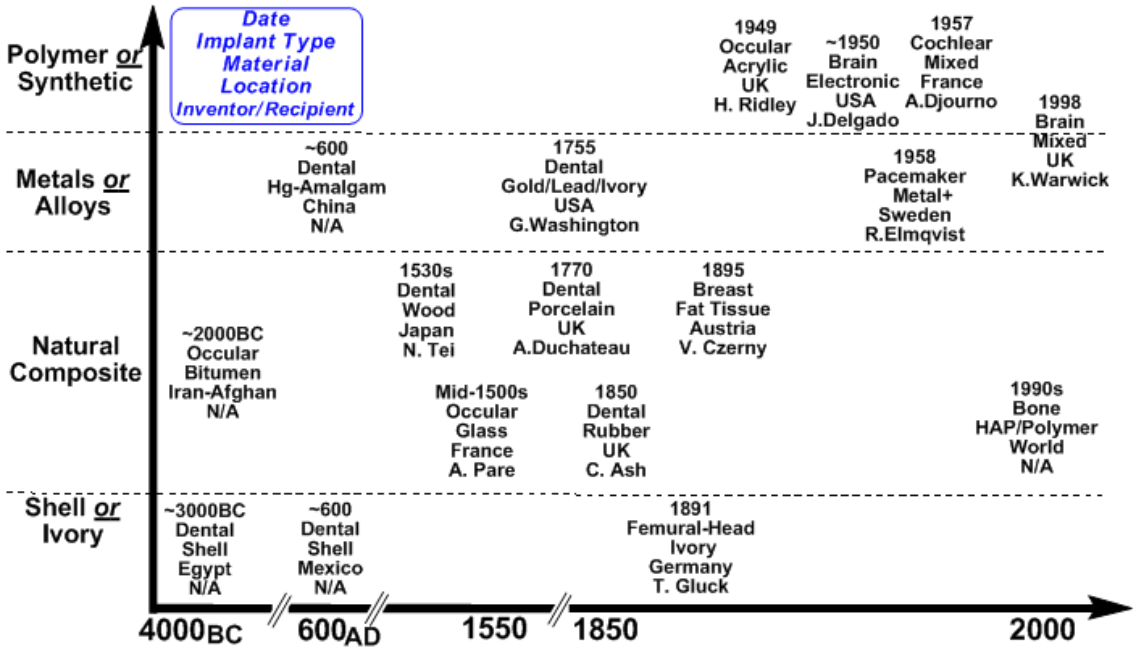

Figure 1 Timeline of the discovery and implementation of representative examples of the implanting of foreign materials into the human body.

Despite this ‘return to natural solutions’, demand for new medical and biomaterials with elevated longevities is accelerating through the ageing of the population and emergence of developing nations, outpacing the discovery, optimisation and development of novel solutions. As a discipline, dental materials science offers hope to help satisfy some of this demand. The ***implantation of foreign materials into the human body*** continues to be ***epitomised by dentistry***, which is by-far the ***historically most pervasive test-set***, with an extensive list of dental solutions being transferable to orthopedics and beyond.

However, ***the rational optimisation and design of tooth and bone replacements remains an unmet challenge***. Problems stem from the as-yet unresolved conflict between strength & toughness [3], with problems of adhesion, biocompatibility, appearance and cost beleaguering materials that do satisfy mechanical needs/thresholds.

One class of composite materials, Glass Ionomer Cements (GICs), also called glass polyalkenoate cements, show promise of resolving this material dichotomy.

GICs, the composite product of the acid-base reaction between an aqueous polymer acid solution and a basic glass powder [4], were first invented to serve as dental cements. They are widely used in dentistry [5,6] and have also been considered for use in bone [7,8] and ear reconstruction [9,10] as well as veterinary sciences [11,12] for their good biocompatibility and bioactivity [6,13] that stimulates tooth and bone remineralisation [14]. Their inherent adhesion to hydroxyapatite (the structural prototype of tooth and bone) and metal substrates [15,16], among other advantages [17,18], makes them almost ideal for these applications. Although the brittleness of these biocompatible composites has confined their use to non-load bearing applications for the past four decades, there is possibility that the brittleness be reduced.

Despite the potential of GICs to serve as a solution to several problems in materials science, and to provide helpful clues to optimise cements used in civil engineering (i.e. Portland cement), research focus and interest is turning away from these well-established materials. An ISI Web of Science search of the combined number of works containing the search string ‘glass AND ionomer’ was 1247, 1161, 1144 in the years 1996-2000, 2001-2005, 2006-2010, respectively (**Figure 2)**. This trend accelerated in 2011 and 2012 (latest values available to current-date), with only 214 and 216 ‘hits’, respectively, translating to a 5-year average of 1075. Although qualitative, this trend is unmistakable, showing dissemination plateauing, hence timing is optimal to introduce novel methods to optimising GICs.

DOI:10.14753/SE.2014.1974

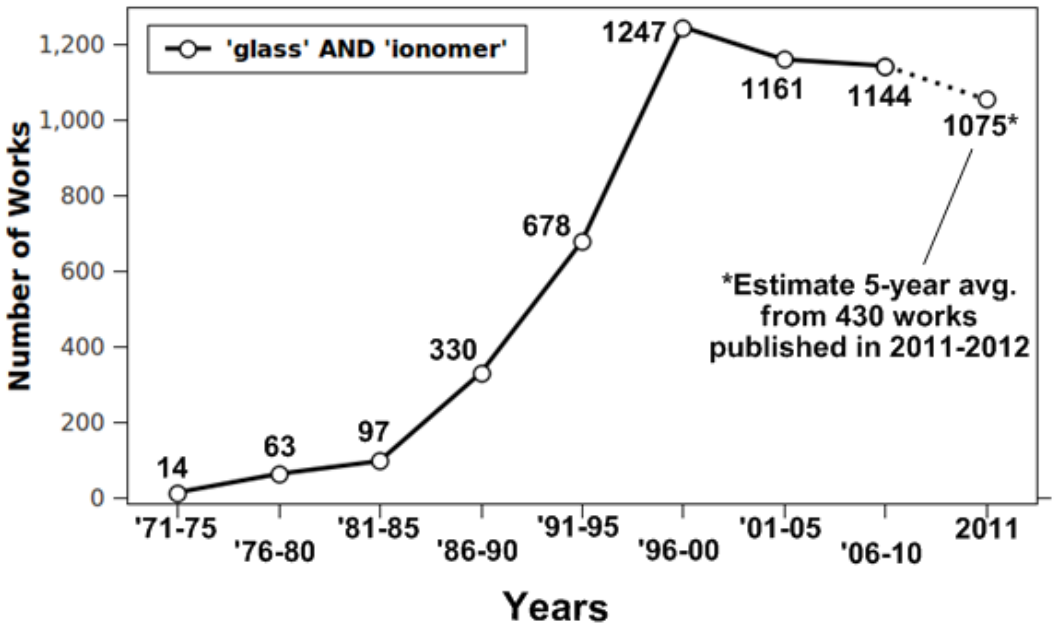

Figure 2 Number of works resulting from an ISI Web of Science search string 'glass AND ionomer', in selected year-groups from 1971 to present, showing a decline from 2001 onwards. Results from 2011-2012 are extrapolated to a 5-year average to match the other data.

DOI:10.14753/SE.2014.1974

1 INTRODUCTION

Dental materials science combines the physical, chemical and molecular sciences with medical technology, clinical practice and aesthetic surgery [19]. The practical requirements for direct restorative tooth and bone materials include mechanical, chemical and biological resilience, biocompatibility, in addition to less obvious demands such as working time (for manipulation) and optimal setting (hardening) profiles [19]. No material is perfect for meeting all these requirements.

Currently, the major classes of direct dental restorative materials are dental silver-mercury amalgam and composite resins. They each have their advantages, despite pronounced disadvantages (**Table 1**), for remaining the first choice worldwide as direct dental restorative materials. These materials suffer from high replacement rates due to an associated occurrence of secondary carries which is partially caused by poor marginal adhesion to tooth structure [13,20]. Thus, bases, liners and bonding agents need to be applied before they are put in place, reducing marginal leakage that leads to secondary carries, while also providing thermal insulation and protect the tooth pulp from the associated chemical stimulation.

Table 1. Advantages and disadvantages of dental silver amalgam and composite resins.

	Advantages	**Disadvantages**
Silver-Mercury amalgam	• high strength • high wear resistance • longevity	• poor aesthetics • corrosion • Hg toxicity (production, use, disposal) • strict cavity preparation
Composite resins	• colour (tooth like) • command set • does not require retentive features • insulates tooth from temperature changes	• strict manipulation technique • setting shrinkage • poor marginal adaptation • lack of chemical bonding to dentine and enamel • short lifespan

Amalgam’s detrimental mercury toxicity has led to a ban on its use according to the European Union's strategy for reducing global exposure to mercury and the signing of the Minamata Convention on Mercury.

DOI:10.14753/SE.2014.1974

One promising alternative to amalgam is Glass Ionomer Cements (GIC). GICs are also known as glass polyalkenoates. GICs are biocompatible [6,13] and chemically bond to tooth and bone structure as well as metal substrates via an ion-exchange layer [15-17]. A novel 'sandwich technique' that involves using GIC to replace dentine and composite resin to replace enamel, has shown satisfactory restorative results [6] and has helped expand GIC's application to load-bearing areas. GICs have also found applications outside dentistry.

Originally made for cementing dental prosthetics in 1972, GICs have found an increasing number of applications over the past four decades in dentistry, orthopedics and beyond.

Unless otherwise stated, all the GICs discussed and studied in this dissertation are Conventional GICs (CGICs), which are the original and unmodified form.

1.1 GIC applications

1.1.1 Dental applications

GICs' applications in dentistry include (**Figure 1.1**):

- *Erosion lesion restoration:* tooth erosion is efficiently restored with self-adhesive GICs with minimum cavity preparation [21].
- *Restorative material:* direct filling material for non load-bearing regions. The successful sandwich technique - a laminated restoration using GIC (to replace dentin) and composite resin (to replace enamel), is applied in load-bearing regions. This strategy combines the most favourable attributes of the two materials [21,22-27]. Numerous in vitro studies have reported improved resistance to microleakage and carie development with this technique [28-32].
- *Luting agents:* for luting crowns, bridges and orthodontic brackets [27,33-35].
- *Cavity lining and base material:* GICs insulate the pulp from temperature and chemical stimuli [36].
- *Core buildup material:* GICs are used in conjunction with endodontic posts taking advantage of their natural adhesion to dentine [37-39].

- *Pit and fissure sealants:* Long-term success with fissure sealing has been demonstrated using GICs [40].
- *Atraumatic restorative treatment (ART):* ART is developed for use in developing countries where reliable electricity is not available for dental drills to operate. ART involves the use of hand manipulated scoops to remove softened tooth tissue and subsequent placement of GICs [6,41]. Clinical outcome is overall successful with retention times of ~2-6 years [41-48].

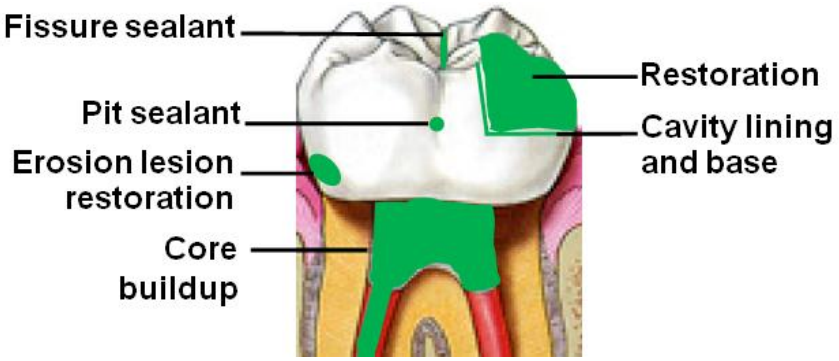

Figure 1.1 Illustration of dental applications for glass ionomer cements as fissure and pit sealants, erosion lesion restoration, core buildup, restoration, cavity lining and base.

- *Root canal filling material:* GICs have been advocated to serve as root canal filling material and subsequent *in vitro* studies have proved that they process adequate root canal sealing ability besides natural adhesion to root canal walls [49,50].

1.1.2 Applications outside dentistry

GICs have found applications outside dentistry, including:

- *Bone cement and bone implant material:* GICs can form a stable integration with bone, and affect the growth and development of bone through the ion release mechanism [7,8]
- *Otologic surgery and craniofacial reconstruction*: there have been successful clinical use of GICs as cochlear implant fixation, repair of the tympanic chain, eustation tube obliteration, ear ossicles and bone-substituted plates for craniofacial reconstruction [8-10]

- *ASPA splinting bandage:* water-hardening GIC is an alternative to plaster of Paris for rapidly developed strength and convenience of use [51].
- *Asbestos sealants:* GIC paste can serve as a cheap and effective asbestos surface sealant because it bonds to the mineral-containing dusts and prevents it from going into the air to cause health hazard [51].
- *Drug storage and osea-based delivery:* the inherent porosity of GICs allows for storage of ions and small molecules, both easily diffusing through and out of the composite matrix. Physical and chemical modification of the pore structure allows for modulation of diffusion and ultimately time-dependent release of such species from GICs placed in tooth or bone [51].

1.1.3 Potential applications

The continued drive to optimise GICs shows promise for replacing amalgam and resins as posterior filling materials if the current shortcomings can be overcome.

1.2 GIC Structure

1.2.1 Macroscopic structure

GICs are composite materials with a gel-like structure resulting from the reaction between an aqueous polyacrylic acid and a fluoroaluminosilicate glass powder (Al_2O_3-SiO_2-CaF_2). The irregularly shaped unreacted glass cores act as fillers embedded in the gel matrix. The matrix is composed of precipitated polyacrylate salts (**Figure 1.2**).

1.2.2 Mesoscopic structure

On the meso-scopic level, GICs consist of unreacted glass cores sheathed with silica gel, embedded in the matrix of cross-linked aluminium and calcium polyacrylate salt gel [51,52]. Silica gel and aluminium phosphate (when there is phosphorus in the glass) form an inorganic network (**Figure 1.2**) [53,54].

DOI:10.14753/SE.2014.1974

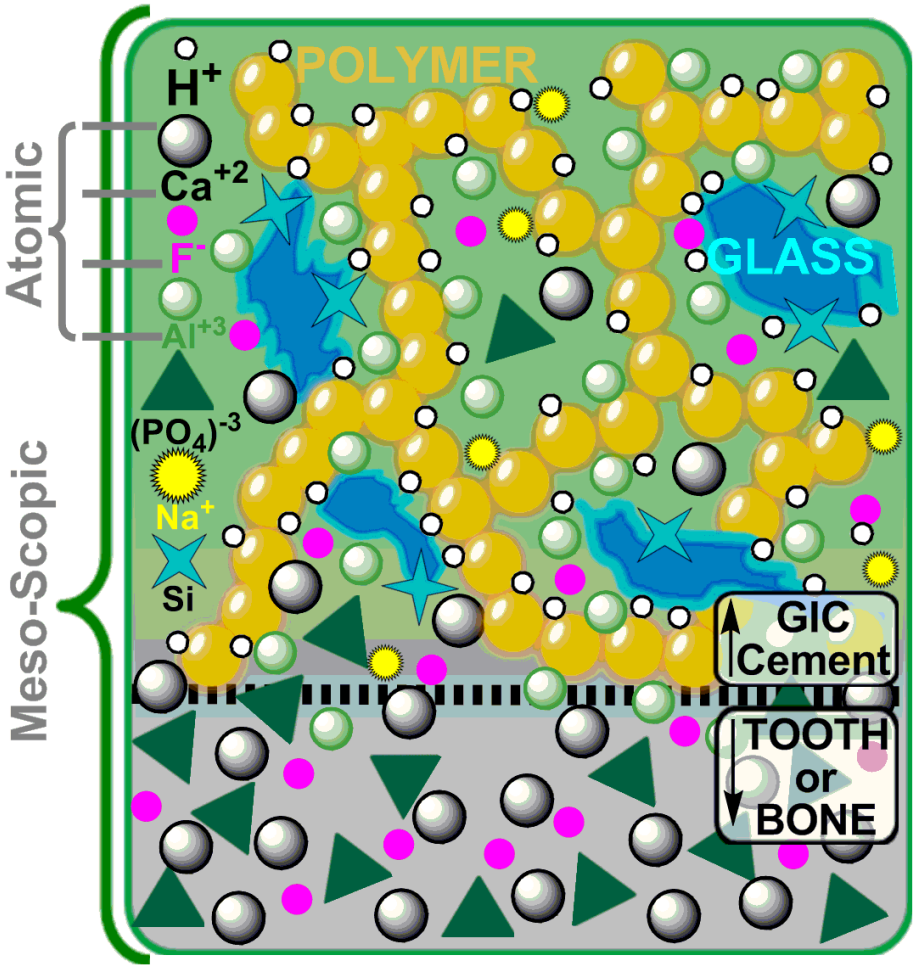

Figure 1.2 Qualitative representation of the meso- through micro-scopic structure of GIC as well as the interface between GIC and tooth/bone. On the meso-scopic scale, the cement is composed of precipitated polyacrylate matrix and glass particle fillers (irregular blue shapes) sheathed with silica gel (light blue).On the micro-scopic scale, the matrix is composed of precipitated polyacrylates formed by polymer chains (yellow bubble chains dotted with white spheres representing H^+) chelating Ca^{2+} (grey) and Al^{3+} (green). The bottom part below Interface (black vertical lines) is tooth/bone consisting of Ca^{2+}, PO_4^{3-} as well as F^- and Al^{3+} which have diffused across the interface from GIC.

1.2.3 Microscopic (Atomic & Molecular) structure

On the micro-scopic (atomic) level, the matrix polyacrylate salt is formed by polymer chains chelating the aluminium and calcium cations. The glass filler-matrix interface is composed of salt bridges formed by surface aluminium cations cross-linking the –COOH groups from the acid polymer, with ligands (H_2O and F^-) coordinatively binding the cations. Fluorine may exist as AlF_2^+, AlF^{2+} and CaF^+ complexes [19]. Phosphorus may form aluminium phosphate ($AlPO_4$) and is evenly distributed throughout the matrix. Silica also forms an inorganic network (**Figure 1.2**) [53,54].

DOI:10.14753/SE.2014.1974

Wilson first proposed the possible molecular structures of the salt bridges in 1974 (**Figure 1.3**) [55]. Unfortunately, there has been no follow-up study nor any molecular modeling of the proposed salt bridge structures.

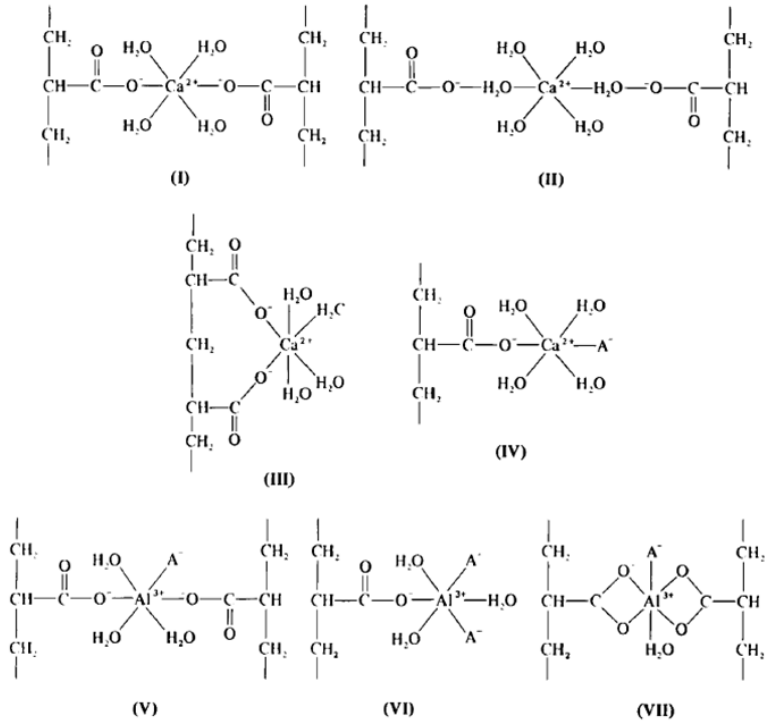

Figure 1.3 Possible molecular structures of the salt bridges proposed by Wilson [51,55]

1.3 GIC properties

1.3.1 Physical properties of GICs

1.3.1.1 Appearance

Fully set (hardened) GICs are translucent and similar to tooth color. Density is 2.4 g/cm^3, although they are porous with ~ 3% porosity [56,57].

1.3.1.2 Biocompatibility

GICs possess good biocompatibility. In vitro experiments with different cell culture showed that freshly mixed GICs were cytotoxic to the cells, although fully-set (hardened) GICs showed no detrimental biological effects [58-62]. Some human histological assessments showed evidence of moderate pulpal inflammatory responses

beneath GICs [63-65], while other comparable studies in primates showed either very mild or no inflammatory responses [58,62,66-68]. The gingival tissue response to cervical lesion restorations with GICs is minimal [69].

1.3.1.3 Adhesion

GICs are adhesive to tooth enamel (apatite), dentine (collagen) and base metals [70,71]. The adhesion to oxide surfaces is believed to be *via* hydrogen and metal ion bridges formed between carboxylate groups (COO^-) and oxygen anions [19]. The bonding to enamel and dentine is effected by the formation of a distinctive ion-exchange interfacial region few micrometers (μm) thick (**Figure 1.4**) with long-term durability [72]. Bonding to tooth is also effective when the tooth surface cannot be thoroughly dried to avoid danger of damage to the tooth structure. This is achieved by hydrogen bonding between tooth and free acid groups of GICs which replaces water molecules and ensures intimate contact [51].

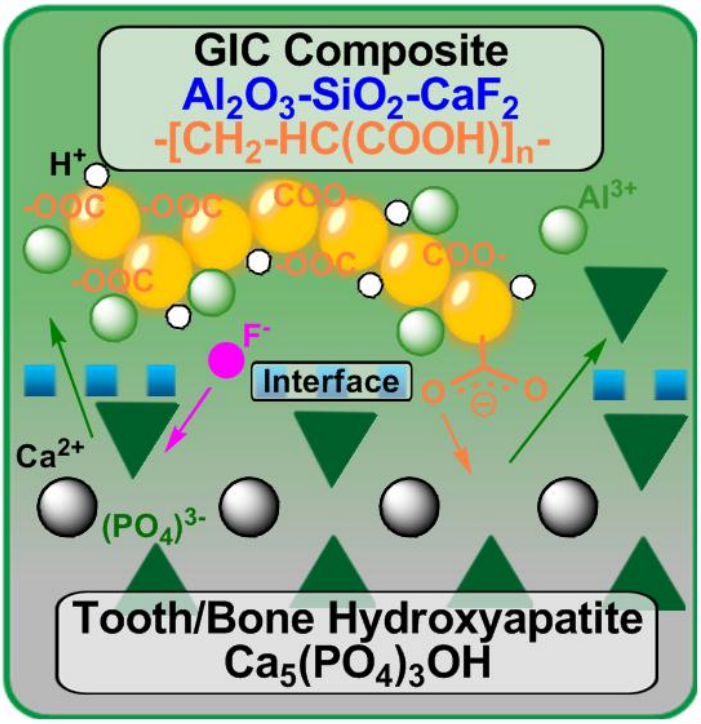

Figure 1.4 Illustration of ion-exchange interface between GIC and tooth/ bone (hydroxyapatite). The bright yellow bubble chains represent the acid polymer chains. Colored spheres represent H^+ (white), Ca^{2+} (grey), F^- (magenta) and Al^{3+} (green). The green triangles are PO_4^{3-}.

1.3.1.4 Ion release

GICs can buffer acids in the mouth and studies have shown that they can rapidly shift the pH of thin films of lactic acid on the cement surface from 4.5 (equivalent to that of active caries) to 5.5 (equivalent to that of arrested caries) within 30 seconds [73]. This gives GICs cariostatic property. The buffering occurs with release of ions, i.e. Na^{+}, Ca^{2+}, Al^{3+}, F^{-} as well as Si and P species, some of which are useful in tooth remineralisation. Among the ions released, fluoride is especially useful as it has been proven to be the most effective agent in preventing (and in some cases reversing) the formation of dental caries [74]. Hence, clinical use of GICs are evidenced as having anticariogenic effect [75] moderated through continual fluoride-release targeting differing causes of caries-formation in the mouth [74,76,77] (**Figure 1.5**).

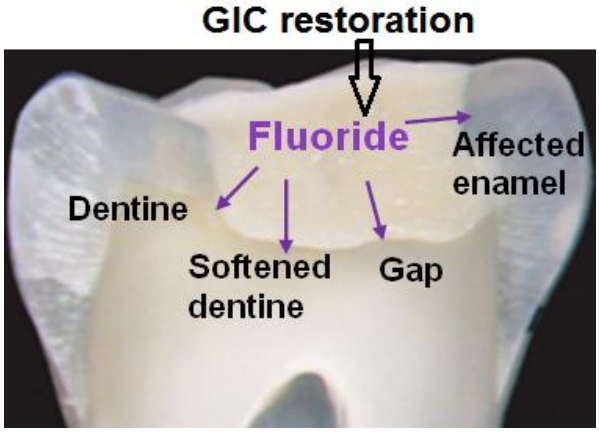

Figure 1.5 Fluoride released from a GIC restoration works on different targets around the restoration to achieve the anticariogenic effect.

1.3.2 Mechanical properties of GICs

Selected mechanical properties of GICs are as follows:

- *Modulus of elasticity*: ~ 7-18 GPa [78]
- *Poisson's ratio*: ~ 0.3 [79-81]
- *Hardness*: Knoop hardness 30 ~ 177 kg mm^{-2} [82]
- *Strength*: compressive strength of modern CGICs is 220~300 MPa [6]; tensile strength 11.7±1.5 MPa [83]; flexural strength ~ 54 MPa [84].
- *Fracture toughness*: 0.3~0.55 MPa $m^{0.5}$ [85].

Selected mechanical properties of oral tissues, amalgam, resin and CGIC [78,79-81,84-90] are reported in **Table 2** for comparison.

Table 2. Selected mechanical properties of human structural tissues and three classes of dental restorative materials.

Materials	Flexural strength/MPa	Fracture toughness/MPa $m^{0.5}$	Poisson's ratio	Modulus of elasticity/GPa
Bone	70-130	2.20-6.00	0.30	11
Dentine	17.5-18.9	1.60-3.10	0.29-0.45	12
Amalgam	30-90	0.96-1.60	0.35	30
Resin	85-92	0.70-1.83	0.35	10
Conventional GIC	7-54	0.30-0.55	0.30	15

It can be seen from **Table 2** that current GICs are inferior to amalgam and resin in flexural strength, fracture toughness and Poisson's ratio but are too rigid with highest modulus of elasticity. Improvement on material flexibility is needed.

Poisson's ratio v, the ratio between transverse strain (e_t) and longitudinal strain (e_l) in the elastic loading direction as $v = -e_t/e_l$ (**Figure 1.6**), has proved valuable as a criterion helping to distinguish brittle materials from ductile materials [91]. CGICs have Poisson's ratio of ~0.3 [80,81,85] while the successful dental amalgam has a value of ~0.35 [90] which is not significantly dfifferent from the average value of dentine [87]. Materials with higher Poisson's ratio will undergo more geometric change in the transvers direction to reduce stress localisation in the longitudinal direction.

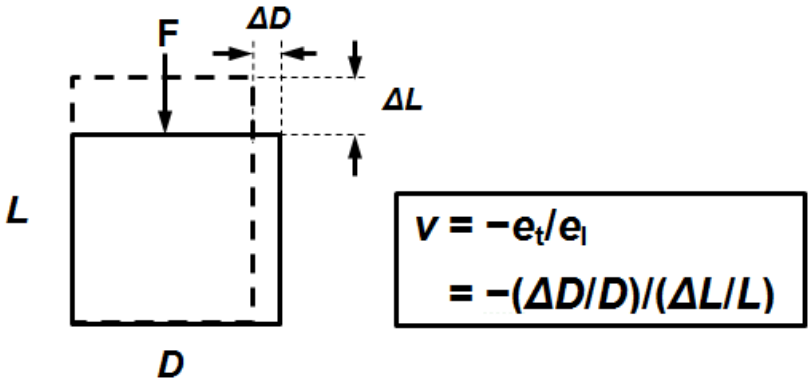

Figure 1.6 Illustration of Poisson's ratio: an object (rectangle in broken lines) under compression F, the transverse strain is e_t, longitudinal strain is e_l and Poisson's ratio $v = -e_t/e_l$.

Fracture toughness as a function of Poisson's ratio for several common classes of materials is tabulated in **Figure 1.7**. Poisson's ratio ν affords a sharp distinction in terms of fracture toughness [91] - brittleness prevelant when $\nu \leq$ ~0.3 and ductility if $\nu \geq$ ~0.35, limits subtended by GICs and amalgams respectively. Like many cements, however, both dental composites start as slurries, for which Poisson's ratio ~0.5, ν falling as setting advances. This process eventually leaves GICs too brittle, but offers a receipt for mechanical improvement, if setting can be arrested before Poisson's ratio falls below 0.35.

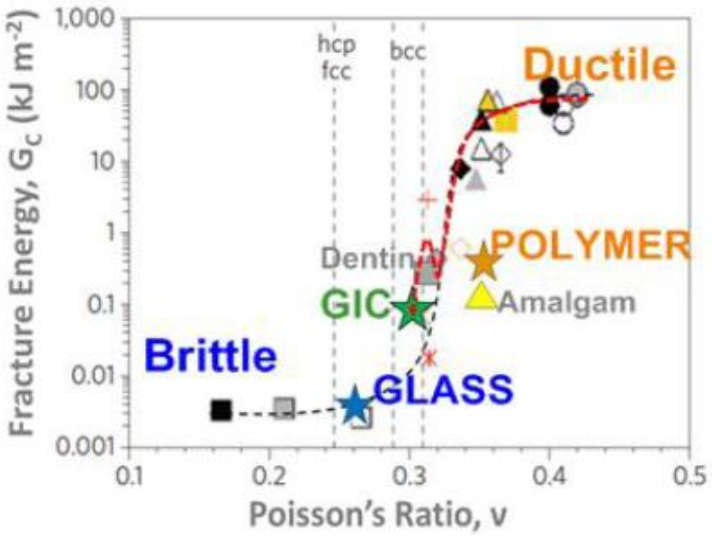

Figure 1.7 Fracture Energy G_C versus Poisson's ratio ν and the brittle-ductile transition, adapted for dental materials. The dashed arrow charts the decline in toughness between plastic slurry and rigid cement.

1.3.3 Changes in mechanical properties over time

The strengths of GICs rise continuously till after 24 hours, when most materials are considered to have reached a value close to their ultimate strength and are required to be tested according to British and International Standards [92]. However, some commercial materials exhibit significant increase of strength values after 24 hours [93].

Young's modulus of elasticity also increases with setting time [51].

The fracture toughness values for GICs in the literature were almost all measured at 24 hours after setting as recommended in the ISO specification 7489 (1986), when they are supposed to reach an initial strength peak. In the few studies that characterised early K_{IC}, the values at 5 hour are the same and even higher than the 24 hour value [94,95].

The only work that characterised Poisson's ratio over time showed that for two of the commercial cements there was a significant decrease in the values between 24 hours and 80 days [80].

There has not been enough data in the literature to construct a plot of fracture toughness as a function of Poisson's ratio in time domain like shown in **Figure 1.8** to help us understand how GIC's fracture toughness changes over setting time with Poisson's ratio being a pointer because *in situ* characterisation of the two parameters is very difficult and near impossible.

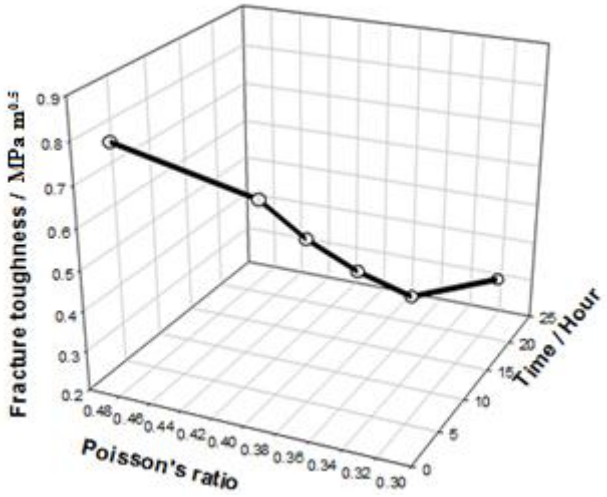

Figure 1.8 Example 3-D plot of fracture toughness as a function of Poisson's ratio and Time created for purpose of presentation.

1.4 GIC setting reactions (cementation)

1.4.1 Role of GIC powder

GIC powder acts as the proton acceptor and provider of silica for silica gel formation and cations for cross-linking the polyacid chains in cement formation. Alumina being more basic than silica, acid attacks preferentially the AlO_4 tetrahedral. Upon mixing the powder and liquid the hydrogen ions break the O-Al bonds. Al^{3+} and network dwelling cations (Ca^{2+} and Na^{+}) are released into the reacting cement with the formation of silicic acids which subsequently polymerises to form silica gel ($Si(OH)_4 \bullet X(H_2O)$) on the surface of the unreacted glass cores (**Figure 1.9**). Free Ca^{2+} and Al^{3+} ions eventually

cross-link the polyacrylic acid chains to form polyacrylate salt matrix [51]. Only a fraction of the glass, approximately 10%, is consumed in the setting reactions. The rest of the glass particles remain and act as reinforcing fillers embedded in the matrix [6].

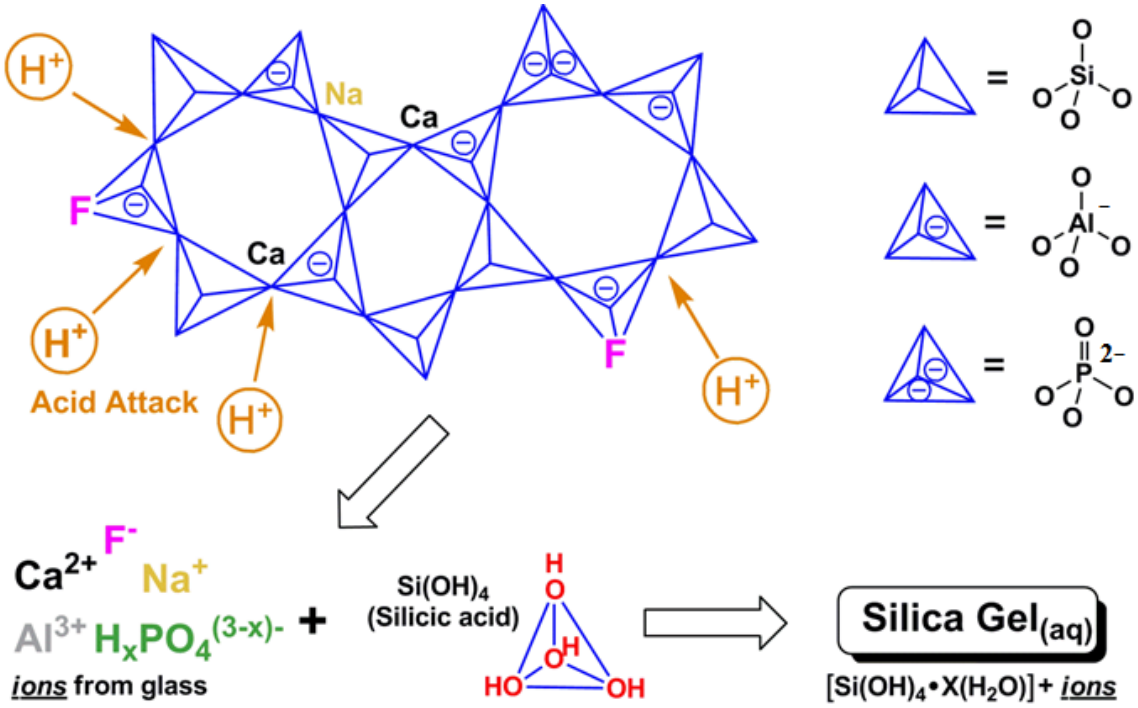

Figure 1.9 Illustration of acid attack on the glass component. H^+ (orange circle) from polyacrylic acid hydrolyses the AlO_4 tetrahedral and resultsing in release of free ions: Ca^{2+}, F^-, Na^+, Al^{3+} and PO_4^{3-} as well as silicic acid. The silicic acid later polymerises to form hydrolised silica gel covering the surface of the unreacted glass particles.

Apart from the organic network of metal polyacrylates, the matrix also contains an inorganic network of pure silicate or a mixed silicate/phosphate interpenetrating with the organic one which is also the reaction product of the glass with the liquid [43,96].

1.4.2 Action of GIC liquid

GIC liquid acts as a proton (H^+) donor. It attacks the glass particles, preferentially at calcium-rich sites of the glass that has undergone phase separation [96] and liberates calcium, aluminium, sodium and fluoride ions that accumulate in the aqueous phase of the paste, existing possibly as fluoride complexes; and silicic acid that polymerises into silica gel [4,97,98]. The polyacrylic acid obtains negative charges and they unwind and extend driven by the repelling force between chains having negative charges. The polymer occupies more space in the reacting sol resulting in a viscosity rise. The

calcium concentration decreases as calcium cations bind the polyacrylic chains to form calcium polyacrylate which then precipitates causing the cement to set within 10 minutes [99]. Aluminium cations stay in the solution for a longer period and eventually form aluminium polyacrylate that precipitates causing further cement hardening and increase of strength.

1.4.3 Setting reactions

The setting reactions of GICs are complex and may vary with composition. In general, they are characterised as acid-base reactions between the liquid component and the glass component in which Ca^{2+} and Al^{3+} are released from the glass particle surface and cross-link the acid polymer into a network [51].

Setting of GICs contains three overlapping stages: 1. Decomposition of glass powder; 2. Gelation; 3. Long-term setting and hardening.

1. *Decomposition of glass powder*

Once the liquid and glass powder are mixed at ~ 1:3 (ml/g), the protons (H^+) from the acid diffuse to the glass surface and attack the non-crystalline part of the glass. Upon proton attack, the Al-O bonds of the glass break and the glass decomposes with the release of Al^{3+} and network dwelling cations, (e.g. Ca^{2+} and Na^+), silicate as well as F^-. Silicate promptly forms silicic acid which then later polymerises to form silica gel [51]. Contrary to previous belief [52], there is no sequential release of Ca^{2+} and Al^{3+} - these cations and other species are released at the same time from as early as ~ 1 minute into the setting paste, existing possibly as fluoride complexes [97]. This ion release is facilitated by the presence of tartaric acid which forms complexes with these ions [100]. The viscosity of the sol rises as the acid polymer chains undergo conformational change of uncoiling and chain extension due to the repelling force between the negatively charged carboxyl groups [51].

The setting reactions can be represented by the following equations [101]:

$$glass + H^+ \rightarrow Ca^{2+} + Al^{3+} + SiO_4^{4-} \quad \text{(Eq. 1.1)}$$

$$nSiO_4^{4-} + 4nH^+ \rightarrow (SiO_2)_n \bullet 2nH_2O \quad \text{(Eq. 1.2)}$$

DOI:10.14753/SE.2014.1974

2. Gelation

When the tartaric acid is fully reacted, the complexes decompose and Ca^{2+} and Al^{3+} are liberated back into the setting paste. Ca^{2+} cations diffuse faster than Al^{3+} because having lower charges they are less hydrolysed than Al^{3+} and form calcium polyacrylate salt gel first at ~ 5 minutes. Ca^{2+} cations show atmospheric binding where they interact electrostatically with the polyacid (PA) anions and are not bound to a specific site. On the contrary, Al^{3+} shows site binding where they diffuse into the ion-binding sites of -COO^- to form ion-pairs with the anions (**Figure 1.10**). The formation of aluminium polyacrylate salt gel is slower occurring at ~ 3 hours because each Al^{3+} cation needs to bind three carboxyl groups to satisfy the valence requirement. This kind of chelation also strengthens the ion-binding. Formation of calcium polyacrylate is believed to be the cause of the initial setting (gelation) of the cement [97].

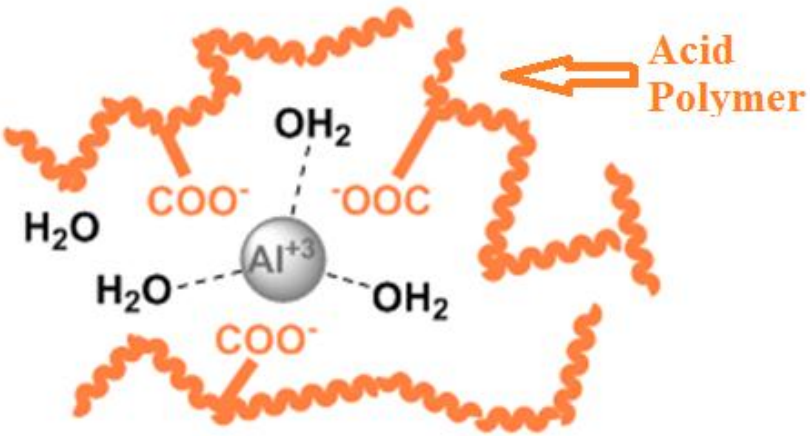

Figure 1.10 One postulated aluminium polyacrylate salt bridge structure formed as a result of the acid polymer (orange chains) chelating the Al^{3+} cations (grey sphere). Three water molecules may act as ligands to complete the VI-coordination.

The setting reactions can be represented by the following equations [101]:

$$Ca^{2+} + 2PA^{-} \rightarrow Ca(PA)_2 \qquad \text{(Eq. 1.3)}$$

$$Al^{3+} + 2PA^{-} \rightarrow Al(PA)_2^{+} \qquad \text{(Eq. 1.4)}$$

Ca^{2+} and Al^{3+} in aluminosilicate cements are cations with a small ionic radius and high ionic potential. They can form chelates through coordination bonds and are known to have a network-forming (glass-forming) capacity [19].

DOI:10.14753/SE.2014.1974

The strength of the coordination bond is related to the cation field strength, *F* [101]:

$$F \propto \frac{z}{r^2} \qquad \text{(Eq. 1.5)}$$

Where *z* is the charge; *r* is the ionic radius in nm.

For calcium, $F \propto 2/0.1^2 = 200$, and for aluminium, $F \propto 3/0.05^2 = 1200$. It is 6 times stronger for aluminium. Aluminium forming stronger and more stable chelates than calcium, they may even displace calcium [101].

$$Ca(PA)_2 + Al^{3+} \rightarrow Al(PA)_2^{+} + Ca^{2+} \qquad \text{(Eq. 1.6)}$$

3. Long-term setting and hardening

The hardness and strengths of the cement continue to rise after 24 hours. Formation of aluminium polyacrylate gel is responsible for this. As the cement hardens, the diffusion of Al^{3+} gets slower and it takes longer for new aluminium polyacrylate to form. It was found that the strength increased continuously for six months [93].

Secondary reactions: studies have shown that silicon and phosphorus are distributed throughout the metal polyacrylate gel binding matrix [99]. There are other secondary reactions contributing to matrix formation and cement hardening: the formation of silica gel and aluminium phosphate gel when there is phosphate in the glass [93,102].
This is represented with equation [101]:

$$Al^{3+} + PO_4^{3-} \rightarrow AlPO_4 \qquad \text{(Eq. 1.7)}$$

The setting reactions are illustrated in **Figure 1.11**.

However, the generality of the above setting reactions is not capturing the atomic scale details, especially of the Al-coordination evolvement, required to effect a full and rational optimisation of mechanical properties of GICs.

It is attempted here to describe the setting reactions in a step-wise fashion (**Figure 1.12**), paying attention to the atomic scale details and keeping in mind that the steps may overlap with the assigned time scale.

DOI:10.14753/SE.2014.1974

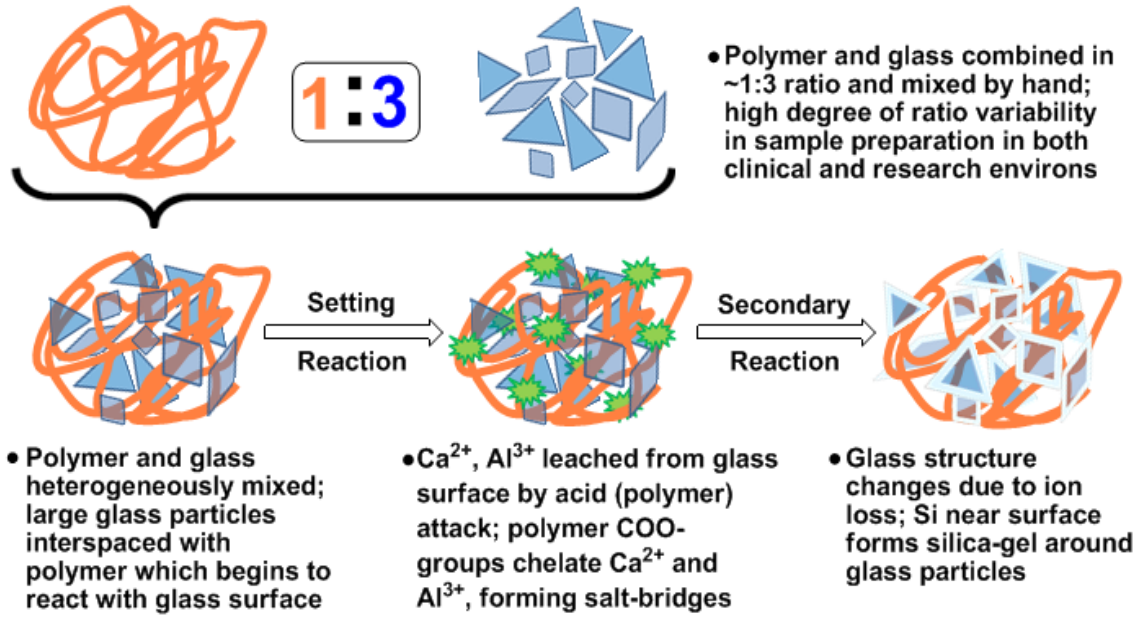

Figure 1.11 Illustration of general aspects of GIC setting (cementation) reactions.

Upon mixing, the H^+ from the acid polymer hydrolyses the surface of the glass particles resulting in the break-down of the glass structure with release of Al^{3+}, Ca^{2+}, Na^+, F^-, and PO_4^{3-} into the reaction paste in ~ 1 min. Ca^{2+} is chelated by the COO^- groups forming calcium polyacrylate salt which promptly precipitates causing the hardening of the paste within 0.1 hour. At up to ~ 3 hours Al^{3+} starts to cross-link the polymer chains forming Al(IV) coordinates with F^- and H_2O being possible ligands. After the glass structure breaks down the Si forms silicic acid. The Al(IV) coordinates then converts to more highly complexed Al(V) coordinates. Silicic acid polymerises to form silica gel on the glass surface. The cement hardens further. At ~ 12 hours Al(VI) coordinates form complexing more ligands which form stronger interfacial bonding between the glass particles and cement matrix (**Figure 1.12**).

DOI:10.14753/SE.2014.1974

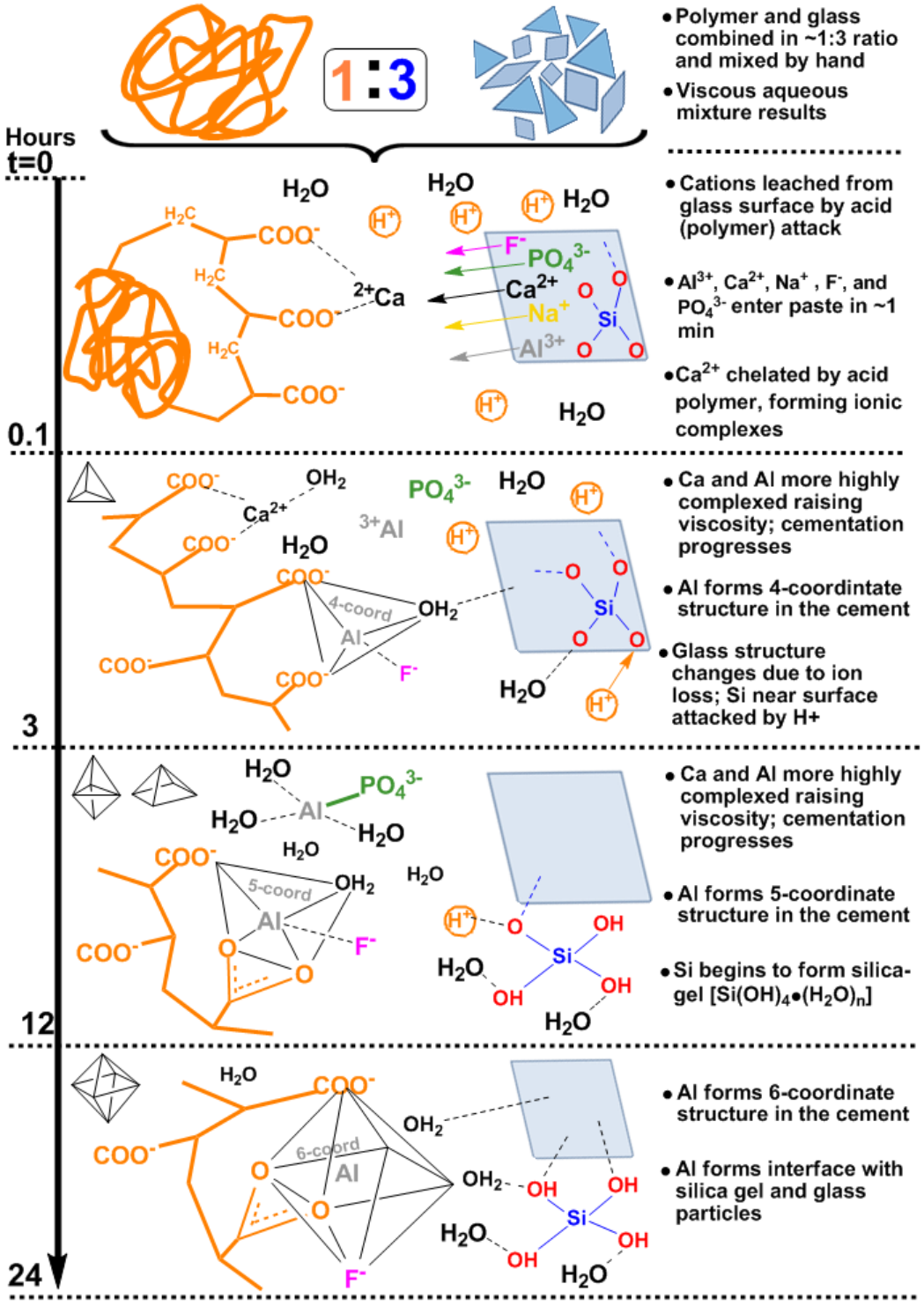

Figure 1.12 Illustration of the step-wise setting reactions of GICs showing the atomic scale details.

1.4.4 Role of water

Water plays important roles in GIC setting. Firstly, it dilutes the viscous acid into a flowable solution that facilitates convenient mixing with the glass powder and gives adequate working time. Secondly, it is the media for ion diffusion so the reactions can occur. The rheology of setting mixture remains low which does not limit ion mobility before the initial setting though hydration of aluminium cations slows down their diffusion. Thirdly, water plays a structural role in the cement formation in silica gel and the calcium and aluminium polyacrylates. This type of water is tightly bound to the cement and does not evaporate, thus it is called non-evaporable water. Opposite of it is evaporable water that can evaporate from the cement when the ambient humidity is lower than that inside the cement. As the cement ages the ratio of non-evaporable / evaporable water increases [96]. This ratio has been found to affect the mechanical properties of GICs and other dental cements: the compressive strengths are proportional to this ratio [78].

1.4.5 Role of fluorine

The concentration of the fluorine ions released affects the setting behavior of the cement: an increase in the concentration shortens the setting time and prolongs the working time. Glasses that contain no fluorine produce intractable cements. The possible mechanism is that fluorine ions complex the cations released from the glass and form AlF_2^+, AlF^{2+} and CaF^+ which aid their extraction and transport and also delays the formation of the polyacrylate salts [19,103]. Fluorine appears to strengthen the cement since the 24 hour compressive strength of fluorine-containing cement G278 is much higher than that of non fluorine-containing cement G241 (125 *vs* 74 N/mm^2) [51]. Fluorine content is also related to the fracture toughness of the cement, where the fracture toughness was increased dramatically at the expense of using low or fluorine free glasses [104].

1.4.6 Role of tartaric acid

The theory of the role of fluorine led to the search for other complexing agents to further improve the setting characteristics of GICs [105]. Among the agents studied, (+)-tartaric acid ($C_4H_6O_6$) (**Figure 1.13**) was the most effective one.

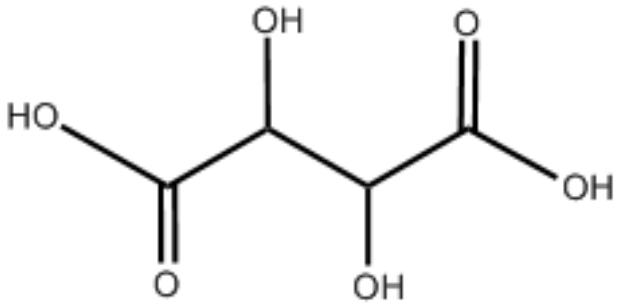

Figure 1.13 Molecular structure of tartaric acid ($C_4H_6O_6$).

The addition of tartaric acid in the liquid component produces cements with optimised setting behavior, i.e. adequate working time, sharp setting and improved strength. The effectiveness may result from the formation of tartaric-metal cation complexes that increases the cation release rate from the glass and delays the polyacrylate salt formation [106]. The difunctional tartaric acid may act as a bridge between the polyacrylic acid chains to increase the salt formation rate and help make stronger chelation [101]. Rheological studies showed that the action of (+)-tartaric acid on the setting reaction depended on its concentration. Low concentrations accelerated the development of viscosity of the cement paste, while high concentrations retarded it. At intermediate concentrations, (+)-tartaric acid first induced a lag period in the setting process during which the viscosity of the cement paste remained constant. This lag period was followed by a sharp, almost exponential, increase in viscosity (**Figure 1.14)**. Thus, (+)-tartaric acid was found to have a dual effect on setting, first inhibiting gelation and then accelerating it. The practical effect is to prolong working time for material manipulation and sharpen setting for short chair side time [106,107].

1.4.7 Role of phosphorous

Observation that P is present in the cement matrix of GICs supports the theory that aluminium phosphate also contributes to the cement hardening. Studies have shown that an increase in the $AlPO_4$ concentration increases the mobility (consistency spread), setting and working times. Cements prepared from glass that had no phosphate were difficult to mix, had very short setting and working times [96,108,109]. But this effect is dependent on the amount of phosphate: at low phosphate content, phosphate modifies the setting behavior; at high content, it disrupts the cross-linking process in the matrix

through competing with acid polymers in reacting with the metal cations resulting in reduced compressive strength and Young's moduli of elasticity [109]. High phosphorous content creates more Al-O-P bonds in the glass and does not dissolve as readily or favor the release of Al^{3+} than Ca^{2+} as does the low phosphate containing glass [110].

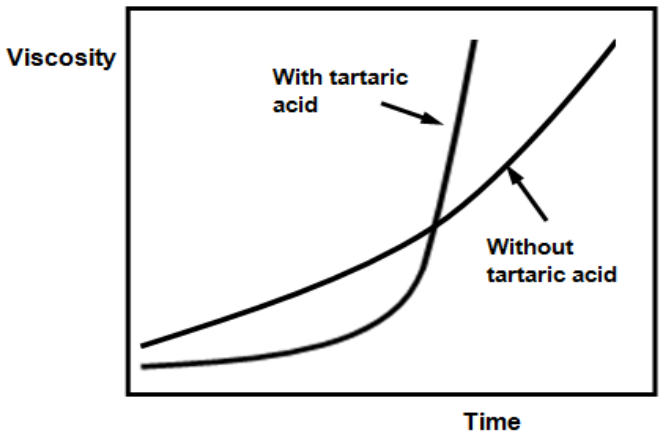

Figure 1.14 Qualitative representation of the change of viscosity for a setting GIC with and without tartaric acid. Without tartaric acid the viscosity rises fast but it takes long to reach the final set. The addition of tartaric acid delays the increase of viscosity so the working time is prolonged and it sharpens the setting.

1.4.8 Factors controlling reaction rate

There are three factors that control the cement-forming reaction rate [111]:

1. *The powder / liquid ratio*: The reaction rate is accelerated as this ratio is increased because of the greater specific surface area of powder per unit volume of paste.
2. *The acid concentration*: The speed of the cement forming reaction is accelerated as the concentration of the polyacid is increased.
3. *The viscosity of the liquid*: The reaction rate will be retarded by an increase in the viscosity of the liquid caused by an increase in the polyacid concentration.

At early stages of the reaction, the powder / liquid ratio alone governs the reaction rate – there is linear relation between the ratio and setting rate. The other two factors only affect reaction rate at later stages. At acid concentration below 38% w/w, an increase in acid concentration increases reaction rate; when concentration is increased from 38% to 43% w/w, setting rate is reduced; when concentration is further increased up to 48% w/w, setting rate increases again [111].

DOI:10.14753/SE.2014.1974

1.5 The components of GICs

Like all cements, GICs are produced from mixing the powder and liquid components.

1.5.1 The glass component

GICs employ ion-leachable calcium aluminosilicate glass characterised by high Al : Si ratio (~1:2) and high fluorine content up to 23% [45].

1.5.1.1 Synthesis

Mixture of SiO_2 and Al_2O_3 in a fluorite flux (CaF_2) is fused at pre-determined proportions in a sillimanite crucible at temperature 1100 - 1500 °C for 45 - 120 min. Other additives, e.g. $AlPO_4$, Na_3AlF_6 and AlF_3, are also used. The melt is poured onto a metal tray to cool to dull red heat, then plunged into a well of water and ground in a vibratory disc mill to a fine powder. The degree of fineness of the powder is controlled by the time of milling [112]. The powder is usually sifted through a sieve of 45 μm.

1.5.1.2 Composition

Typical glass compositions are shown in **Table 3** and the fraction of each element is shown in **Table 4**. G338 was discovered after G200 and is the glass powder commonly used in commercial products [96].

Table 3. Composition of glass G200 and G338, as wt. % prior to firing.

Component	G200	G338
Al_2O_3	16.6	14.3
SiO_2	29	24.9
CaF_2	34.2	12.8
AlF_3	5.3	4.6
$AlPO_4$	9.9	24.2
Na_3AlF_6	5	19.2

Only certain compositions (**Figure 1.15**) in the range have the necessary combination of properties. There must be sufficient alumina for the glass to be basic

enough to be susceptible to acid attack. However, too much of it results in the separation of Al_2O_3 as a separate phase (corundum) and this makes the glass opaque.

The advantages of using the fluorite flux include [112]:

- It reduces the fusion temperature;
- Makes a workable cement;
- Increases cement strength;
- It is the source of fluoride release which gives GICs anticariogenic characteristic;
- The presence of CaF_2-rich separated phase assists in creating the tooth-like optical properties of the set cement.

Table 4. Composition of typical glasses for glass ionomer cements, as at. %.

Element	G200	G338
Si	13.9	11.8
Al	13.4	16.9
Ca	17.6	6.6
F	20.1	19.7
Na	2.0	6.3
O	30.6	32.5
P	2.5	6.2

However, too much of fluorite makes the material opaque. A certain amount is required to give the opal appearance.

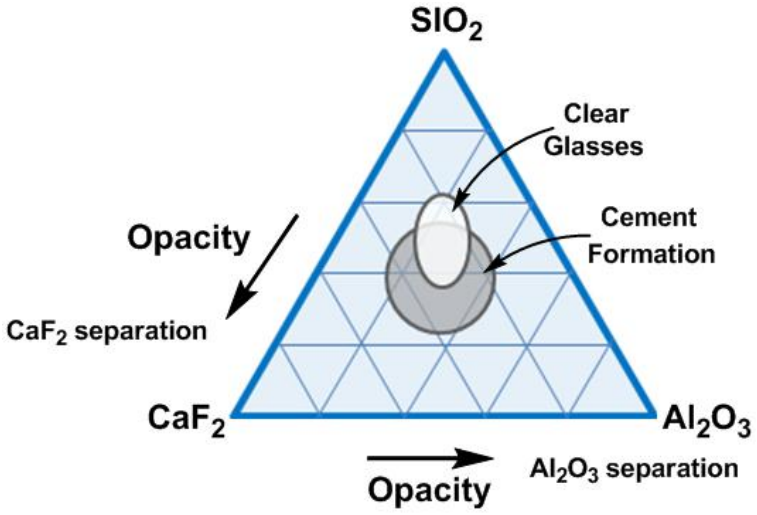

Figure 1.15 Region of Al_2O_3-SiO_2-CaF_2 glass that forms cement with polyacrylic acid on the phase diagram. The clear glasses are not satisfactory. Reproduced from [101].

1.5.1.3 Effect of particle size and distribution

Reduction in the median glass particle size improves compressive strength [113,114] and hardness [82]. It also assists the reduction in maturation time because the larger surface area for reactions will result in rapid set and less long-term degradation. Larger glass particle sizes and a more integrated microstructure contributed to a higher wear resistance [82]. And large particles produce cements of increased fracture toughness by deflecting cracks upon failure [115].

Optimising particle size distribution has been recognised as a route to improved mechanical properties [84] and clinical handling characteristics [116] which may enhance the longevity of the restoration. It was proved that powders with a bimodal particle size distribution, i.e. wide distribution of particle sizes with fine particles distributed among large particles, ensured a high packing density of GICs, leading to relatively high compressive strength [117].

1.5.1.4 Effect of alumina : silica ratio

The glass powder's reactivity depends on the ratio of alumina (basic) to silica (acidic): the basicity in the fusion mixture. An increase in the basicity of the glass will increase the setting reaction rate and shorten the setting time.

On the structural aspect, the glass can be considered as a silica network consisting of SiO_4 tetrahedral in which four-coordinated aluminium has partly replaced silicon forming Al-O-Si bonds (**Figure 1.16**). The aluminium acts as network-former. This replacement introduces more basicity and negative charge into the glass structure due to valence difference which is balanced by network-dwellers, i.e. Na^+ and Ca^{2+}. When these are not available, Al^{3+} may go into network-dwelling sites. When the Al_2O_3:SiO_2 ratio approaches unity, the glass structure acquires enough negative charges to become susceptible to acid attack at the Al^{3+} sites. This explains the decreased setting time when the Al_2O_3:SiO_2 ratio was increased up to 1. When the Al_2O_3:SiO_2 is further increased over 1, the excess Al^{3+} ions will go into network-dwelling sites increasing the resistance to acid attack while the network charge is not altered [112]. F may also break up the glass network by replacing bridging-oxygen and forming non-bridging fluorines [118].

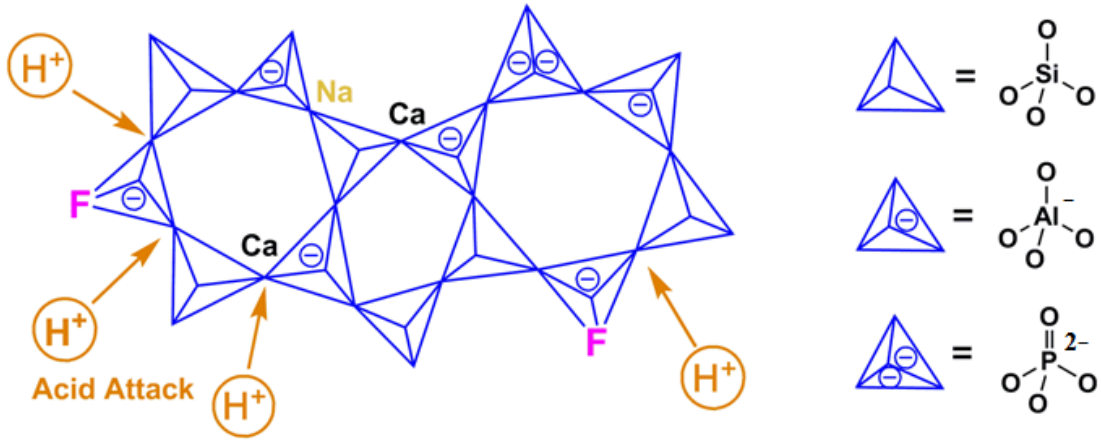

Figure 1.16 Qualitative representation of the microstructure of the glass component. Al has partially replaced silicon forming Al-O-Si bonds with Ca and Na charge balancing the network. P may also replace Al forming Al-O-P bonds. F may also break up the glass network by replacing bridging-oxygen and forming non-bridging fluorines.

1.5.1.5 Effect of sodium

Increase of sodium content increases setting rate but reduces the hydrolytic stability of the set cements. The sodium content should be minimal in order to produce cements with adequate hydrolytic stability [96].

1.5.1.6 Effect of fluorine

Glasses used in glass iononer cements are high in fluorine [108,119]. The fluorine's two major roles are:

1. *For appearance*: it lowers the glass' refractive index and enables the match to the polyacylate salts so translucent cements can be produced;
2. *For caries inhibitory*: it forms fluorine complexes in the cement matrix that lead to fluoride release.

It also breaks up the glass network by replacing bridging-oxygen and forming non-bridging fluorines [118] and facilitates acid attack and fast cement formation [108]. The strengths of the set cements first increase with an increase of fluorine content initially, and then reach a maximum before decrease with further increase of fluorine. Experimental cements with lower fluorine had increased fracture toughness [104]. For applications where appearance is not important, lower fluorine content may be preferable [119].

1.5.1.7 Effect of cation substitution

A study on the influence of certain cation substitutions on an equimolecular basis on the properties of the cements prepared from the glasses revealed that the replacement of CaF_2 by MgF_2 made the cement paste difficult to mix; replacement of CaF_2 by LaF_3 produced a rubbery cement mix but it had improved compressive strength; partial replacement of Al_2O_3 by TiO_2 slowed down the setting rate; replacement of NaF by LiF gave a glass that yielded a slow-setting cement with very poor resistance to aqueous attack [96]. None of the above substituting cations have produced as satisfying cement as the present composition.

1.5.2 The liquid component

GICs employ aqueous poly(acrylic acid) (PAA) solution or its copolymers (polyalkenoic acids) as the liquid component.

1.5.2.1 Synthesis

The acid solution is prepared directly by free radical polymerization of alkanoic acids (carboxylic acids) using ammonium persulphate as the initiator and propan-2-ol as a chain transfer agent. The concentration of acrylic acid was kept below 25%. The final concentration of the acids was obtained by vacuum distillation. The acid is then diluted with water to desired concentrations [120].

1.5.2.2 Composition

There are five generations of liquids for conventional GICs (**Table 5**).

Table 5. Liquid composition of the five generations of CGICs [121].

Generation	Acid (-m%)	Molecular weight (a.u)	Additive (-m%)
ASPA I	50% PAA	23,000	-
ASPA II	47.5% PAA	23,000	5% tartaric acid
ASPA III	45.25% PAA	23,000	4.75% tartaric acid 5% methanol
ASPA IV	47.5% 2:1 acrylic acid - itaconic acid	10,000	5% tartaric acid
ASPA V	47.5% 2:1 acrylic acid - itaconic acid	10,000	10% tartaric acid

A variety of other unsaturated carboxylic acids and monomers have been proposed to form copolymers with acrylic acid among which copolymers of acrylic acid - maleic acid and acrylic acid - 3-butene-1,2,3-tricarboxylic acid (**Figure 1.17**) were put into practical use.

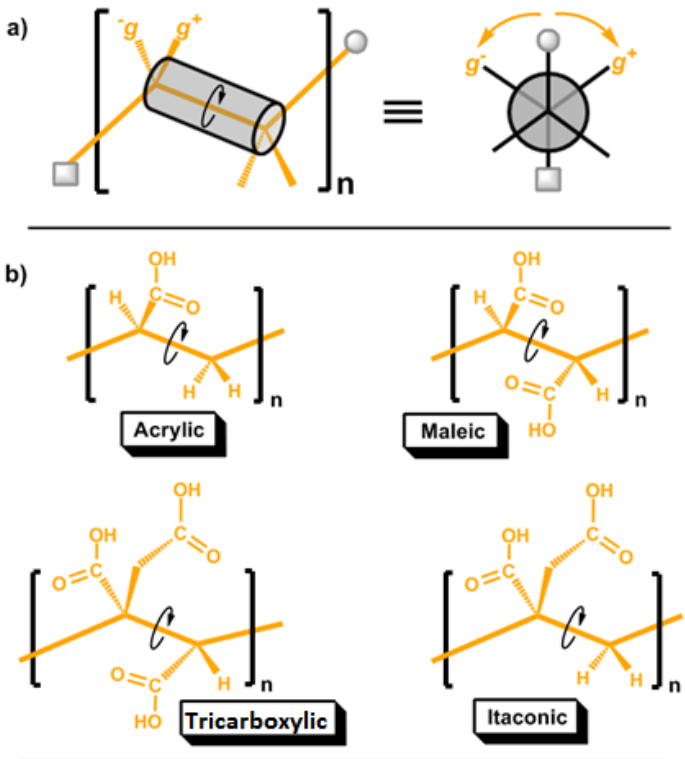

Figure 1.17 Stereochemistry of polyacrylic acid copolymer components. (a) Basic stereochemistry model: Sawhorse and Newman projections; (b) acrylic, maleic, tricarboxylic and itaconic acids.

1.5.2.3 Influence of polyacrylic acid molecular weight

The strength of the cement is dependent on the stress transfer between the structural elements (**Figure 1.18 a**). Increase of the polymer molecular weight will increase the amount of covalent bonds and lead to better stress distribution through the structure (**Figure 1.18 b**).

Polyacrylic acids of increased molecular weight produce cements of increased compressive, tensile strengths [122], flexural strength [123-125], fracture toughness, toughness [125], wear resistance, acid erosion resistance [124] and un-notched fracture strength [104] but with decreased setting and working times [122]. Higher molecular weight polymers have longer polymer chains which results in higher matrix strength as well as stronger bonding between the matrix and fillers.

DOI:10.14753/SE.2014.1974

1.5.2.4 Influence of polyacrylic acid concentration

Increase of the polymer concentration will increase the amount of covalent bonds which leads to better stress distribution through the structure (the polymer structure units are represented by orange spheres in **Figure 1.18 c**).

Change of the concentration affects the setting and working times. An increase in acid concentration causes increase in compressive and tensile strengths [111]. It is desirable to use high acid concentration provided that it gives adequate setting and working times.

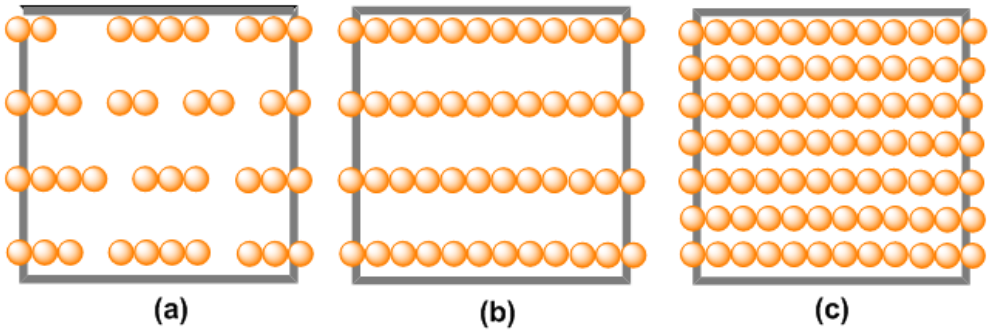

Figure 1.18 The strength of the cement is dependent on the stress transfer between the structural elements, for example, (a) polymer (represented by orange spheres). The strength can be improved by (b) increasing polymer molecular weight and (c) concentration. Reproduced from [101].

1.6 GIC characterisation techniques

Since their introduction in the early 1970s, intensive research has been carried out to characterise the properties and setting mechanism of existing and experimental GICs. Various techniques have been used, the principal ones of which are reviewed in this section of the dissertation.

1.6.1 Structural characterisation techniques

The structure of GICs and the glass component have been extensively studied with all kinds of microscopes, including light microscope, confocal fluorescent microscope, scanning electron microscope (SEM), transmission electron microscope (TEM), Ion microprobe, amongst others. With the aid of X-ray diffraction techniques (XRD), and

differential scanning calorimetry (DSC), the crystal structure, the phase properties and thermal history of the glass have been revealed [126].

1.6.1.1Transmission Electron Microscopy (TEM)

In TEM, a thin specimen is irradiated with an electron beam emitted from the electron gun. A three- or four-stage condenser-lens system permits variation of illumination aperture and illuminated specimen area [127]. The transmitted electron intensity distribution is then imaged with the lenses onto a fluorescent screen. Because of the small wavelength of electrons, TEM allows examination of objects with high resolution on the order of ~0.1 - 0.3 nm; as small as a single column of atoms. This has propelled TEM to becoming a principal method for imaging and analyses in the physical, materials and biological sciences [128].

1.6.1.2 Differential Scanning Calorimetry (DSC)

DSC is a thermal analytical technique which measures the change of the difference in the heat flow rate to the sample and a reference material subjected to controlled temperature modulation [129]. The temperature program keeps the sample and reference at the same temperature throughout the experiment, which increases linearly as a function of time. Schematic illustration of a heat flux DSC is shown in **Figure 1.19**.

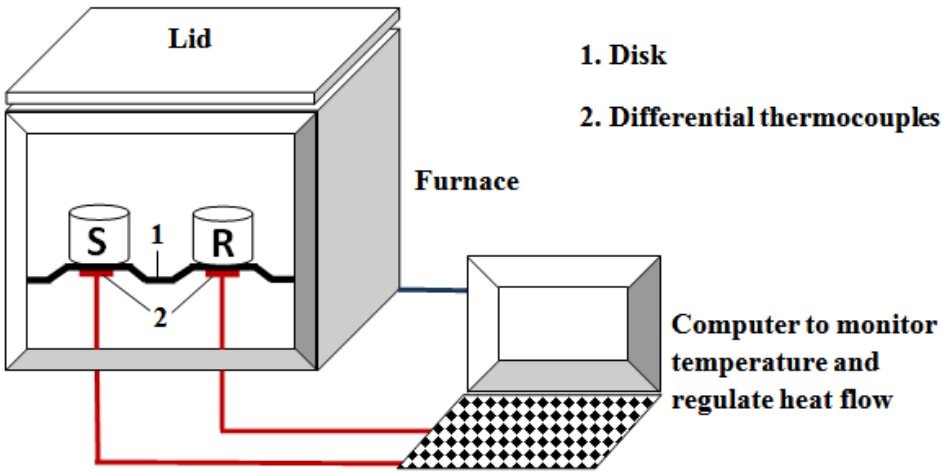

Figure 1.19 Schematic illustration of a heat-flux DSC with disk-type measuring system: 1. disk; 2. differential thermocouples; S. sample crucible and R. reference crucible.

DSC can quickly measure reaction heats, heats of transition and their change at characteristic temperatures on small sample masses (milligram). It is increasingly used

in quality assurance and the identification of substances, their stability, safety, associated kinetics, etc. [129]

1.6.2 Setting mechanism characterisation techniques

GIC setting mechanism has been studied with wet chemical extraction method [4], electrical method [98] and spectroscopic methods, like Infrared spectroscopy (IR), Fourier Transform Infrared spectroscopy (FTIR) [97], Raman spectroscopy [130], Nuclear magnetic resonance spectroscopic (NMR), among others.

1.6.2.1 NMR

NMR has been extensively used in tracking atomic structure in glassy and amorphous materials. NMR has proved to be a powerful tool in elucidating the early stages in the cement-forming reactions because it is able to discriminate between the various complexes formed and the atoms in different environment [131]. Studies of GIC setting reactions, structure and changes during setting have likewise benefitted from NMR, specifically ^{1}H-, ^{13}C-, ^{19}F-, ^{27}Al-, ^{29}Si- and ^{31}P-(MAS)NMR have all been employed [132-142].

Results are reported as showing Al changing coordination from Al(IV) to Al(V) through to Al(VI) (**Figure 1.20**), however several shoulders and so called 'mystery peaks' adorn the spectra [110,143], with conclusions that the role of each atom requires tracking throughout the lifetime of the setting reaction [110].

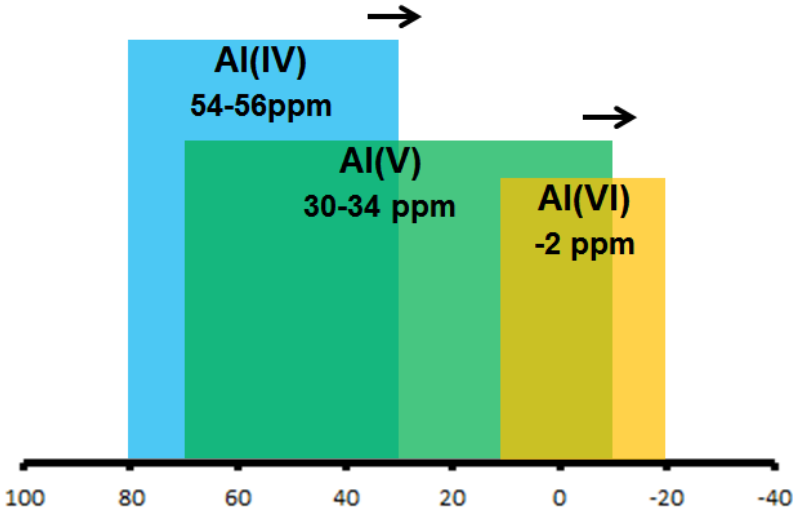

Figure 1.20 Simplified representations of Hill *et al*'s deconvoluted experimental ^{27}Al MAS-NMR spectra of GICs indicating Al changing coordination from Al(IV) to Al(V) through to Al(VI) over cementation.

DOI:10.14753/SE.2014.1974

In these GIC studies, deconvolution of the ^{27}Al spectra (**Figure 1.21**) was performed based on the knowledge that the integration of each peak is directly proportional to the amount of that Al species in the cement [110].

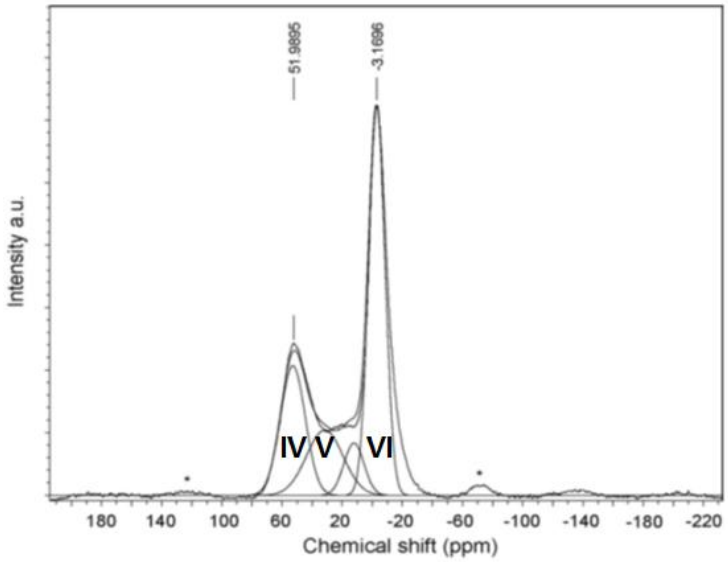

Figure 1.21 Experimental and simulated ^{27}Al spectra of LG125 cement at one year. Peak at ca. ~50 ppm is assigned as Al(IV) and ~-2 ppm is Al(VI). The shoulder between these peaks at ~30 ppm is assigned as Al(V) and/or line broadening quadrupolar effect of Al(IV) [136].

These were assigned Al(IV) (54-56 ppm), Al(V) (30-34 ppm) and Al(VI) (-2 ppm). It was discovered that a portion of Al(IV) in the glass converted to Al(VI) [132-136] whose intensity increased as the cement set (**Figure 1.22**). Al(V) was still present in cements aged up to one year [110] but disappeared after some time in other studies [132,133].

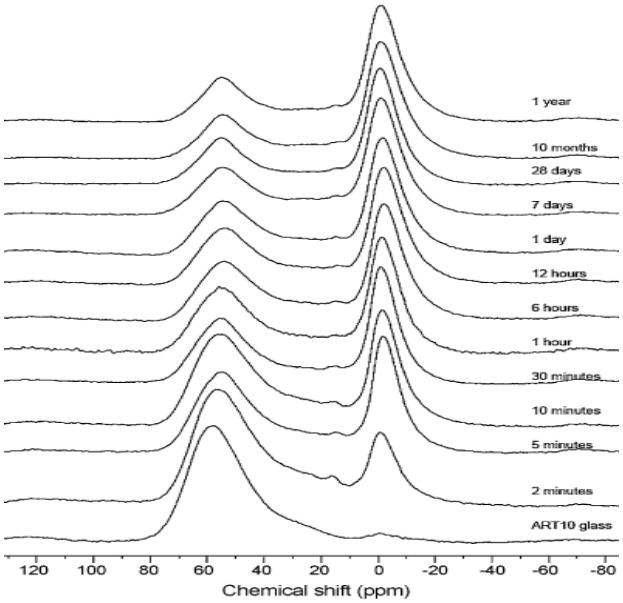

Figure 1.22 The ^{27}Al MAS-NMR spectra of GIC based on ART10 [110].

1.6.3 Mechanical characterisation techniques

One of the major requirements of a product in service is that the mechanical properties are suitable to the task. Mechanical testing helps to resolve a material's response to the relevant physical changes and challenges it experiences towards predicting service performance. It is also the most direct way in which the success or failure of modifications to its formulation or other relevant changes to application may be evaluated.

The mechanical properties of GICs have been characterised using various conventional mechanical testing methods used in materials science as follows:

- Compression test
- Tensile strength test
- Diametral tensile strength test
- Flexural strength test
- Bi-axial flexure test

1.6.3.1 Fracture toughness test

The reliability of the above mentioned strength tests has been brought into doubt - compressive and diametral tensile strength tests allegedly measure shear strength, which is most probably the mechanism of failure [144]. Flexural strength testing is very sensitive to the surface conditions on the bottom tension face, effectively making such superficial flaws the controlling factor.

This is further evidenced by literature strength values widely varying for the same materials [145]; measured strength being highly-dependent on processing history, test methodology, testing environment, strain rate, failure mechanism, etc. Unless the critical flaw size and distribution are identical to those involved in clinical failure, laboratory failure strengths will not provide accurate information on the likely performance in clinical use [146]. Compressive strength has been demonstrated to be an invalid measure of "strength", due to the simple and logical reason that a material cannot fail in compression, offering no advantage in the context of the strength data it

generates [147,148]. A proposition has been made to eliminate it from the International Organisation for Standardisation (ISO 9917-1: 2003) [148].

Additionally, failure in strength testing is caused by material fracture. In other words, fracture initiates the termination of the test, followed by tabulation of strength values so-garnered. However, any isolated strength-testing without relation to fracture studies is invalid and out of context.

In contrast, fracture toughness considers the effect of such stress concentration, a phenomenon that has pronounced effect on the likelihood of failure of brittle materials [149].

Plain-strain fracture toughness K_{IC}, also called failure mode I (tensile failure) critical stress intensity factor, is an intrinsic property of a material and is a measure of the energy required for a crack to propagate from an existing defect. For any given flaw size, a material with a higher K_{IC} value will survive a higher stress before catastrophic failure. It has been proved suitable for explaining clinical observations or for predicting the performance of new materials [57]. A variety of test configurations have been devised for measuring it. These tests embody pre-existing cracks or defects within the materials and K_{IC} is defined and calculated from the specimen dimension, defect size and the fracture load [149]. The following tests have been used to measure fracture toughness of GICs:

- Single-edge-notch test (SEN)
- Chevron-notch short-rod test
- Double-torsion test
- Compact tension test

Table 6 presents fracture toughness study results of different types of GICs in the literature.

However, there are practical difficulties in determining fracture toughness for glass ionomers, and only few studies have been reported on this property [6].

DOI:10.14753/SE.2014.1974

Table 6. Fracture toughness study results of different types of GICs in the literature.

Cement	Age	Geometry	Test	Crosshead speed	Fracture toughness	Ref
Ketac-Fil	1 day	3×6×35, 2.5 mm notch	Single Edge Notch	0.127 mm/min	0.35	[150]
Ketac Silver	1h,5h,1d,7d, 1m,3m	3×6×34 mm	Single Edge Notch	0.1 mm/s	0.3-0.45	[95]
Chemfil II					0.38-0.5	
Chemfil II Express	1 week	3×6×34, 1.5 mm notch	Single Edge Notch	5 mm/min	0.48	[151]
Fuji II					0.27	
Ketac Silver					0.37	
Chelon Silver					0.33	
Miracle Mix					0.21	
KetacCem luting	1 week	4×8, 6 mm load line, 2 mm crack	Chevron notch short rod	4 µm/s	0.27	[147]
Fuji I luting					0.34	
KetacCem					0.37	
Fuji Cap I					0.37	
Vitremer luting					1.08	
Fuji II LC	1h, 1d, 1w, 1m, 6m	2.5×5×25, 2.5 mm notch	Single Edge Notch	0.5 mm/min	1.23-1.49	[152]
Vitremer					0.86-1.51	
Fuji II					0.35-0.56	
Fuji II	Non-aged, 9 m	2.5×5×25, 2 mm notch	Single Edge Notch	2 mm/min	0.3-0.7	[153]
Miracle Mix					0.4-0.6	
Fuji II LC					0.4-1.2	
Resiomer					0.6-1.2	
Fuji II	2 m	2×10×30, 0.2 mm groove	Double Torsion	0.05 mm/min	0.51	[57]
Ketac-Fil					0.55	
Ketac-Fil	24 h	3×6×35, 2.5 mm notch, 2D,3D FEA	Single Edge Notch	0.127 mm/min	0.3-0.4	[154]
Fuji I	7 d	4×8, 6 mm load line, 2 mm crack	Chevron notch short rod	4 µm/s	0.26-0.27	[155]
Fuji Plus					0.67-0.72	
Experimental GICs	24 h	3.5×25×65 mm	Double Torsion	0.1 mm/min	0.13-0.33	[156]
		3×24×25 mm	Compact Tension		0.13-0.25	
Experimental GICs	4.5-3812h	3.5×65×25 mm	Double Torsion	0.1mm/min	0.15-0.34	[94]
Fuji II	1 w	N/A	Single Edge Notch	0.1mm/s	0.26	[157]
ASPA					0.34	
Chemfil					0.45	
Coreshade	1 w	2×4×20, 2 mm notch	Single Edge Notch	0.51 mm/min	0.55	[158]
Ketac Molar	24 h	1.8×4.2×20, 2 mm notch	Single Edge Notch	1.25 mm/min	0.72	[149]
Vitreme					0.75	
Vitremer Luting	24 h, 7 d	N/A	Mini Compact Tension	0.5 mm/min	0.4-0.7	[159]
Advance					0.8-0.82	
Fuji Duel					0.7-0.75	
Ketac-Cem					0.2-0.25	
α-Silver	7 d	N/A	Mini Compact Tension	0.5 mm/min	0.45	[160]
α-Fil					0.5	
Ketac-Molar					0.45	
Vitremer					0.61	
Fuji II LC					0.52	
Photac-Fil					0.68	
Experimental GICs	24 h	3.5×65×25 mm	Double Torsion	0.1 mm/min	0.1-0.33	[124]
Experimental GICs	1d,7d,28d	3.5×65×25 mm	Double Torsion	0.1 mm/min	0.27-1.39	[104]

1.6.3.2 Hertzian indentation test

Although a significant amount of work has been completed on GICs using the aforementioned strength tests, they predominantly focus on simple strength values that do not correlate with clinical behavior.

Hertzian indentation testing has been well established as a clinically-relevant approach to failure testing of both monolithic and layered dental ceramics [161,162], due to its ability to reproduce bottom-initiated radial cracking that is consistent with the failure mode observed in failed dental restorations [163,164]. It also offers insights for assessing damage mode and fracture process under concentrated contact loading [161,162]. Darvell and coworkers have proved that Hertzian indentation testing can be extended to amalgam and GICs for investigation of clinically-relevant failure mode, while also accommodating varied coating thickness [165-167].

GIC discs 2 mm thick and 10 mm diameter have been tested by loading centrally using a 20 mm diameter hard steel ball while resting freely on a filled-nylon substrate (E=10 GPa) at 23 °C in air (**Figure 1.23**). The failure load at the first bottom-initiated radial cracking is detected with the aid of an acoustic emission detection system. Failure loads for CGICs have a mean value around 250 N and the failure mode is complete radial cracking [166].

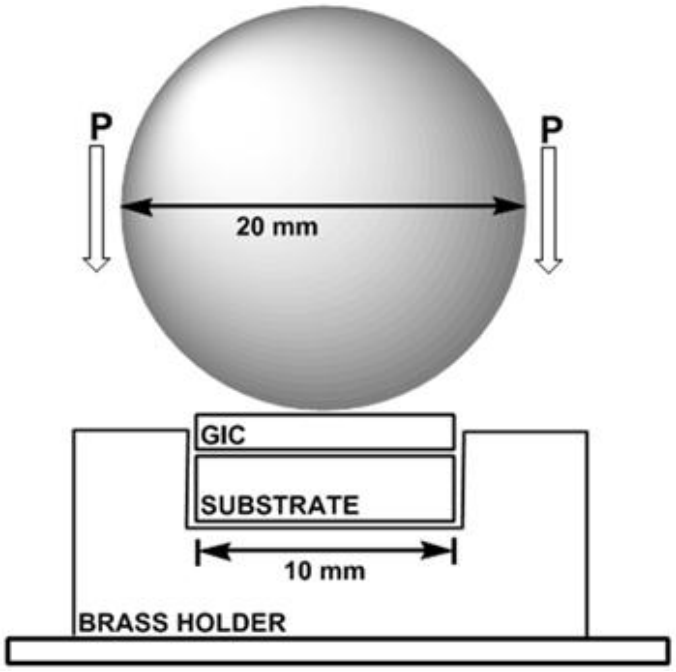

Figure 1.23 Hertzian indentation test geometry. The upper grey sphere represents the ball indenter of 20 mm diameter under downward load. The lower part represents the sample holder holding in place the10 mm diameter GIC disc on top of substrate [165].

1.6.3.3 Fractography

An effective means of evaluating the results of the aforementioned mechanical tests, is by fractographic analyses, which correlates strength values with material behaviour [168]. It uses 2-D imaging equipment (camera, optical microscope, SEM, etc.) to identify and characterise fracture features [169]. It is essential for critical flaw determination and strength prediction [168]. Tracking the fracture propagation directions also helps gain insight into the microstructure of a material. Fractographic analyses have been successfully applied to fracture surfaces of dental ceramics [170], composite resins [168] and GICs [112,147,148].

However, the imaging techniques adopted in these examinations limit the study to near-fracture surface regions, resulting in only partial detection of the 3-D crack network; no information is revealed on internal defects and crack-microstructure interaction in the sample-bulk. Additionally, the high vacuum used in scanning electron microscopy causes dehydration, and this creates artificial features in the sample. Therefore, a non-destructive 3-D imaging method revealing structural features in the bulk of the material would be of considerable value.

1.6.3.4 X-ray micro computed tomography (μCT)

A non-destructive 3-D imaging method that can complement fractography has been made possible via recent developments in high-resolution X-ray micro computed tomography (μCT).

μCT uses X-ray to scan the cross-sections of a 3-D object taking advantage of X-ray absorption contrast within the object and the scan slices can recreate a virtual model of the object [171]. The pixel size of the cross-section is in the micrometer range. X-ray nanotomography uses pixel in the nanometer range. They provide non-destructive 3-D micrography of the internal structure of the object scanned. For this function, micro (nano) tomography may be used to investigate an object's internal structure before and after external loads are applied in order to study the impact the loads have on the object and the object's internal response to the loads.

Successful non-destructive 3-D fracture characterisation and microstructure analysis on engineering materials [172] and bone cements [173] have taken advantage of this technique. X-ray microtomography has found three applications in dental field, namely

mapping of root cannel anatomy [174-179], material porosity measurement [56] and data feeding for finite element analysis [180-182].

1.7 Modifications to GICs

Although GICs possess unique properties that make them useful in restorative and adhesive dentistry, their brittleness, low fracture toughness and early sensitivity to moisture limits them to non-load bearing application.

Ever since their introduction in 1970s, much effort has been devoted for GIC modification aiming at improving their performance. The major modifications are reviewed in this section.

1.7.1 Modifications to the glass component

Filler reinforced glasses were experimented on (**Table 7**) but the filler matrix bonding was no better than that of the CGICs, which defeats the original purpose of toughening the material with filler reinforcement (**Figure 1.24**). Not until this problem is solved, filled glass will not produce cement with significant improvement [118].

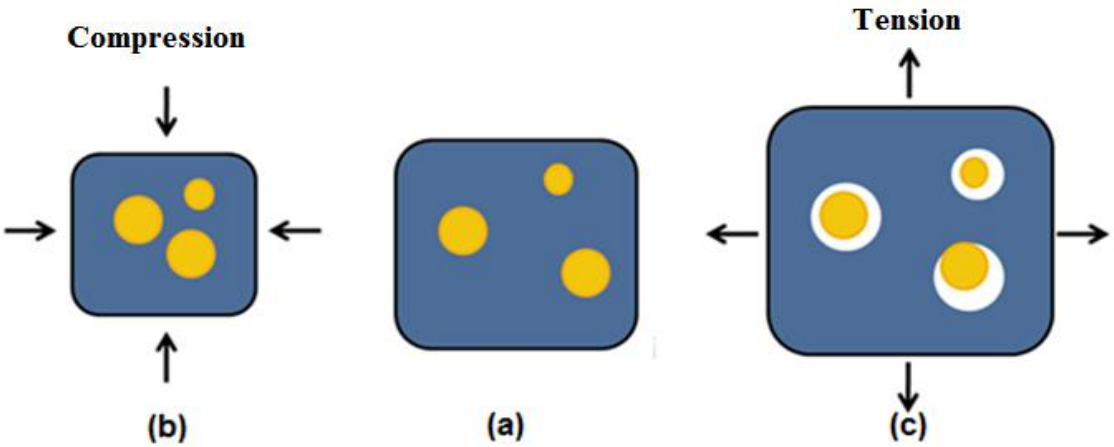

Figure 1.24 Illustration of reinforcement effect of fillers represented by three yellow circles in (a) under stress: when the filler-matrix bonding is weak the reinforcement effect works under compression (b), but does not work under tension (c).

DOI:10.14753/SE.2014.1974

Table 7. Modifications to CGIC glass powder.

Modification	Method	Setting time	Abrasion Resistance	Compressive Strength	Flexural Strength	Tensile Strength	Fracture Toughness	Hydrolytic Stability	Reference
Amalgam reinforcement	amalgam fused and sintered	-	↑	↑	↔*	-	0.21	good	[183,184]
Silver reinforcement	silver powder sintered	faster setting	↑	↑	↓	-	-	good	[185]
Stainless steel reinforcement	mix 9 µm SS particles with glass	faster setting	-	↑	-	↑	-	good	[186]
Aluminoborate glass	boric, zinc, aluminium oxides	faster setting	-	-	-	↔	-	poor	[187-189]
Zinc silicate glass	Al_2O_3-ZnO-SiO_2	faster setting	-	↑	-	-	-	good	[190]
SrO glass	5% SrO addition	slower setting	-	↑	-	-	-	good	[191]
Crystallite strengthened	dispersed phase droplets inclusion	-	-	-	↑	-	-	good	[123]
Glass fibre reinforcement	reactive glass fibre addition	-	-	↑	↑	-	0.22	good	[192,193]
Bioactive glass particles	bioactive glass addition	-	-	↓	-	-	-	good	[194,195]
HA incorporated	HA or HA/ZrO_2 addition	-	-	↑	↑	↑	0.58	good	[196-200]
Zirconia GIC	Yttria stabilized ZrO_2	-	-	↑	-	↑	-	good	[201]

* ↔ - No significant increase.

DOI:10.14753/SE.2014.1974

1.7.2 Modifications to the liquid component

1.7.2.1 Other copolymers

Synthesis of amino acid-, methacryloyl glutamic acid- and N-vinylpyrrolidone-containing polyelectrolytes (**Figure 1.25**) [20,202] were proposed to improve the mechanical properties (**Table 8**) by enhancing ionic cross-linking and reinforcing the interfacial bonding between salt matrix and the glass particles in the set cement. The idea is that since cross-linking is not complete, i.e. only a fraction of aluminium cations and carboxylic groups are chelated, which may be due to the short side chain length from the polymer backbone, not providing enough space for chelation. Overcoming this steric hindrance is done by tethering different types of acid groups to the polymer backbone. This way various side chain lengths are achieved making more carboxylic groups more available for chelation and high stability. This spacing out strategy has proved efficient in enhancing the level of salt-bridge formation and improving cement properties [203].

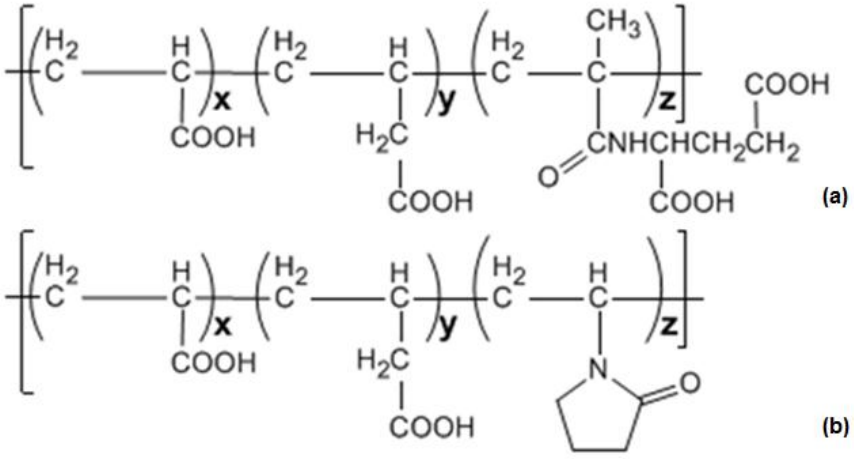

Figure 1.25 Copolymers of (a) AAx (acrylic acid)-IAy (itaconic acid)-MGAz (methacryloyl glutamic acid) and (b) AAx-IAy-NVPz (N-vinylpyrrolidone acid).

DOI:10.14753/SE.2014.1974

Table 8. Mechanical properties of GICs based on commercial and experimental acid polymers [204-207].

	Commercial	$AA_xIA_yMGA_z$*		$AA_xIA_yNVP_z$*
Acid type	Fuji II	8:1:1 copolymer	7:3:3 copolymer	7:3:1 copolymer
Compressive strength / MPa	204.8	269.9	223.6	276.0
Knoop surface hardness	36.7	36.5	-	-
Flexural strength / MPa	14.9	-	34.6	34
Fracture toughness/$MNm^{-1.5}$	0.52	-	0.64	0.607

*AA: Acrylic Acid; IA: Itaconic Acid
MGA: Methacryloyl Glutamic Acid
NVP: *N*-VinylPyrrolidone

1.7.2.2 Resin modified GICs (RMGICs)

A very important modification to the liquid component is the resin-modified form. Resin-modified refers to the addition of polymerisable resin groups (usually 2-hydroxyethyl methacrylate, or HEMA) by grafting them to the molecules of the acid solution. So this class of materials usually contains polymerisable monomers with their initiation system (chemical or light) and the GIC components: glass component and aqueous acid solution. The setting reactions are polymerisation as well as acid-base reaction (**Figure 1.26**) [208]. Only about 5% of the mixed cement will be resin, and when polymerised it will impart strength as well as protection to the ongoing acid-base reaction from dehydration and water sorption. These products are considered dual-setting if only one polymerisation mechanism is used and tri-setting (dual-cure) if two polymerisation mechanisms are used. The simplest form of these materials is GIC mixed with a minor amount of HEMA or Bis-GMA in the liquid. More complex materials contain modified polyalkenoic acid with polymerisable side chains [208].

DOI:10.14753/SE.2014.1974

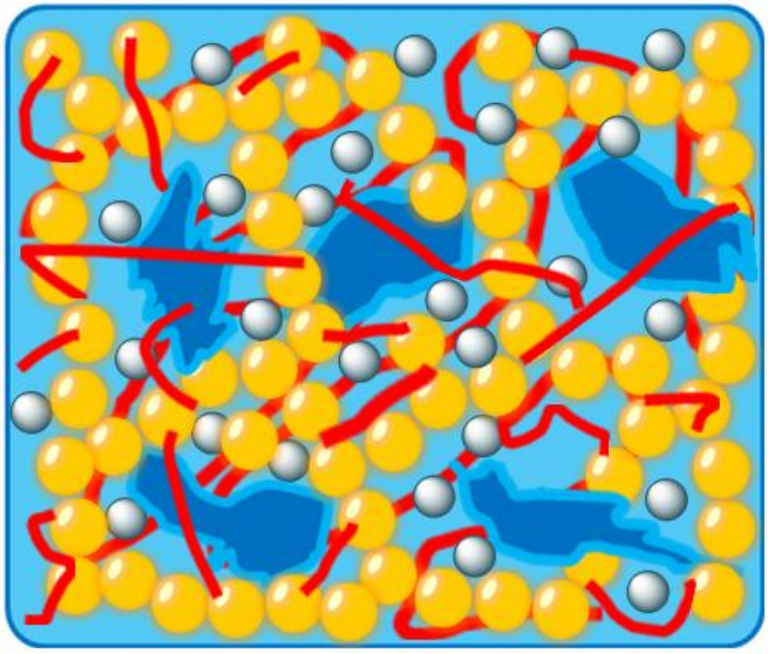

Figure 1.26 Qualitative representation of resin-modified GIC structure. The cement is composed of precipitated polyacrylate salt matrix and glass particle fillers (irregular blue shapes) sheathed with silica gel (light blue). The polyacrylate salt matrix consists of polymer chains (bright yellow bubble chains) cross-linked by Al^{3+} cations (grey spheres) as well as the polymerised resin component (red lines). The filler-matrix interface is composed of polyacrylate salt bridges formed by the surface Al^{3+} cations cross-linking the polymer chains. The other ions are the same as CGICs and are not shown here.

RMGICs possess the advantages of both composite resin and that of GICs. They generally adhere to dentin and enamel [209] and release fluoride [210]. They also release other species same as CGICs [211]. They are superior to CGICs on the following aspects:

- *Early water stability*: According to solubility test result, the water solubility of RMGIC was reduced by 34% compared with CGICs during the first hour of storage [212].
- *Command set*: Command set of RMGICs gives the practitioners enough working time and they almost set instantaneously with the light activation.
- *Immediate strength*: RMGICs have 27% higher compressive strength and 21% higher yield strength at one hour [212] so they can bear masticating stress sooner after they set.
- *Less brittle*: RMGICs are less brittle with 33% increased fracture toughness [212].
- *Elevated surface crazing problem when desiccated*: RMGICs are less susceptible to dehydration and surface cracking [212].

They also have disadvantages, i.e. volumetric change caused by curing shrinkage [213], slight swelling caused by water absorption [213,214] and toxicity of monomers [215]. The tendency of phase separation during setting [216] is another disadvantage.

Despite all these, RMGICs have been found satisfactory in primary dentition and are now being used to restore permanent teeth. This class of materials has great potential to remain the material of choice for restorative dentistry.

1.7.2.3 Acids other than polyacrylic acid

The use of Poly (Vinyl Phosphonic Acid), PVPA, $-[-CH_2-CHPO(OH)_2-]_n-$, as the liquid component has produced cements of improved handling characteristics, adhesion, translucence and greater hydrolytic stability over the polyacrylic acid - based cements [217-220]. Modification of PVPA by incorporating cross-linking agents, e.g. formaldehyde and buta-1,3-diene diepoxide, during the polymerisation has led to cements of improved compressive strength (138.1 MPa). This new line of materials has the potential of developing into suitable materials for clinical applications [220].

Unfortunately most approaches to optimising material performance rely on combinatorial (trial-and-error) or serendipitous means. Lacking fundamental understanding of the structure and dynamics of set (hardened) GICs, or of the setting process itself, leaves the rational optimisation and design of GICs in its infancy.

Timing is optimal for introducing novel approach towards rational characterisation and design for optimised material performance.

1.8 Novel techniques

1.8.1 Neutron spectroscopy

The timeliness of this work is highlighted by the results of an ISI Web of Science search of the terms ‘bioglass AND neutron’, generating only 3 hits, whilst ‘glass AND ionomer AND diffraction’ produced only 45 hits (1st work in 1992). Only 1 work involving neutron scattering on dental composites was identified, which used neutron diffraction

technique to identify phases formed during heat treatment of a commercial dental glass-ceramic [221], whilst no computational modelling has been documented to-date.

1.8.1.1 Fundamental background

The neutron is a subatomic hadron particle which has the symbol n or n^0, zero net electric charge and a mass slightly larger than a proton and 1,839 times that of an electron. Neutrons have a mean lifetime of ~1000 s. The nucleus of an atom consists of protons and neutrons (**Figure 1.27**). The number of neutrons determines the isotope of an element - while all isotopes of a given element have the same number of constituent protons, each isotope differs in its number of neutrons. For example, C-12 has 6 protons and 6 neutrons while C-14 has 6 protons and 8 neutrons.

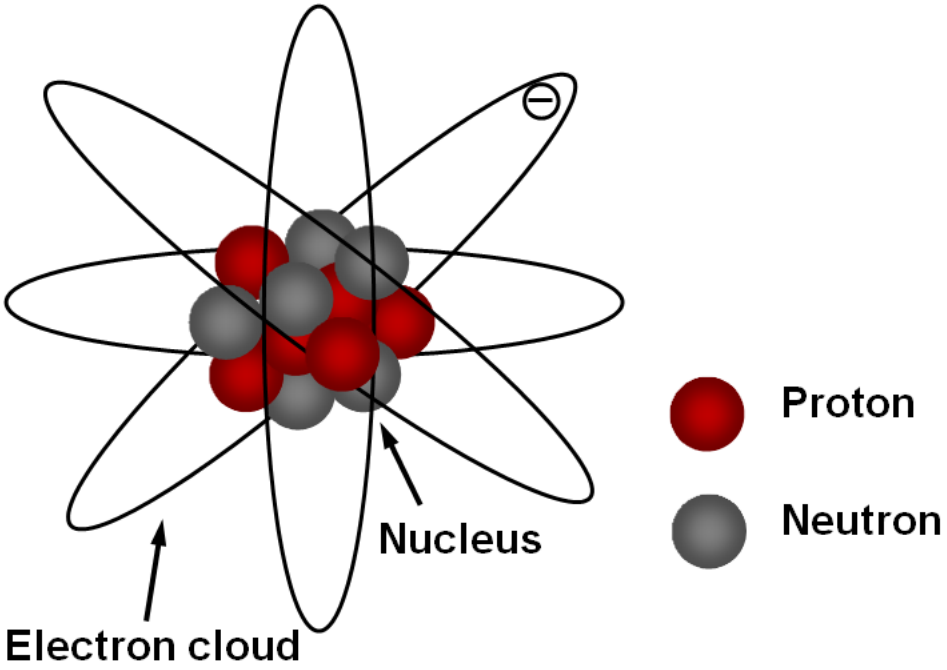

Figure 1.27 A nucleus is composed of protons (red) and neutrons (grey) with the electron cloud orbiting around it, with each electron having a particular energy level and angular momentum.

Use of neutrons in spectroscopy has significant advantages over other forms of radiation in the study of microscopic structure and dynamics of materials. Neutrons scatter from materials by interacting with the nucleus of an atom rather than the electron cloud. This means that the scattering power (cross-section) [222] (**Figure 1.28**) of an atom is strongly related to its atomic number, unlike X-rays [223] and electrons whose scattering power is related to the number of electrons associated with the atom.

Scattering cross-section σ_{scat} is a hypothetical area which describes the likelihood of light/particle beam being scattered by a particle. It depends on the wavelength of the light/particle beam as well as the shape, size and permittivity of the particle. The total amount of scattering in a sparse medium is determined by the product of the scattering cross-section and the number of particles.

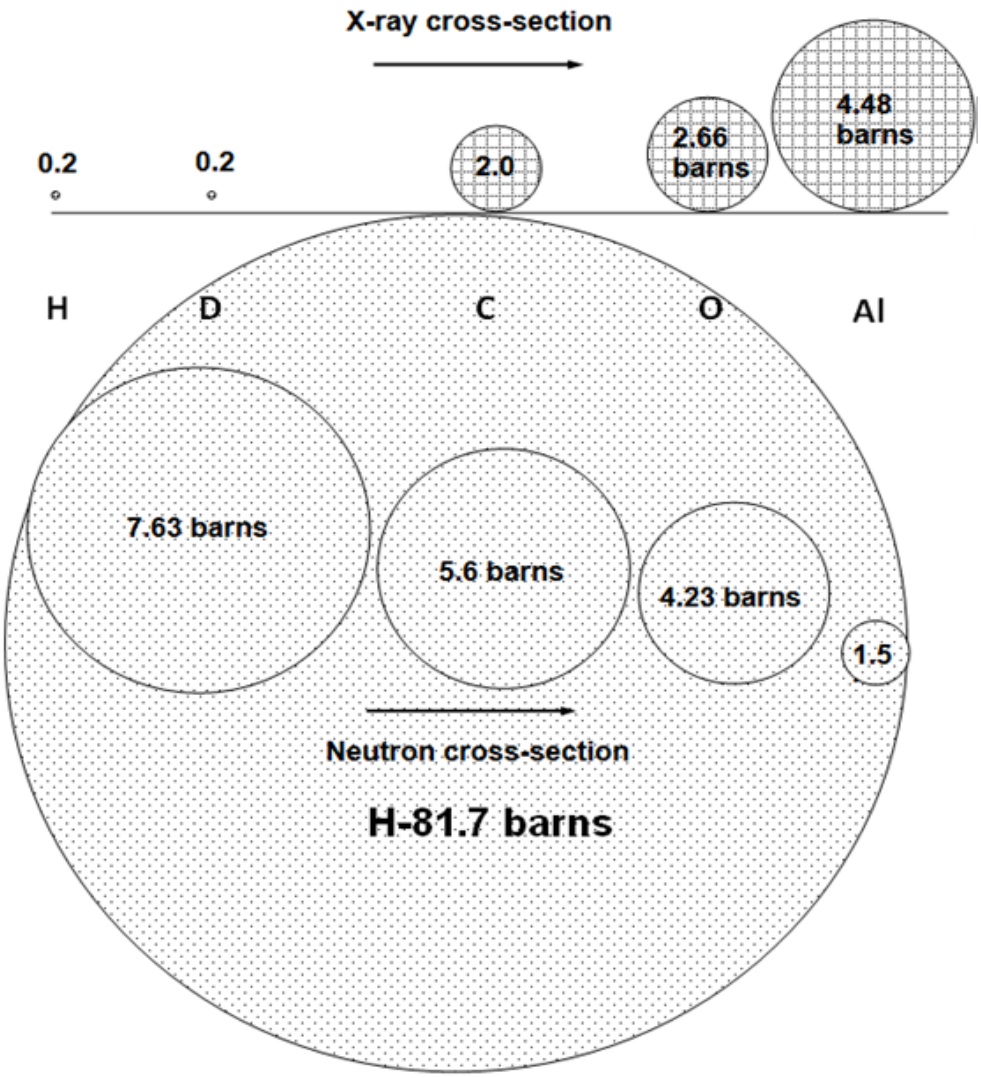

Figure 1.28 X-ray and neutron scattering cross-sections for H, D, C, O and Al in barns (10^{-28} m^2) [222,223]. The diameters of the spheres are proportional to the cross-section values.

The characteristic neutron interaction has three advantages:

- It is easier to sense light atoms, such as hydrogen, in the presence of heavier ones;
- Neighbouring elements in the periodic table generally have significantly different scattering cross-sections and can be distinguished;

- Neutrons can differentiate between isotopes. Isotopic substitution can be used to label different parts of the material or molecule in a sample.

The interaction of a neutron with the nucleus of an atom is element specific and mediated by the strong nuclear force, while also being insensitive to the electronic environment, making them a highly penetrating non-destructive probe. This allows the investigation of the interior of materials and bulk processes under realistic conditions [224]. Neutron energies are similar to the energies of atomic and electronic processes, (i.e. in the μeV to eV range), allowing energy scales associated with μeV quantum tunneling, through the meV of molecular translations, rotations, lattive modes (phonons) and vibrations, to eV atomic recoils and electronic structure transitions [224].

The two dominate means to produce neutrons for scientific research are neutron-induced nuclear fission (**Figure 1.29)** as used at the Institut Laue Langevin (ILL, Grenoble, France) and through neutron spallation processes (**Figure 1.30)** as employed at the ISIS pulsed neutron and muon source at the Rutherford Appleton Laboratory (RAL, Harwell, Oxfordshire, UK).

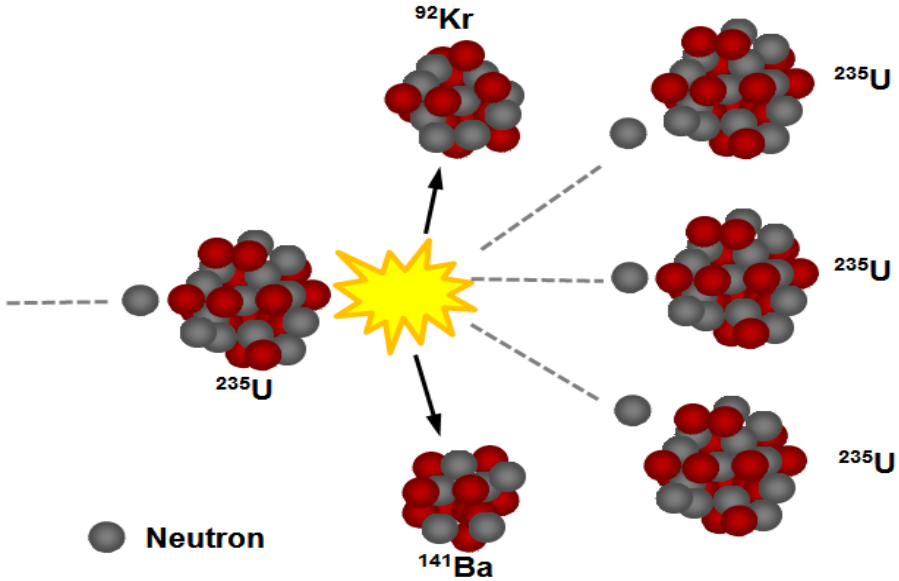

Figure 1.29 Illustration of nuclear fission reaction wherein the ^{235}U nucleus is promoted to an excited state by the collision of an incident neutron (grey). This splits the ^{235}U nucleus into fast-moving ^{92}Kr and ^{141}Ba nuclei with subsequent release of three free fast neutrons; the latter going on to excite ^{235}U nuclei, inducing a chain reaction.

At a spallation source, production of neutrons is achieved by accelerating bunches of protons in a linear accelerator and subsequently in a synchrotron to sufficiently high

energies (~0.90-0.95c; where c=speed of light) such that when they collide with a heavy (metal) target nucleus (tantalum-Ta, tungsten-W, or even mercury-Hg) they produce highly excited nuclear states in the target nuclei. These nuclei subsequently relax by ejecting neutrons, gamma (γ) rays and neutrinos (**Figure 1.30**). The maximum energy of neutrons produced corresponds to the energy of the impinging proton beam resulting in neutrons of much higher energies than those produced in nuclear reactors. A reflector made of beryllium surrounds the target to reflect the ejected neutrons back into the target area in order to increase the neutron flux [225]. At ISIS the average flux is ~2×10^{13} n/cm^2/s and the peak flux can reach ~8×10^{15} n/cm^2/s.

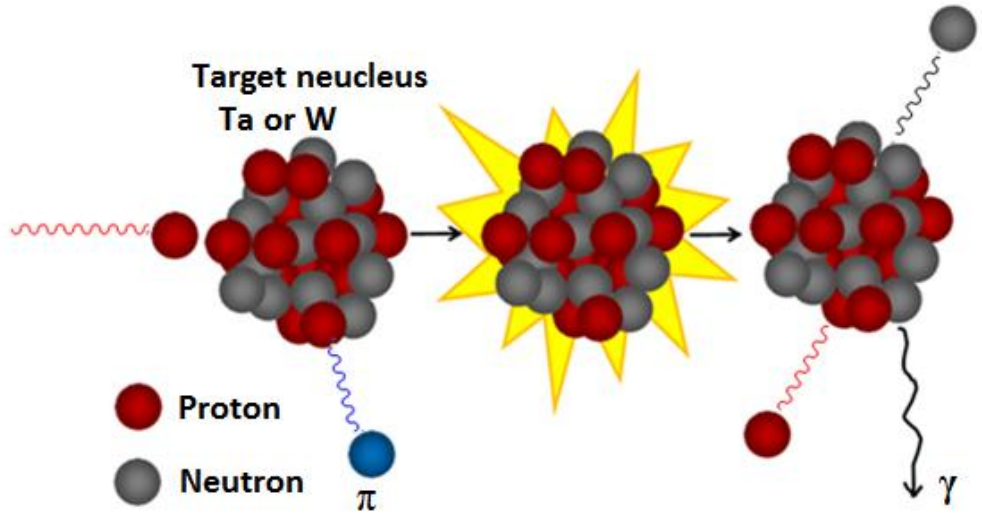

Figure 1.30 Illustration of neutron spallation reaction. High-energy protons (red) collide with a heavy metal target and produces an exited nuclear state which relaxes through emission of high-speed neutrons (grey) and other particles, including protons (red), pions (π, blue) and γ rays (black).

A spallation neutron source is safer to manage (relative to nuclear reactors) and provides broader diversity of scientific tools. The proton beam can be emitted in short pulses (~400 ns wide), allowing for temporal control of neutrons departure from the target. As the mass of all neutrons is fixed, their energies can be derived from their time of flight (TOF) from the moderator (medium that reduces the speed of fast neutrons) to the detectors. TOF *t* (**Figure 1.31**) can be expressed as [226]:

$$t = \frac{L_0}{v_0} + \frac{L_1}{v_1} \qquad \text{(Eq. 1.8)}$$

DOI:10.14753/SE.2014.1974

Where L_0 is the incident flight path length from moderator to sample; v_0 is incident neutron velocity; L_1 is the final flight path from sample to detector; v_1 is the scattered neutron velocity.

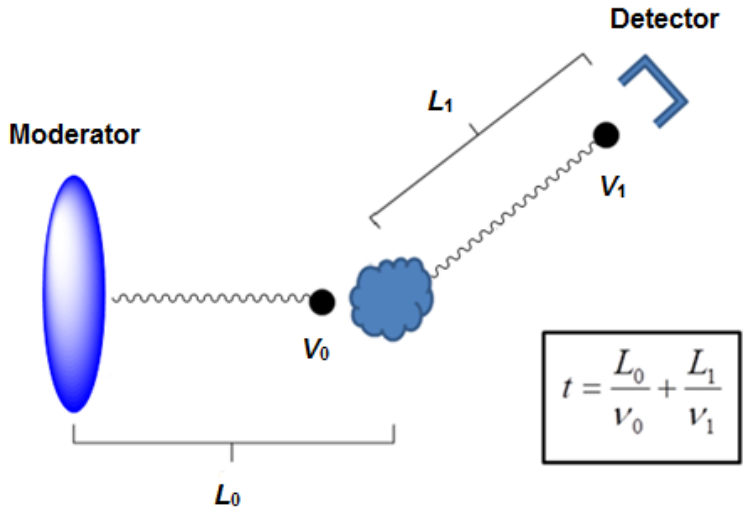

Figure 1.31 Illustration of neutron TOF *t*, which is the time it takes a neutron to travel over the initial flight path (L_0) from the moderator to the sample at the initial velocity v_0 and over the final flight path (L_1) from the sample to the detector at the final velocity v_1.

1.8.1.2 Neutron Compton Scattering (NCS)

Also called Deep Inelastic Neutron Scattering (DINS), this technique is analogous to the measurement of the electronic momentum distribution through Compton scattering of high-energy photons from electrons, or the nucleon momentum distribution via quasi-elastic electron scattering from nuclei. NCS is the only effective technique at present for deriving the single-particle (atomic and molecular) momentum distributions, $n(p)$, in condensed matter systems [227]. In simple terms, NCS may be regarded as atomic mass spectroscopy in which each atomic mass contributes to the overall time-of-flight spectrum in the form of a Doppler-broadened recoil peak. The width of such a recoil peak is related to the kinetic-energy distribution in momentum space of the target nucleus before collision [228].

The basis of the NCS technique is impulse approximation (IA), which treats the atom-neutron collision event as the neutron scattering from a single atom with conservation of the total kinetic energy and momentum of the neutron plus the atom, at sufficiently high momentum transfer [226]. A basic assumption of IA is that for neutron wavelengths much less than the inter-atomic spacing, atoms scatter incoherently and the impacted atoms recoil freely from the collision.

DOI:10.14753/SE.2014.1974

The VESUVIO inverse geometry time of flight spectrometer (**Figure 1.32**) at the ISIS spallation neutron source of the Rutherford Appleton Laboratory (UK) has high instrumental resolution and a wide accessible kinematical space: 1 eV<$\hbar\omega$< 20 eV (energy transfer) and 20 Å^{-1}<q<250 Å^{-1} (momentum transfer). At these wavevectors, scattering is well described within the framework of the IA, which is exact in the limit of infinite momentum transfer [227,229].

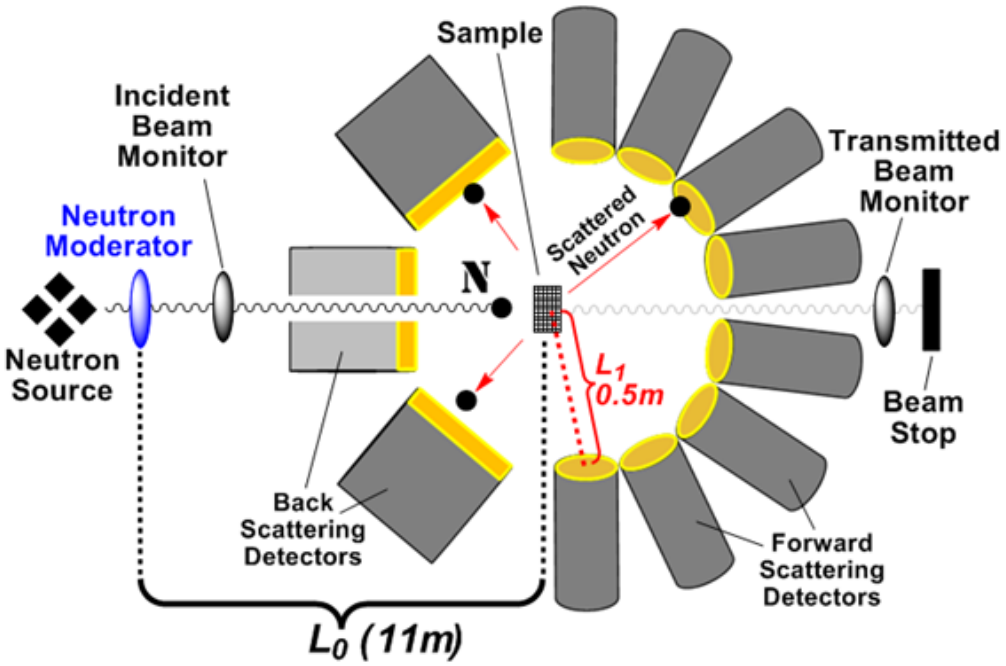

Figure 1.32 Schematic of VESUVIO instrument. The three grey rectangles are back scattering detector banks covering angular range 133-165 degrees and the 8 grey cylinders are forward scattering detector banks covering angular range 30-70 degrees. The sample is located in the center at an equal distance of L_1 (final flight path of 0.5 m) from all the detector banks. Incident neutrons N from the neutron source travel along incident flight path L_0 (11 m) from the neutron moderator to the sample. The neutrons scattered by the sample atoms are detected by the detectors while the transmitted neutrons go through the transmitted beam monitor and stop at the beam stop.

Under these conditions, applying the momentum and energy conservation laws, the energy and momentum transfers are related by

$$\hbar\omega = \frac{(p_n - p_n')^2}{2M} + \frac{(p_n - p_n')\cdot p}{M} \qquad \text{(Eq. 1.9)}$$

Where M and p are the mass and momentum of the struck particle before collision; p_n and p'_n are the momenta of the incident and scattered neutron, *i.e.* p_n-p'_n=$\hbar q$.

Thus, the energy distribution of the scattered neutrons is directly related to the distribution of particle momenta parallel to the wavevector transfer.

DOI:10.14753/SE.2014.1974

Time of flight techniques require that the energy of either the incident or the scattered neutrons is well defined. On VESUVIO this is accomplished by using a gold foil analyser whose neutron absorption resonance occurs at 4.9 eV. This defines the final energy of the scattered neutron as 4.9 ± ~0.14 eV. The detectors at forward scattering angles are cerium doped Yttrium Aluminium Perovskite (YAP) γ-ray detectors (**Figure 1.33**) [230,231]. Back-scattering detectors are ^{6}Li doped ZnS scintillators. ^{6}Li readily absorbs neutrons and emits α particles (^{4}He).

$$^{6}Li + n \rightarrow {}^{3}H + {}^{4}He \qquad \text{(Eq. 1.10)}$$

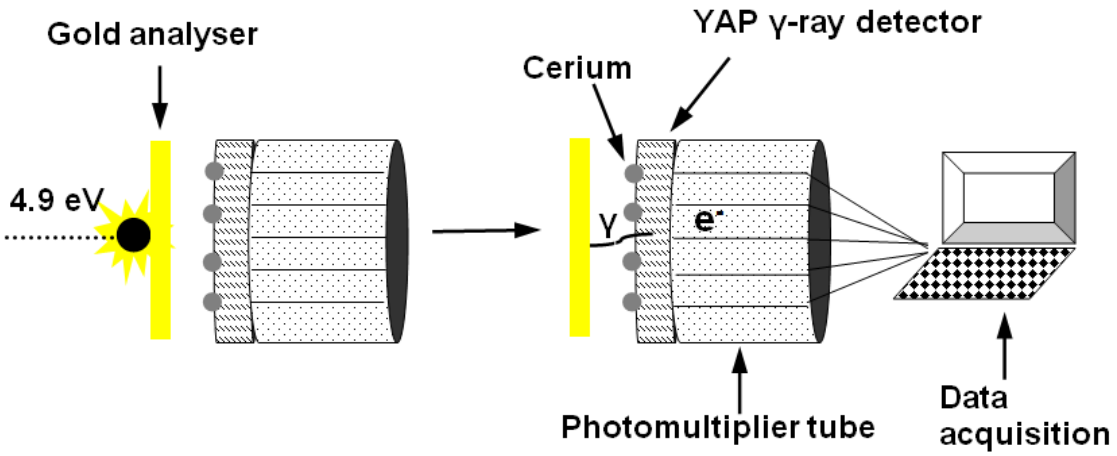

Figure 1.33 Schematic of the YAP detector and gold analyser used on VESUVIO forward scattering detector banks. The gold foil absorbs neutrons (black sphere) with final energy of 4.9±~0.14 eV and emits a γ cascade which is detected by the YAP detector. The detector sends electronic signals through the photomultiplier tube to reach the final data acquisition.

When the gold foil absorbs neutrons in the 4.9 eV resonance it emits a γ-ray cascade which can be detected [230]. There is also a secondary gold foil which can be placed between the sample and detectors. The VESUVIO data is obtained by taking the differences between spectra produced with the secondary gold foil in and those produced with it out (**Figure 1.34**) [232]. This gold foil cycling technique, also called double difference, not only removes detector efficiency-drifts and gamma background but also greatly improves the resolution function [232].

The standard expression for the count rate in an inverse geometry TOF spectrometer for a system of N identical atoms scattering neutrons into a detector subtending solid angle $d\Omega$ is:

DOI:10.14753/SE.2014.1974

$$C(t) = 2\left(\frac{2}{m}\right)^{1/2} \frac{E_0^{\,3/2}}{L_0} I(E_0) D(E_R) N \frac{d^2\sigma}{d\Omega dE_1} d\Omega \qquad \text{(Eq. 1.11)}$$

Where

$$E_0(E_1, t) = \frac{m}{2}\left(\frac{L_0 \nu_1}{\nu_1 t - L_1}\right)^2 \qquad \text{(Eq. 1.12)}$$

which defines the incident neutron energy E_0 in terms of scattered neutron energy E_1 and time of flight t; $D(E_R)$ is the probability that a neutron of energy E_R is detected; $\frac{d^2\sigma}{d\Omega dE_1}$ is partial differential scattering cross-section.

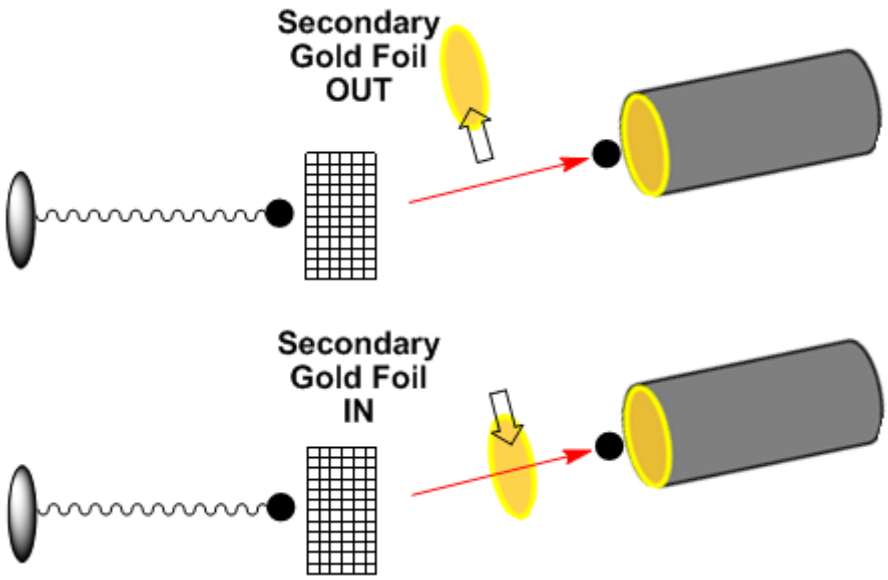

Figure 1.34 Illustration of gold foil recycling technique used on VESUVIO. In the secondary (gold foil out) mode the gold foil is moved out of the final flight path between the sample and detectors and in the primary (foil in) mode the foil is moved into the final flight path. During a data collection period the secondary gold foil is moved in and out many times.

At sufficiently high momentum transfer the IA is exact to interpret neutron data. For a system that has atoms of different mass M the count rate is expressed with the sum Σ:

$$C(t) = 2\left(\frac{2}{m}\right)^{1/2} \frac{E_0^{\,3/2}}{L_0} I(E_0) D(E_R) \sum_M N_M \frac{d^2\sigma_M}{d\Omega dE_1} d\Omega \qquad \text{(Eq. 1.13)}$$

DOI:10.14753/SE.2014.1974

Where N_M is the number of atoms of mass M; $\frac{d^2\sigma_M}{d\Omega dE_1}$ is partial differential scattering cross-section for mass M.

The dynamic structure factor for atoms of mass M is

$$S_M(q,\omega) = \int n_M(p)\delta\left(\omega + \frac{p^2}{2M} - \frac{(p+q)^2}{2M}\right)dp = \frac{M}{q} J_M(y_M, \hat{q})$$

(Eq. 1.14)

Where q is momentum transfer; ω is kinetic energy transfer; $n_M(p)$ is the atomic momentum distribution for mass M; y_M is the Westscaling factor defining the nuclear Compton scattering profile $J_M(y_M, \hat{q})$ of mass M and is defined as

$$y_M = \frac{M}{q}\left(\omega - \frac{q^2}{2M}\right)$$

(Eq. 1.15)

$J_M(y_M, \hat{q})$ is the probability distribution of the momentum component of mass M along the direction of $\hat{q}$. In isotropic samples such as liquids and powders, all directions are equivalent and the dependence on $\hat{q}$ can be ignored.

The count rate equation can then be expressed with Compton scattering profile:

$$C(t) = \frac{E_0 I(E_0)}{q} \sum_M A_M M J_M(y_M)$$

(Eq.1.16)

Where A_M is the amplitude of scattering from each peak and

$$A_M = \frac{2}{L_0} D(E_R) \sqrt{\frac{2E_R}{m}} \Delta\Omega N_M {b_M}^2$$

(Eq. 1.17)

Where b is the nuclear scattering length.

One approximation made in the data analysis is that the resolution can be incorporated as a single convolution in t space, with a different resolution function $R_M(t)$ for each mass.

$$C_m(t) = \left[\frac{E_0 I(E_0)}{q} \right] \sum_M A_M M J_M(y_M) \otimes R_M(t) \qquad \text{(Eq. 1.18)}$$

The second approximation is that $J_M(y_M)$ is assumed to have a normalised Gaussian form

$$J_M(y_M) = \frac{1}{\sqrt{2\pi\sigma_M{}^2}} \exp\left(\frac{-y_M{}^2}{2\sigma_M{}^2} \right) \qquad \text{(Eq. 1.19)}$$

Where σ_M is the Gaussian width of each peak in momentum (y_M) space to be fitted along with A_M [226,227].

Determination of momentum distribution $n(p)$ of light atoms, i.e. H, D, ^{3}He, ^{4}He, Li, is usually done on forward scattering spectra where their peak is well separated from peaks of other masses after correction for gamma background [233] and multiple scattering [234]. The spectra are then transferred to momentum space and the fitted widths σ_M in momentum space (as in Eq. 1.19) are obtained by fitting Eq. 1.11 to the data.

With respect to application, VESUVIO has successfully characterised the nuclear momentum distribution of a range of light-atom-containing systems, such as H_2/D_2 and H_2O/D_2O mixtures [235,236], H_2O in differing phases [237,238] and confinements [239,240], ^{3}He [241] and ^{4}He [242-244], among others.

Determination of momentum distribution $n(p)$ of heavy atoms is done on back scattering spectra after correction for gamma background and multiple scattering, in addition to subtraction of sample container background signal. VESUVIO has also been used to successfully characteris heavier atoms, including: O, Na and Si through investigation of NaH in both bulk material and encapsulated nanoparticles within silica gel (SiGNaH) [245].

The backscattering NCS spectra consist of peak contributions from each heavy atom in the sample. However, as the atomic mass increases the peak positions become more closely-spaced and a progressive suppositioning of peaks results. The resultant convoluted peak then needs to be separated into constituent peaks for each atom [230]. For systems containing heavier masses that are not well separated the following relationship is used [227]:

$$\frac{A_x}{A_y} = \frac{N_x b^2{}_x}{N_y b^2{}_y} = \frac{N_x \sigma_x}{N_y \sigma_y} \qquad \text{(Eq. 1.20)}$$

Where N is number of each atomic species in the sample; σ is neutron scattering cross-section.

The fitting command is written in such a way that only the fixed ratio of amplitudes is significant. When the stoichiometry of the sample is known, the amplitude ratio can be calculated as the product of the concentration of each atomic species and its neutron scattering cross-section. This ratio is used in back scattering fitting.

The position of the peak centre in time of flight space is determined from Eq. 1.8 and the following relation [226]:

$$\frac{v_1}{v_0} = \frac{\cos\theta + \sqrt{(M/m)^2 - \sin^2\theta}}{M/m + 1} \qquad \text{(Eq. 1.21)}$$

Where M is the atomic mass; m is neutron mass; θ is the scattering angle.

σ_M is then obtained in the same way as is done for light atoms. σ_M can be converted to kinetic energy or equivalent harmonic oscillator frequency.

1.8.1.3 Neutron diffraction

Neutron diffraction uses neutron scattering to obtain a diffraction pattern that provides information on the structure of a material. Different from NCS, slow neutrons are used and there is no energy (momentum) transfer, hence neutron diffraction is also labelled elastic neutron scattering (ENS). Neutrons are scattered by the atomic nucleus, providing the most direct insight into the position and motion of atoms, both as individual particles (self-scattering) and as pairs of particles (distinct scattering); the neutron probes directly the site-site correlation functions between atomic centers [224].

In order to track and characterise effects related to the typical spacing between atoms (~1-2Å), it is necessary to use comparable neutron wavelengths. At this wavelength the neutron energy is fortunately well away from any nuclear resonance energies, so there is no angular momentum transfer in the scattering process [225]. Impinging on a crystalline sample, neutrons will scatter under a limited number of well-defined angles according to Bragg's law (**Figure 1.35**).

DOI:10.14753/SE.2014.1974

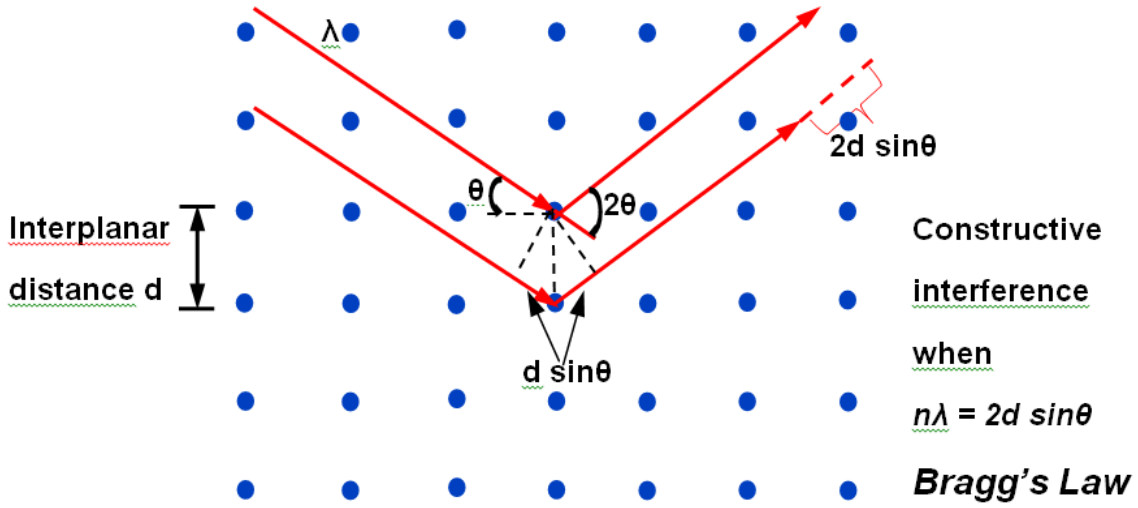

Figure 1.35 Illustration of application of Bragg's law to a diffraction event. Two parallel waves of identical wavelength λ impinge at angle θ on a crystalline solid with lattice planes separated by interplanar distance d and are scattered off two atoms. If the wave path difference $2d\sin\theta$ equals an integer multiple of λ, constructive interference occurs.

Bragg's law describes the condition for constructive interference from successive crystallographic planes of the crystalline lattice [246]:

$$2d\sin\theta = n\lambda \qquad \text{(Eq. 1.22)}$$

Where θ is scattering angle; n is an integer determined by the order given; λ is the wavelength.

A diffraction pattern is obtained by measuring the intensity of scattered waves as a function of scattering angle. Very strong intensities known as Bragg peaks are obtained in the diffraction pattern when scattered waves satisfy the Bragg condition, allowing the interplanar distance d to be calculated.

Time of flight is also used in neutron diffraction experiments for measuring the neutron velocity or wavelength. Neutron velocity and wavelength are convertable through the de Broglie wavelength equation:

$$\lambda = \frac{h}{m_n v} \qquad \text{(Eq. 1.23)}$$

Where h is Planck's constant; m_n is the mass of the neutron; v is its velocity.

The conversion between wavelength λ, energy E, wave vector ($k = \frac{2\pi}{\lambda}$), time-of-flight (TOF) and temperature T is as follows [225]:

λ [Å] = 0.395603 × 10^{-2} TOF (TOF in [μs/m]) (Eq. 1.24)

TOF [μs/m] = 252.778λ (λ in [Å]) (Eq. 1.25)

E [meV] = 81.8042/λ^2 (λ in [Å]) (Eq. 1.26)

= 2.07212k^2 (k in [$Å^{-1}$]) (Eq. 1.27)

= 0.0861734T (T in [K]) (Eq. 1.28)

The Near and InterMediate Range Order Diffractometer (NIMROD) (**Figure 1.36**) at the ISIS pulsed neutron and muon source (RAL, Harwell, UK) is designed for structural studies of disordered materials and liquids on a continuous length scale ranging from <1 Å to >300 Å maintaining subatomic distance resolution ~ 0.1 Å. This capability is achieved by matching a low and wider angle array (0.5° - 40°) of high efficiency neutron ^{6}Li doped ZnS (Ag) scintillation detectors (**Figure 1.37**) to the broad band-pass radiation delivered by a hybrid liquid water and liquid hydrogen neutron moderator assembly [247].

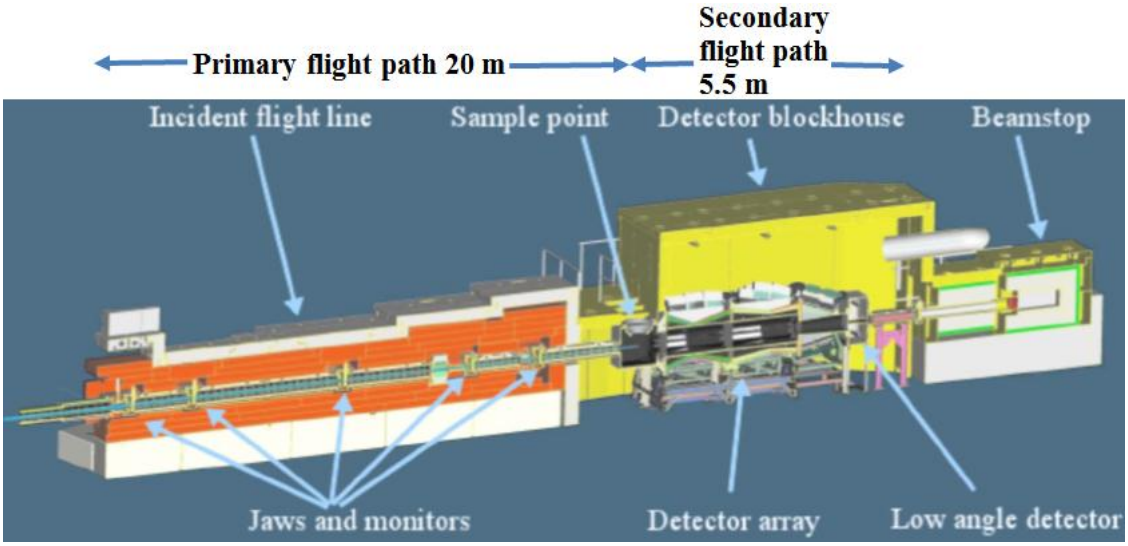

Figure 1.36 Cutaway diagram of NIMROD showing its principal structural components [247]. The components in NIMROD's yellow 'block house' are amplified in **Figure 1.37**.

The quantity measured in a neutron diffraction experiment is the Total Structure Factor $F(Q)$ where Q is the magnitude of the momentum transfer vector of a scattered neutron, or scattering vector, and is defined as follows:

DOI:10.14753/SE.2014.1974

$$Q = \frac{4\pi \sin\theta}{\lambda} \qquad \text{(Eq. 1.29)}$$

Where 2θ is the scattering angle; λ is the incident neutron wavelength.

The broad spectral range of the pulsed neutron source enables short-wavelength neutrons to be used to access high-Q (~31 Å^{-1}) and high structural resolution ~ 0.1 Å and long-wavelength neutrons for low-Q (~0.02 Å^{-1}) and long length scale structural correlations of > 300 Å [247].

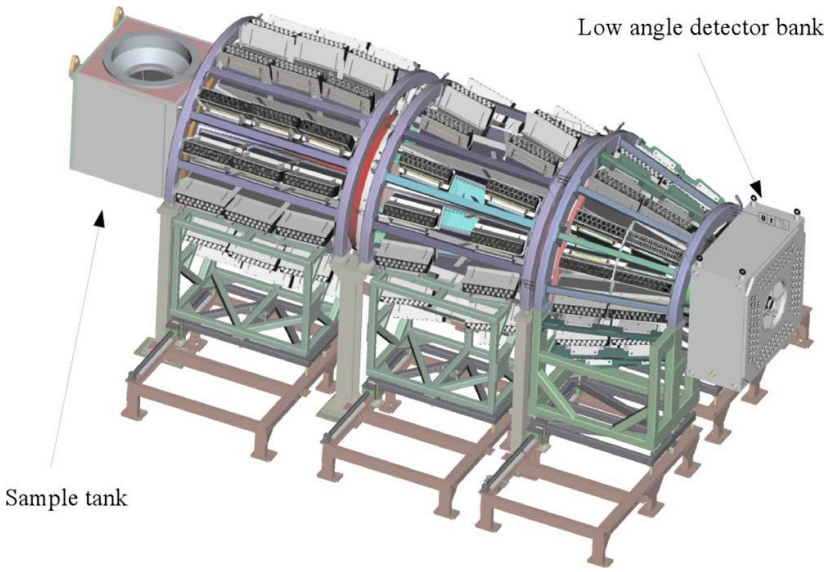

Figure 1.37 Overview of NIMROD's sample tank and secondary flight path vacuum tank and detector module distribution. The vacuum provides a clean path for the neutrons from sample to detectors. Next to the sample tank are 61 wide angle (3.5°-40°) detector modules (grey rectangular boxes) mounted in 7 rings around the beam axis. There are 24 modules in the low angle (0.5°-2.2°) detector bank [247].

The Total Structure Factor $F(Q)$ is defined as [248]:

$$F(Q) = \sum_{\alpha \le \beta} (2 - \delta_{\alpha\beta}) c_\alpha c_\beta b_\alpha b_\beta \left[S_{\alpha\beta}(Q) - 1 \right] \qquad \text{(Eq. 1.30)}$$

Where c_α and c_β are the concentrations of element α and β; b_α and b_β are their corresponding neutron scattering lengths; $S_{\alpha\beta}(Q)$ are the partial structure factors corresponding to the pairwise correlations between element α and β; $\delta_{\alpha\beta}$ is the Kronecker delta function to avoid double counting interactions between like-atom pairs.

Structure Factor $S(Q)$ commonly used in Small Angle Neutron Scattering (SANS) technique can also be derived as the normalised $F(Q)$.

The total radial distribution function $g(r)$ is the Fourier transform of $F(Q)$:

$$g(r)-1=\frac{1}{(2\pi)^3\rho}\int_0^\infty 4\pi Q^2 F(Q)\frac{\sin Qr}{Qr}dQ \qquad \text{(Eq. 1.31)}$$

1.8.2 Coherent Terahertz Spectroscopy (CTS)

The terahertz (THz) region of the electromagnetic spectrum (**Figure 1.38**) is loosely defined as the frequency range from ~0.1 to 10 THz [249]. This part of the electromagnetic spectrum has been traditionally less well explored and was once dubbed the 'terahertz gap' because of the lack of compact, high-power, low-consumption, solid-state coherent sources and efficient detectors [250]. Despite this, the THz region has attracted attention for potential high impact applications, especially in imaging as THz radiation is non-ionising. It only excites rotational and low-energy (collective) vibrational states of molecules while leaving the electronic state unaltered. Hence, terahertz radiation is inherently safer than X-rays with respects to non-destructive nature [251].

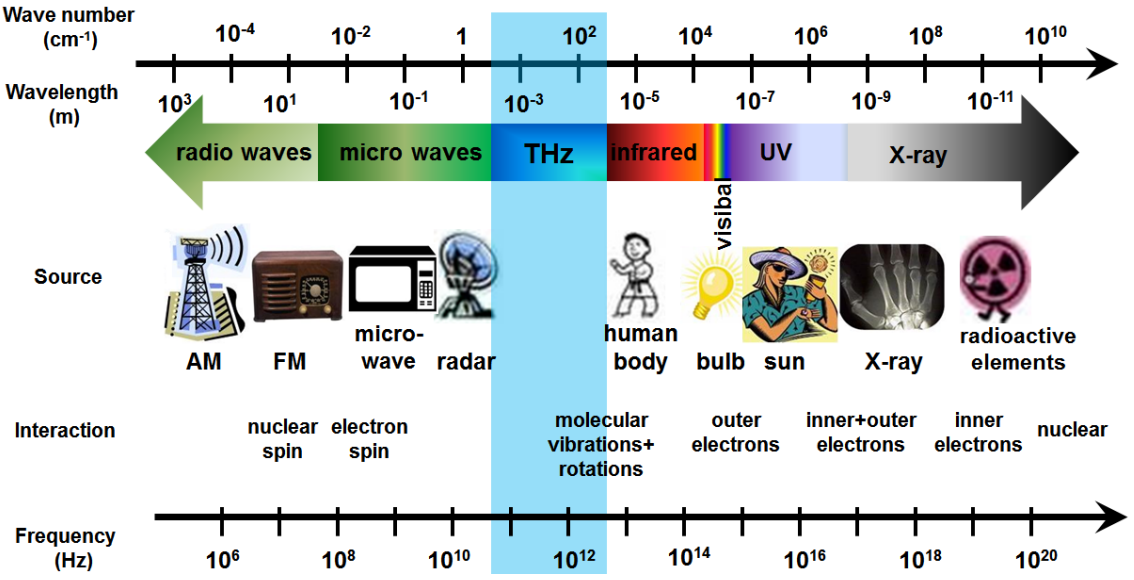

Figure 1.38 Illustration of the electromagnetic spectrum, quantified using differing units and highlighting the THz region (blue shadow). Several exemplary energy sources, size-scaling and phenomena are provided to denote the differing energies spanning the electromagnetic spectrum.

Rapid technological development for the generation and detection of coherent THz radiation over the past ~20 years has allowed this (relatively) unexplored region - traditionally relegated to the preserves of physicists and engineers - to become a useful

analytical tool accessible to users in many areas spanning the physical, materials and biological sciences [252].

CTS is unique in that it is able to characterise extremely low energy phenomena (i.e. ~10^{-1} to 10^{2} meV), including elusive vibrational modes involving whole molecule collective motions and interfacial dynamics (**Figure 1.38**). In addition, the time-gated radiations sources can easily be adjusted to the femtosecond (fms, 10^{-15} s) timescale, facilitating ultra-short time resolved measurements of dynamic phenomena [253]. Although still in its infancy, CTS has been shown to be a powerful tool in the studies of gas phase phenomena in the THz region; e.g. CO [254], N_2O [255] and propane [256]; crystalline material, e.g. indomethacin [257].

Combining CTS with modern computational modeling allows for quantitative assignment of the cartesian nature of the vibrational modes observed, and an overall more coherent understanding of the THz spectra [258-264]. Related studies on macro-biomolecules, DNA [265,266], solvent and solution dynamics [267,268] have also been advanced using CTS. Work in solid state transformation[269,270] has already demonstrated the potential for CTS as a useful addition to other solid state techniques including DSC, solid-state NMR and XRD [252]. It can be said without exaggeration that CTS is suitable for the studies of matters in all forms.

1.8.3 Computational Modeling

The intention of a scientific inquiry is to obtain an understanding and control of some parts of the universe. However, the universe is not so simple that it can be grasped and controlled without abstraction. Abstraction consists in replacing the parts of the universe by a model of similar but simpler structure [271]. Abstract models can be considered as the starting point of theory.

The importance of molecular modeling is represented by two of the Nobel Prizes:

1. The 1998 Chemistry Nobel Prize was awarded to Pople and Kohn for their ‘development of computational methods’ and ‘density functional theory.’
2. The 2013 Chemistry Nobel Prize was awarded to Karplus, Levitt and Warshel for the ‘Development of multiscale models.’

DOI:10.14753/SE.2014.1974

Most molecular and materials modeling involves three stages. In the first stage a model is constructed to describe the system, including inter-atomic bonding and intra-/inter-molecular interactions. The second stage is calculation, wherein an approximation describing the laws of physics/chemistry to be applied to the model(s) is then selected to evaluate the system. The two most common approximations are classical mechanics (known as molecular modeling) and quantum mechanics, including *ab initio* and density functional theory (DFT). At the third stage, the results of the calculation must be extracted, tabulated and analysed to ensure it has been accurately completed. Finally, the results must be 'translated' and transformed back to the relevant physics or chemistry of the phenomenon under investigation (i.e. spatial orientation of atoms → atomic structure; energetics → stability; dynamics → mechanical properties) [272].

With the emergence of supercomputers and ever-more economical computing, *ab initio* and especially DFT computations [273,274] have become a viable alternative to characterising (bio)molecular and material systems, advancing our understanding of the universe and allowing rational design of novel materials to help us meet the challenges of tomorrow.

DOI:10.14753/SE.2014.1974

2 DISSERTATION OBJECTIVES

Glass ionomer cements (GICs) have been in use for over 40 years and show promise for continued evolution in extensive applications spanning dentistry to orthopedics, and beyond. The existing body of literature on GICs covers a broad range of approaches and techniques, all with common focus on the effective resolution of its structure, setting mechanism and final chemical, physical and mechanical properties as well as its biocompatibility. Current descriptions of GICs are as a composite of unreacted glass particles sheathed in silica gel and embedded in a polyacrylate salt gel matrix. They are the reaction product of an acid-base reaction between the liquid-polymer and powder-glass components. Interphase bonding is driven by the formation of Al^{3+}/Ca^{2+} - polyacrylate salt bridges at glass particle surfaces. Silica gel ($Si(OH)_4 \bullet X(H_2O)$) and various phosphates ($H_x(PO_4)^{(3-x)-}$, with x = 0-3) also form an inorganic network contributing to the long-term mechanical properties. GICs' inherent and durable adhesion results from an ion-exchange interface formed between GICs and teeth or bones. Fully set GICs are hard materials with sufficient service-strengths, yet their brittleness restricts them to non-load bearing applications. The salt bridge interphase and interfacial bonding is responsible for the brittleness evidenced by preferential crack-propagation along interfaces under material failure. Extensive characterisation of the Al-polyacrylate salt bridge using differing techniques (IR, NMR, etc.) has led to the conclusion that a portion of the Al coordination evolves from IV→V→VI during cementation, driving relevant time-dependent property changes of GICs. Specifically, maximising Al(VI) coordination and cross-linking was thought to be most desirable for increasing strength. However, several recent works evidence GICs as being over-crosslinked, and potentially the underlying aspect of their observed low fracture toughness (i.e. brittleness); increase of strength at the detriment of toughness is well established in materials science.

DS/ISO/R 1565:1978 - directed mandates have orphaned material and mechanical characterisations of GICs to the post-setting domain (i.e. > 24 hours), whilst atomistic descriptions are severely lacking or entirely absent.

DOI:10.14753/SE.2014.1974

Based on the current state and challenges on GIC research, the objectives of this dissertation are as follows:

1. To undertake an exhaustive survey of all relevant literature on GICs and dental materials towards formulation of an agenda-changing research program;

2. To rationally characterise the microscopic structure, setting dynamics in commercially available GICs;

3. To resolve atomistic origin of fracture toughness towards rational characterisation and design of such materials for optimised clinical performance;

4. To pioneer the application of novel experimental techniques affording structural, energetic and temporal resolution not previously attained for GICs.

3 MATERIALS AND METHODS

Conventional acid-base setting GICs were investigated in this trans-disciplinary work. This work is composed of three series of studies:

1. Mechanical testing and fractography;
2. Neutron experiments;
3. Complementary experiments.

The materials and methods used in each series will be described separately.

3.1 Mechanical testing and fractography

3.1.1 Sample preparation

A commercial conventional acid-base reaction setting GIC (0807231, Fuji IX capsule, GC, Tokyo, Japan) was used to prepare 10 pieces each of normal (2×10 mm) and miniature samples (0.2×1 mm) in purpose-made aluminium moulds. Following manufacturer's instructions, the capsule was shaken for 10s in an amalgam mixer, followed by insertion of the capsule nozzle into the mould, itself coated with paraffin oil to act as a separation medium. Care was taken to firstly touch the mould wall with the nozzle and then raise it slowly as the paste was extruded into the mould until it was overfilled, in order to eliminate trapped air. A similarly-lubricated glass slab was then put on top of the mould and held in place for 2 min for initial setting to occur at 20±2 °C. The environmental humidity was not controlled, more closely reflecting the variability of application conditions. The sample was then de-moulded and wrapped tightly in aluminium foil to maintain water-balance, and subsequently stored in an incubator at 37 °C for 7 days [275].

3.1.2 Micro- and nanoCT imaging and data analysis

The miniature samples were scanned before and after Hertzian indentation testing with X-ray microcomputed tomography (SkyScan 1172, Kontich, Belgium) using microfocused X-rays at 70 kV with a 0.5 mm thick Al filter. Micromorphological analyses were conducted on the scans using the instrument software (CTAn, SkyScan, Kontich, Belgium). Isometric voxel of 2 μm was used for image reconstruction. Segmentation of images at different grey levels was applied to visualise different phases

of the samples by their different X-ray absorption. Due to the nonlinear character of absorption-density functions, pores were easily detected while the porosity characteristics were determined numerically. Although glass particles could be visualised, they could not be detected by the software.

Two of the broken samples were scanned with nanocomputed tomography (SkyScan 2011, Kontich, Belgium) using microfocused X-rays at 40 kV with no filter. An isometric voxel of 0.39 μm was used for image reconstruction. To assess the accuracy of the μCT results, three 20 nm thick × 200 nm diameter VOIs were chosen on both nanoCT and μCT scans of the same sample for porosity parameter determination, with all results subsequently compared using a Student's t-test at 95% confidence interval [275].

3.1.3 Hertzian indentation test

Samples were tested resting freely on a 30% glass fibre-reinforced polyamide (nylon 6,6) (elastic modulus 10 GPa), substrate of 5 mm thickness × 10 mm diameter, using a universal testing machine (Z005, 121-001609, Zwick, Ulm, Germany). With the aid of a computer connected microscope (1-747-034, dnt digital microscope camera, Conrad, Budapest, Hungary) for facilitating accurate alignment, loading was applied centrally on the sample through a 100Cr6 steel ball bearing of 20 mm diameter (2 mm for the smaller samples) at a crosshead speed of 0.2 mm/min. The load vs. displacement progression was monitored to determine the load-point of material failure. The test was terminated promptly upon observation of a sudden drop in load, with the maximum load attained utilised as the effective failure load [275].

3.1.4 Complementary imaging

The larger samples were examined after mechanical testing with an optical stereo microscope (Meiji, China) at up to 90 × magnification, as well as with a scanning electron microscope (Hitachi S-2460N, Tokyo, Japan) at up to 1500 × magnification, under vacuum [275].

DOI:10.14753/SE.2014.1974

3.2 Neutron experiments

3.2.1 Neutron Compton scattering (NCS) experiments

NCS data were collected on the VESUVIO spectrometer (**Figure 1.31**) at ISIS in March 2011, October 2011 and March 2013. Calibration was first done by measuring the empty beam and the empty sample holder. The empty sample holder spectrum was always subtracted from the back scattering spectra before any data analysis.

Optimal sample thickness results in scattering of ~10% of the incident neutrons, minimising multiple scattering. Optimal sample thickness for the current work was determined to be ~1 mm, calculated from following equations:

$$\exp(-N\sigma t) = 0.9 \quad \text{(Eq. 3.1)}$$

$$N\sigma t = 0.1 \quad \text{(Eq. 3.2)}$$

Where N is the number of molecules/cm^3; σ is the scattering cross-section/molecule in cm^{-2}; t is the sample thickness in cm.

Commercial G338 glass powder , the basis of commercial GIC powders, was loaded into a 5 cm × 5 cm cross-section, 1 mm deep aluminium sample holder till full. The holder was then put into VESUVIO's sample chamber and the temperature maintained at 300±0.1K throughout the measurements. Data was collected with consecutively numbered runs of 900 μamp-hour each for 12 h. Commercial liquid Chemflex (40% aqueous polyacrylic acid solution), the basis of commercial GIC liquid, was measured in the same fashion. A GIC composite sample was produced by hand-mixing the glass-powder and polymer-liquid at ratio of ~2.5 powder/liquid at room temperature (~295 K in the experiment hall laboratories). The mixture was immediately transferred to aluminium foil which was folded over the sample on a laboratory bench top and a lead brick was put on top for ~2 min to allow shaping (to sample can depth-dimension ~1 mm) and even spreading of the sample during initial setting. The sample was then sliced with a scalpel to just under cross-sectional sample-can dimensions (~ 4.75 cm × 4.75 cm) while the composite sample was still pliable. The aluminium-foil 1mm-GIC 'sandwich' was then put into the sample holder, sealed with a 1mm diameter indium (In) wire and fastened with nuts and bolts. The loaded and sealed sample holder was then placed in VESUVIO's sample chamber and the temperature maintained at 300±0.1K throughout the remainder of the experiment. Data was collected with consecutively numbered runs

of 90 µamp-hour (minimal data size with acceptable statistics and retaining time resolution for setting dynamics study) each for the first 48 hours and then 900 µamp-hour each from 48-72 h.

Data treatment and fitting routines followed that described in reference [227] as well as outlined in **Section I_8.1.2**. The only alteration made in this work was that for stoichiometric-fixing of the back scattering spectra, two sets of data analysis routines were used as there are 8 species other than H in the GIC composite cement exceeding the 7 species maximum capacity of the current data analysis routine. The first routine used the amplitude ratio of the 7 masses: 12, 16, 19, 23, 27, 29.3 (a combined mass determined from the Si/P amplitude ratio) and 40 (**Figure 3.1**), to obtain the NCS width values for C, O, F, Na, Al and Ca respectively. The second routine used the amplitude ratio of the 7 masses: 12, 16, 19, 25 (a combined mass determined from the Na/Al amplitude ratio), 28, 31 and 40, to obtain the NCS width values for C, O, F, Si, P and Ca, respectively. This procedure was repeated at each chosen time point.

The same procedure was repeated for experimental runs tracking setting in GIC composite cements at 280 K and 320 K for 24 h each.

The relative time scales of the experiment is shown in **Figure 3.2**. The time in hour below the horizontal line is the real setting time from the start of cement mixing. The neutron data collected continuously between two time points was summed up and assigned an average setting time (above horizontal line). For example, the 24 h cement data time-point is the total data collected from 18 h to 30 h. The starting point is assigned a 0.6 h (36 min) value as it took this much time to prepare the sample, load it in the instrument, allow temperature to settle (to 300K) and initiate data collection.

DOI:10.14753/SE.2014.1974

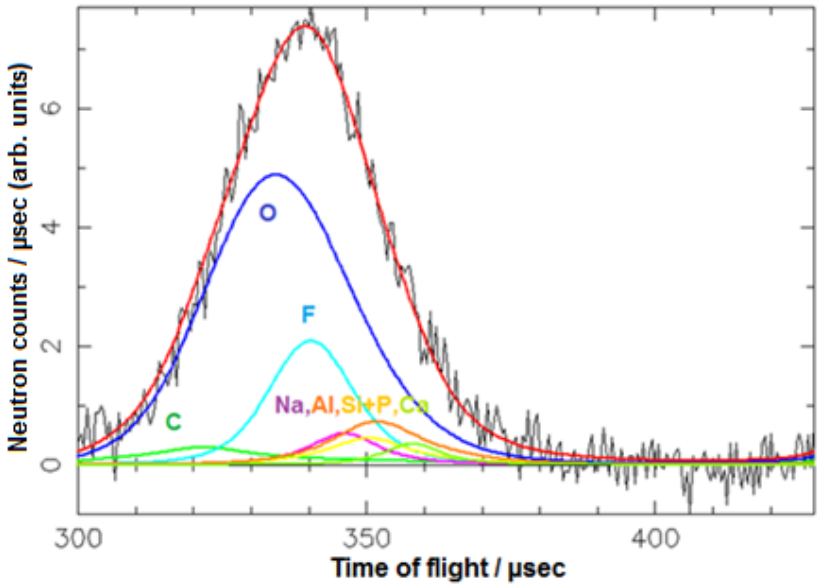

Figure 3.1 Stoichiometric fitting of back scattering data. The fit (red) of the corrected raw data (black) is deconvoluted into seven constituent peaks, each marked by their respective atomic symbols.

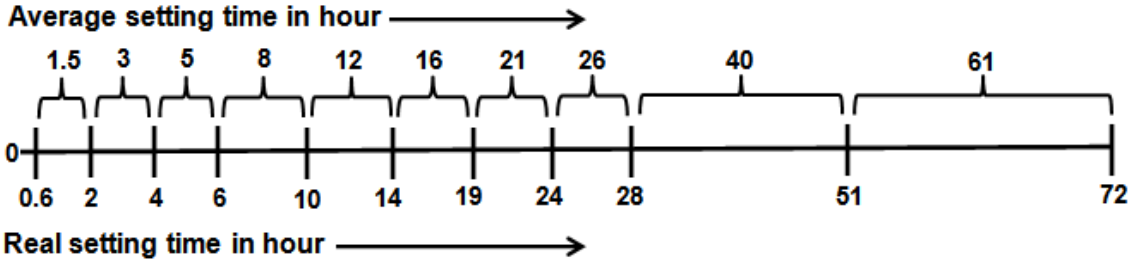

Figure 3.2 Time scale of NCS experiment. The time in hours below the horizontal line is the setting time in real time-space from the start of cement mixing. The neutron data collected continuously between two time points was summed up and assigned an average setting time above the horizontal line.

3.2.2 Neutron diffraction experiments

Neutron diffraction data was collected using the Near and InterMediate Range Order Diffractometer (NIMROD) at ISIS pulsed neutron source. Calibration was first done by measuring the vacuum chamber, the empty can and a vanadium reference. After the calibration, the glass powder and liquid were measured in the TiZr can, respectively. The glass powder and liquid were hand-mixed at 2.5 powder/liquid ratio at room temperature. The cement mixture was then transferred immediately to the TiZr can and put into the sample chamber. Measurements of the cement were performed for 24 h. Data treatment with Gudrun package [276] followed the routine described previously [277] as well as outlined in **Section 1_1.8.1.3**.

DOI:10.14753/SE.2014.1974

3.3 Complementary experiments

3.3.1 DSC measurement

The isobaric (constant pressure) heat capacity (C_p) of G338 glass powder was measured using a differential scanning calorimetry (Netzsch STA449C, Netzsch-Gerätebau GmbH, Germany) in the argon atmosphere. The sample was placed in a platinum crucible situated on a sample holder of the DSC at room temperature. The samples were held for 5 min at an initial temperature of 50 °C, and then heated at a rate of 20 °C/min to 600 °C, and then cooled back to 250 °C at 20 °C/min. After natural cooling to room temperature, the second upscan was performed using the same procedure. To determine the C_p of the sample, both the baseline (blank) and the reference sample (sapphire) were measured. To confirm reproducibility, the measurements for some samples were repeated to check for drift in the baseline.

GIC sample was produced at a powder/liquid ratio of 2.5 and the mixture was stored in distilled water at 37 °C after 1 h setting. The setting was terminated at 60 h by quenching it into liquid nitrogen. It was then ground into fine powder. The 60 h GIC powder was then measured with the same procedure as G338.

3.3.2 TEM measurement

TEM was performed at the NanoVision Centre at QMUL using SEM and TEM facilities. The G338 glass powder was dried before mounting. Care was taken to spread the powder into a very thin near monolayer on the sample stage.

3.3.3 CTS measurement

A quasi-optical (QO) transmissometer driven by a vector network analyser (VNA) was used to study the cementation process over the frequency domain of 220-325 GHz (0.22-0.325 THz) using a novel reflection setup (**Figure 3.3**).

DOI:10.14753/SE.2014.1974

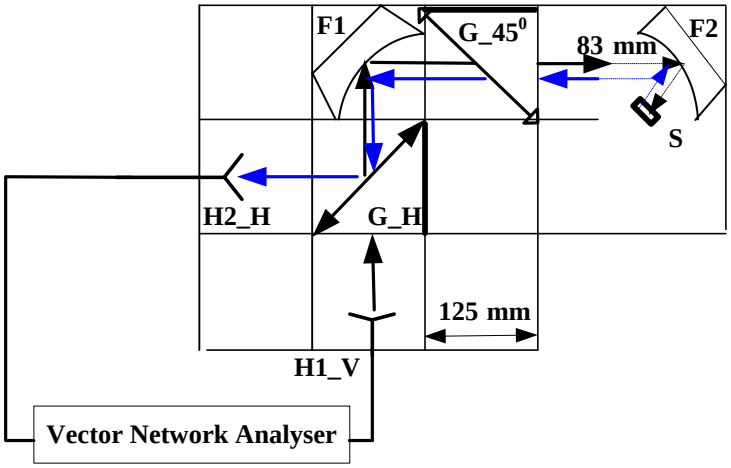

Figure 3.3 Schematic diagram of the quasi-optical transmissometer: H1 and H2 denote a pair of corrugated feed-horns transceiver. The designations V and H represent respectively linearly-vertical and horizontal polarised electric fields; F1, an ellipsoidal reflector, has a focal length of 250 mm; F2, a spherical mirror, has focal length 83 mm; G_H represents a wire-grid with horizontal polarisation and G_45^0 a wire-grid with 45^0 polarisation; S is the sample under test.

GIC cement was produced by hand-mixing G338 glass powder and Chemflex liquid at a powder/liquid ratio of 2.5 at room temperature. The sample was shaped into a disk of 11 mm diameter and 1.86 mm thickness by manual press-fitting into a Real TPX® cap (**Figure 3.4**). Setting time was recorded from the start of mixing. The sample holder is sealed to maintain the water content. This eliminates transmission signal fluctuation that would be attributed to water-based stoichiometric variation during curing. QO transmissometer scans at a resolution of 52.5 MHz were recorded continuously at 3-minute intervals for 30 hours. Measurements were then repeated on the glass and liquid components in isolation.

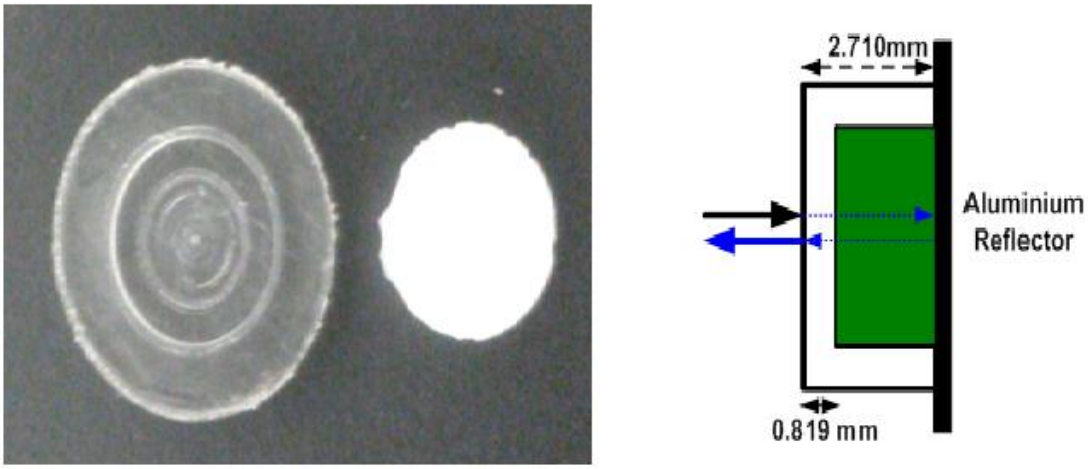

Figure 3.4 (left) Real TPX® cap and GIC sample; (right) schematic plot of TPX® cap and the samples under the test are fully filled in the green area.

DOI:10.14753/SE.2014.1974

3.3.4 Computational Modeling

Quantum chemical computations were undertaken with the Gaussian 09 program package (G09) [283]. Preliminary Al-coordination permutation models **Figure 3.5** were constructed to characterise the influence of axial and equatorial ligands on ^{27}Al-NMR shifts relative to the experimental standard ($AlCl_3 \bullet 6H_2O$). These models and the NMR standard were geometry-optimised using the DFT Becke-3-Lee-Yang-Parr correlation (B3LYP) method [279], employing the all-electron DGDZVP basis set [280]. NMR shifts were determined on the optimised structures using the well-established Gauge-Independent Atomic Orbital (GIAO) method [281] and compared to the shift of the standard. Secondary computations on these models were subsequently completed using the MP2(full) method [282] and DGDZVP basis set, with trends mirroring those emerging from the DFT computations.

In order to study the collective vibrational interaction between PAA and glass particles we have assembled many-atom organic-inorganic clusters based on the geometry-optimised *ab initio* model. Representative cement models were built with PAA oligomers attached via a Al(V) to a glass substrate with the composition of anorthite ($CaAl_2Si_2O_8$), modelled as a hydrated 8-unit molecular cluster ($Ca_8Al_{16}Si_{16}O_{64}H_{40}$, 164 atoms). A 78-atom, 396-electron, top-slice of this model characterised interfacial Al-coordination changes through stretching and compression of COO(-) ligatures, resulting in Td and Oh Al-coordination, respectively. Relative contributions to free-energy of each normal mode of vibration were plotted as a function of frequency and grouped by motion-types.

DOI:10.14753/SE.2014.1974

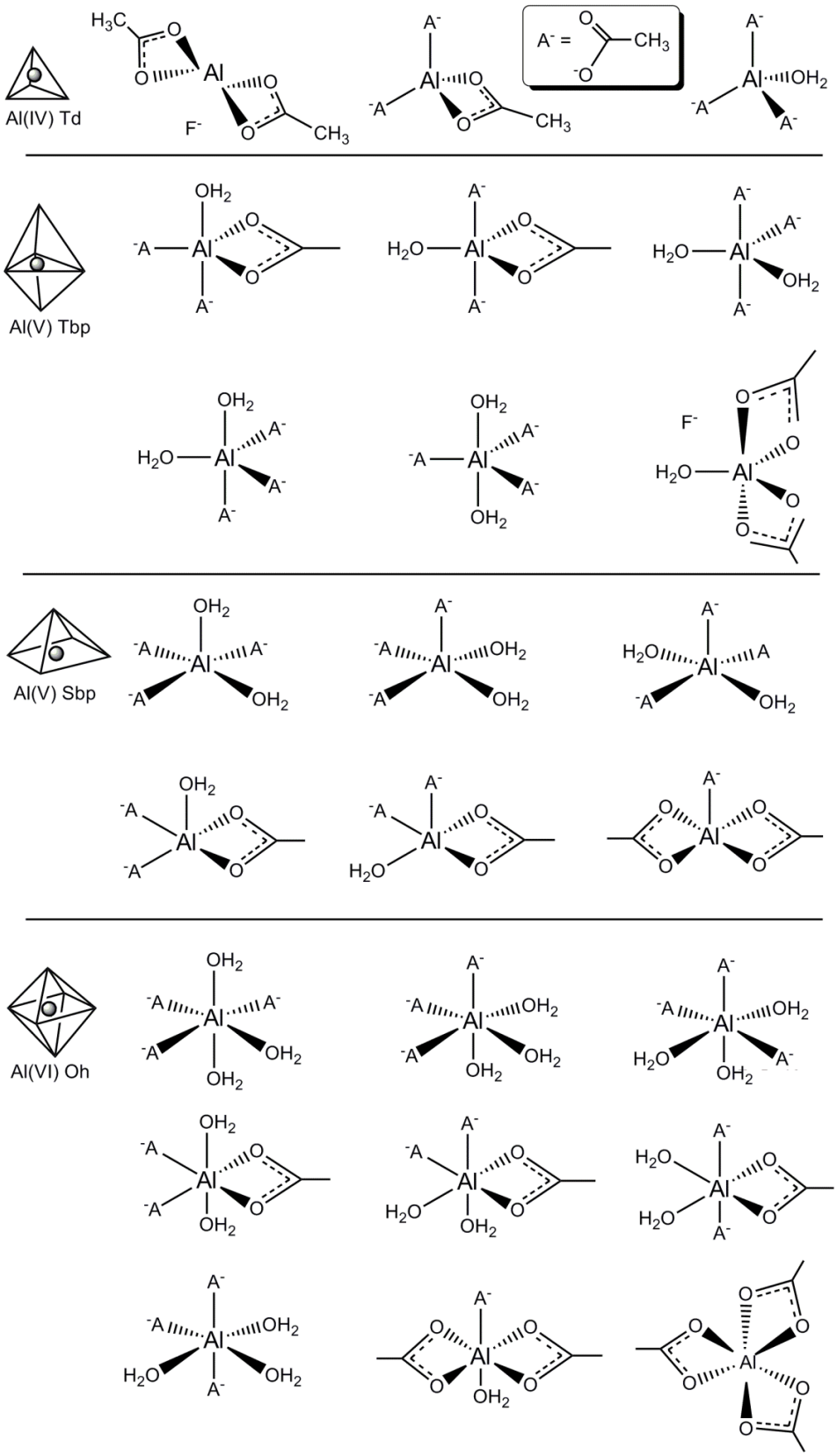

Figure 3.5 Tetrahedral (Td), trigonal bipyramidal (Tbp), square-based pyramidal (SBP) and octahedral (Oh) Al-coordination models with differing configurational permutations of ligating H_2O and carboxylic acid groups; the latter trialled in both mono-A^- and bi-dentate CH_3COO^- binding arrangements. All models are neutral, with F^- used to charge-balance as required.

DOI:10.14753/SE.2014.1974

4 RESULTS

4.1 Mechanical testing and fractography

4.1.1 Hertzian indentation test results

A representative force-displacement plot was shown in **Figure 4.1**. The highest force the samples could sustain before failure was determined from the plots and the means determined from these values. The mean failure load for the normal samples was 218.7 ± 52.1 N; the value and variability being consistent with, and representative of, the diverse conditions of clinical preparation, application and setting. For the miniature samples, a mean value of 35.3 ± 1.0 N was recorded.

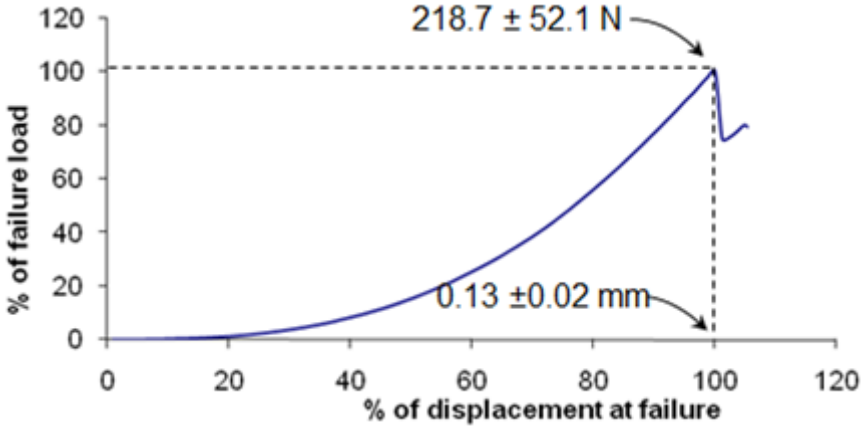

Figure 4.1 Typical force-displacement plot resulting from Hertzian indentation test, presented as % of failure load as a function of % displacement at failure [275].

4.1.2 µCT imaging

Figure 4.2 represents the 3-D microtomography of a portion of the fracture surface. Spheres are used to highlight the location of pores prior to crack propagated through them while the irregularly shaped recesses and dimples denote the sites where the glass cores from the opposing fracture-face were embedded in the matrix.

DOI:10.14753/SE.2014.1974

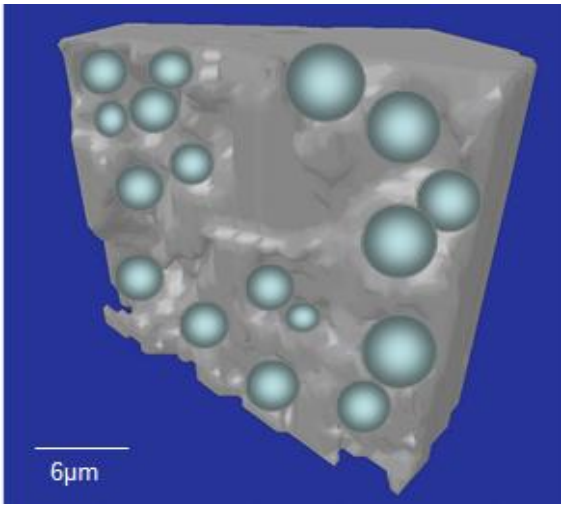

Figure 4.2 MicroCT mapping of the radial fracture surface, wherein greyish-cyan spheres highlight the distribution of pores on the fracture-surface. Dark grey recesses and dimples highlight the prefracture location of glass cores from the opposing fracture surface [275].

Figure 4.3 shows the "pore phase" in a sample after the Hertzian indentation test, as determined through the µCT methodology, using the differing X-ray absorption of open cracks and pores, with respect to the absorption of the matrix.

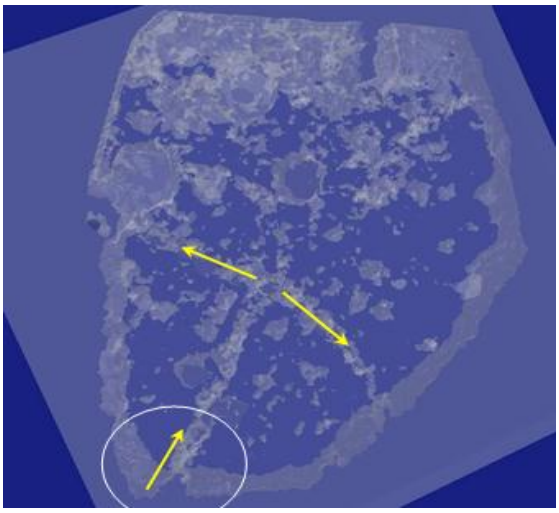

Figure 4.3 Segmented microCT of one dissected piece of a fractured GIC sample, with the fracture origin oriented towards the bottom (white circle). The image shows the pores and pore-phase (milky white) linked by micro-cracks. The crack originating from the bottom progresses at a ~60° angle up and to the right, until it is deflected left–right, to form a 'T-shaped' crack, effectively connecting the principal cracks and contributing to overall failure [275].

Figure 4.4 is the nanoCT image.

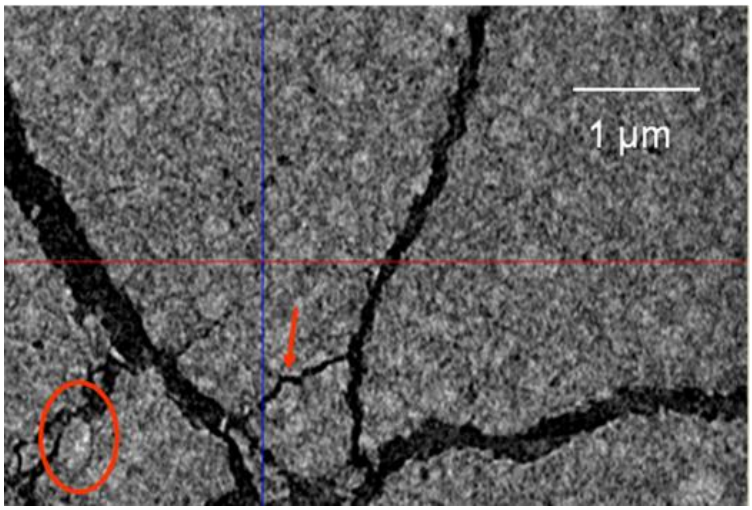

Figure 4.4 Nano CT image showing that microcracks propagating along the interface of the matrix and glass cores (arrow and oval) [275].

4.1.3 Complementary imaging

The optical and scanning electron micrographs are shown in **Figure 4.5**.

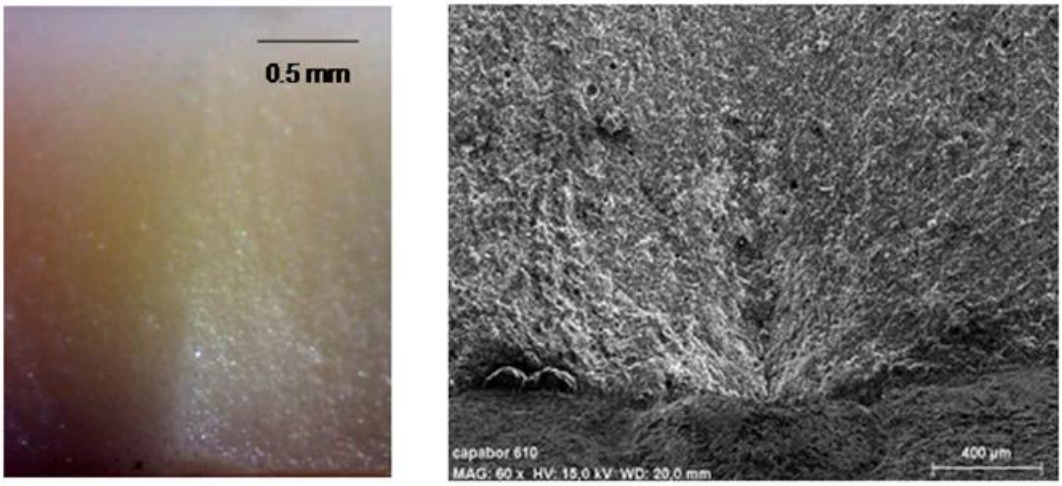

Figure 4.5 (a) Optical image showing the fracture origin at the middle of the bottom surface, with hackles radiating out from the origin; (b) scanning electron micrograph of the same specimen shows incomplete radial cracking, as well as the hackles that radiate out from the origin [275].

Figure 4.6 is the scanning electron micrograph of higher magnification ×400.

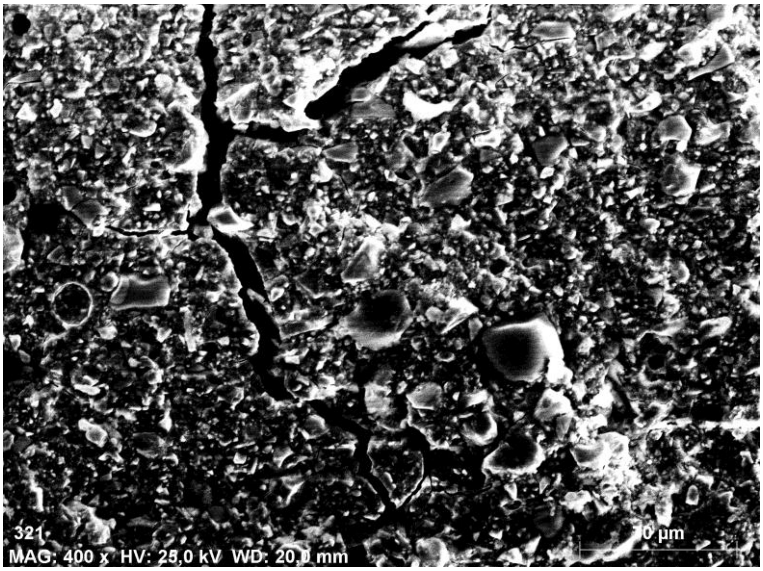

Figure 4.6 Scanning electron micrograph of the fracture surface at 400 × showing the glass cores exposed upon material fracture, with the microcrack propagating along the edge of the glass cores. The bar is 10 µm [275].

4.2 Neutron experiments

4.2.1 Neutron Compton scattering (NCS) experiments

The small mass of H leads to a broad energy distribution of the scattered neutrons that is well-separated from the scattering from heavier atoms, which appears as a near-elastic contribution [288]. Together with its large incoherent cross-section (**Figure 1.27**) hydrogen is an ideal candidate for NCS measurement with high accuracy. Thus, the forward scattering results are presented first.

4.2.1.1 Forward scattering

Figure 4.7 shows the corrected neutron time of flight spectra for 24 h cement collected on single banks of the forward scattering and back scattering detectors.

DOI:10.14753/SE.2014.1974

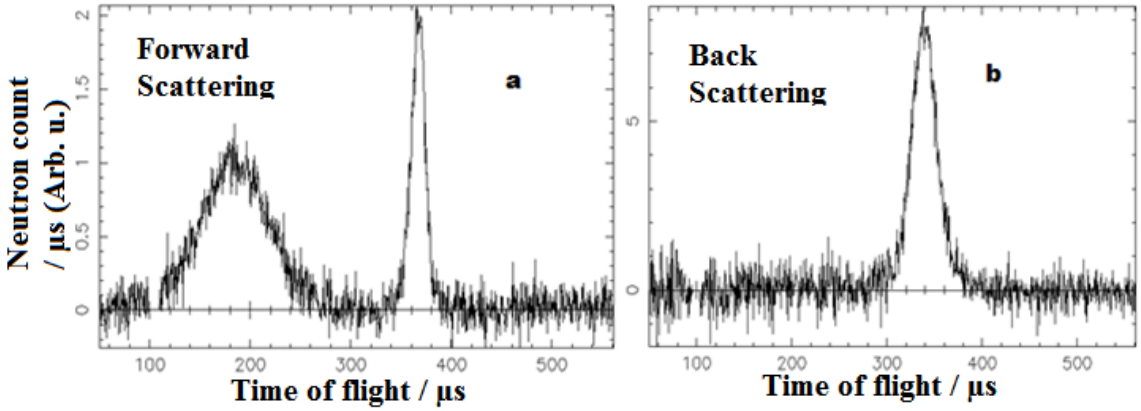

Figure 4.7 (a) sum of forward scattering data with angles 60-80˚ after the correction procedure for 24 h cement. The large peak at the lower time of flight is sole contribution of the scattering signal from H. The thin peak at the higher time of flight is the supposition of peaks from the heavy atoms; (b) sum of back scattering data with angles 150-170˚ after the correction procedure for 24 h cement. The only peak is the supposition of peaks from the heavy atoms.

Following the method outlined, the H peaks in the forward scattering spectra recorded over cementation were fitted and the neutron Compton profile (**Figure 4.8**) and radial momentum distribution (**Figure 4.9**) were determined and plotted.

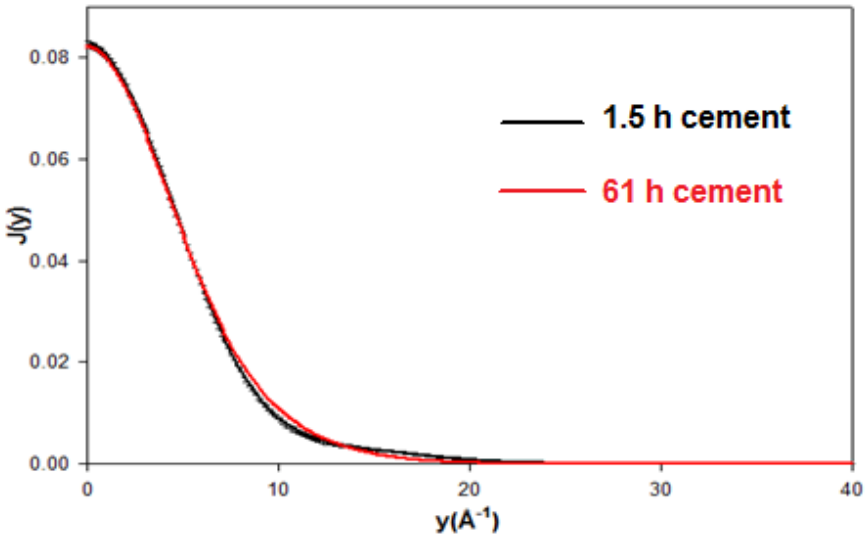

Figure 4.8 Neutron Compton profiles of 1.5 h (black) and 61 h (red) cements. The errors are shown as vertical lines but are too small to be seen. 61 h cement has a shift to higher *y* values.

DOI:10.14753/SE.2014.1974

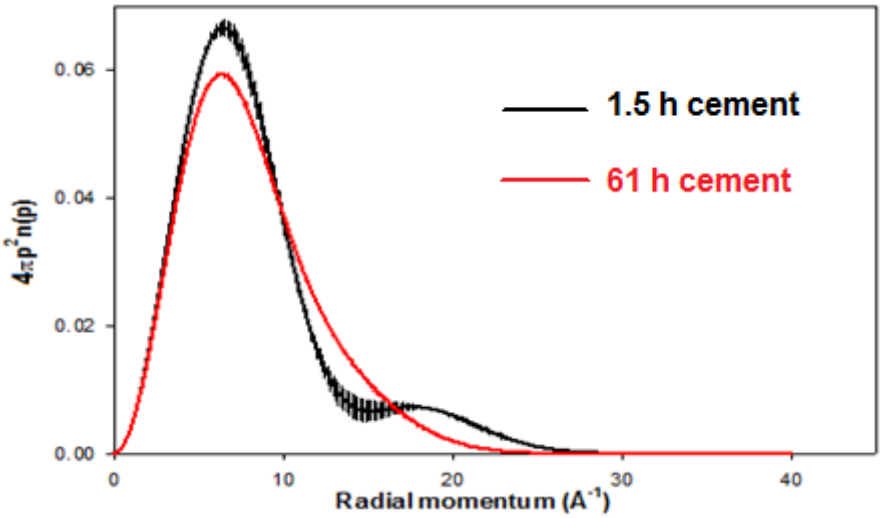

Figure 4.9 Radial momentum distributions of 1.5 h (black) and 61 h (red) cements. The errors are shown as vertical lines. 61 h cement has a shift to larger radial momentum values. The appearance of an oscillation in the momentum distribution for 1.5 h cement is characteristic of a population of protons that are coherently distributed in the ground state of a double well potential.

The determined proton NCS width, mean kinetic energy and oscillator frequency as a function of cementation time were tabulated in **Table 9**.

Table 9. Proton Compton profile widths, mean KE (kinetic energy) and OF (oscillator frequency) with standard deviation in bracket.

Cementation time	H width / $Å^{-1}$	Mean KE / meV	OF / cm^{-1}
0	4.93 (0.03)	152.40 (1.24)	1638.96 (13.30)
1.5 h	4.66 (0.07)	136.17 (4.09)	1464.36 (43.99)
3 h	4.81 (0.05)	145.08 (3.02)	1560.15 (32.44)
5 h	4.77 (0.06)	142.67 (3.59)	1534.31 (38.60)
8 h	4.65 (0.04)	135.58 (2.33)	1458.08 (25.09)
12 h	4.80 (0.04)	144.47 (2.41)	1553.67 (25.89)
16 h	4.80 (0.06)	144.47 (3.61)	1553.67 (38.84)
21 h	4.76 (0.04)	142.08 (2.39)	1527.88 (25.68)
26 h	4.82 (0.06)	145.68 (3.63)	1566.64 (39.00)
40 h	4.82 (0.03)	145.68 (1.81)	1566.64 (19.50)
61 h	4.81 (0.03)	145.08 (1.81)	1560.15 (19.46)

As both mean kinetic energy and harmonic oscillator frequency of the same atom are calculated from the Compton profile width squared, the three parameters have similar trend over time on different scales. Only the Compton width values as a function of time were plotted in **Figure 4.10** to show the overall trend uncovered.

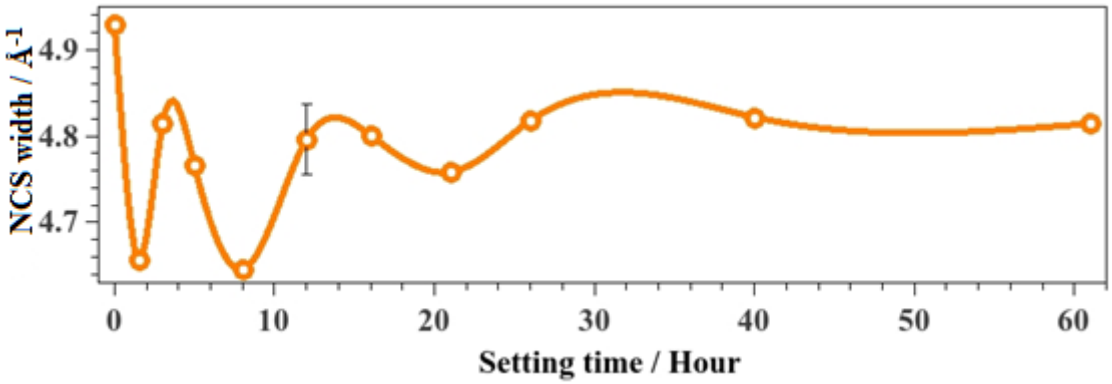

Figure 4.10 Determined NCS with values of H-atom (circles) and spline showing NCS wdith trend ($Å^{-1}$) as a function of setting time (Hours); a representative error bar is shown at 12 h.

The measured H NCS width at all three temperatures were co-plotted in **Figure 4.11** to show the temperature effect.

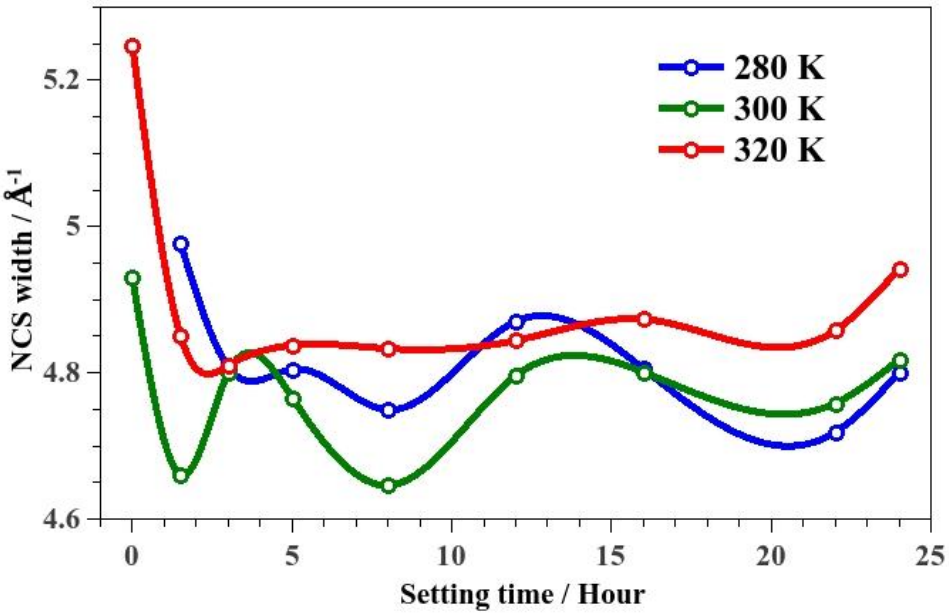

Figure 4.11 Measured NCS width values of H at 280 K (blue), 300 K (green) and 320 K (red) co-plotted as a function of setting time.

4.2.1.2 Back scattering

Since the separate components are not expected to change over time, the acid-polymer and glass-powder NCS data should also not change over time. An instrument reliability

and feasibility check was done by comparison of the acid-polymer and glass-powder data at different times. The corrected time of flight back scattering spectra after correction for gamma background and multiple scattering and subtraction of sample holder signal with error bars and fits of 3 h and 8 h acid polymers were shown in **Figure 4.12**. There was no significant difference between the spectra and the fits. The calculated mean kinetic energy values for O at the two times were 68 and 66 meV, respectively, which were not significantly different. **Figure 4.13** presented the case of glass powder and there was no significant difference between the spectra, the fits nor the mean kinetic energy values for O. The reliability of the instrument was thus confirmed.

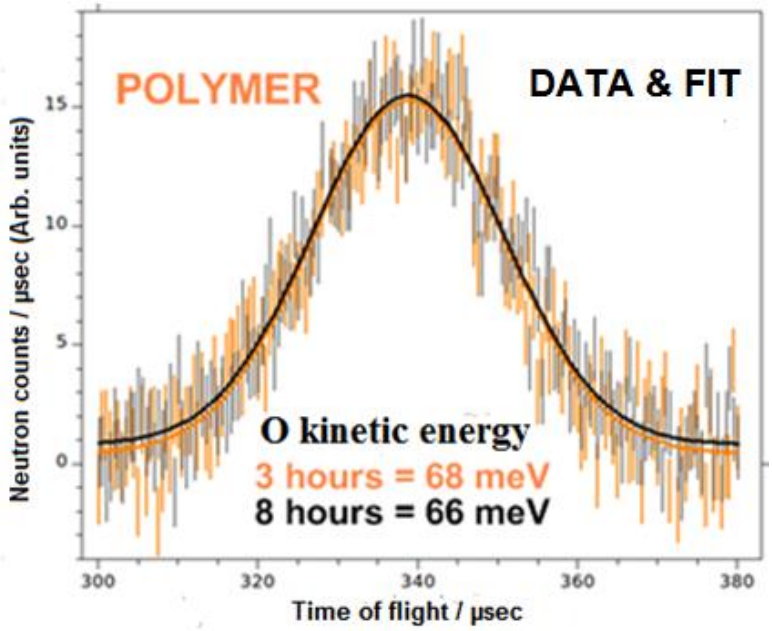

Figure 4.12 Corrected time of flight spectra for the acid-polymer with error bars and fits (solid lines) at 3 h (orange) and 8 h (black), as well as the mean O-atom kinetic energy values (meV).

These also served as references for judging changes occurring during setting. Since the residual glass and polymer remained unchanged, the variations observed in the cement related to developments at the organic-inorganic interface during the course of setting.

DOI:10.14753/SE.2014.1974

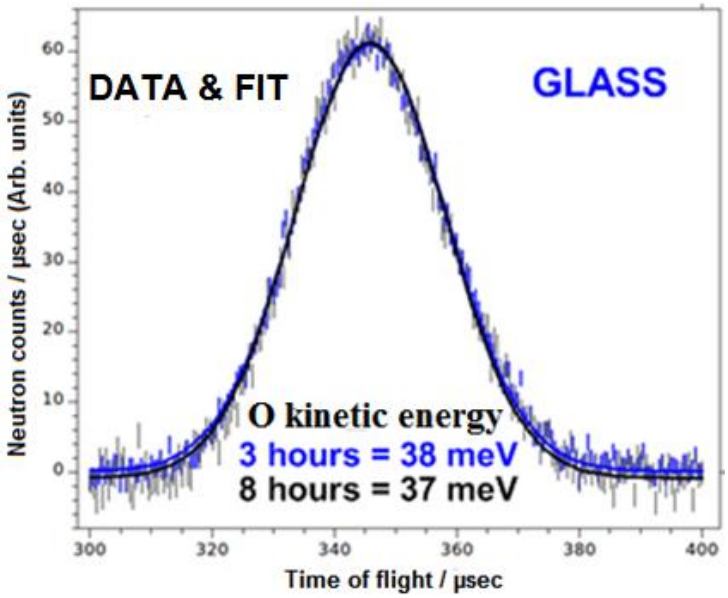

Figure 4.13 Corrected time of flight spectra for the glass powder with error bars and fits (solid lines) of 3 h (blue) and 8 h (black), as well as the O-atom mean kinetic energy values (meV).

The same was done for the corrected spectra and fits of 12 h and 61 h cements showing global changes in **Figure 4.14**. It was seen that NCS technique was able to capture these changes taking place during setting. This also made the subsequent deconvolution of the back scattering peaks into constituent peak contribution of each element and tracking the setting dynamics through the change of these elements meaningful.

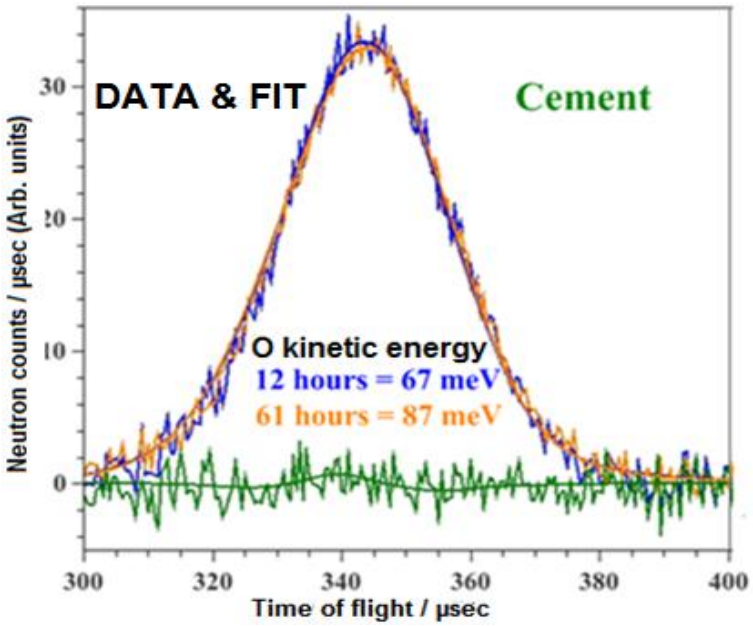

Figure 4.14 Corrected time of flight spectra and fit (solid lines) of 12 h GIC (blue), 61 h GIC (orange) and the difference of the spectra and fits as well as the calculated O mean kinetic energy values.

DOI:10.14753/SE.2014.1974

The Compton profile width values for the heavy atoms were tabulated in **Table 10**.

Table 10. Compton profile width values in $Å^{-1}$ for the heavy atoms with standard deviation in bracket.

Time	C	O	F	Na	Al	Si	P	Ca
0 h	14.75 (1.12)	12.26 (0.60)	8.58 (0.20)	12.50 (0.51)	14.06 (0.55)	20.10 (0.95)	16.26 (1.35)	11.85 (0.79)
1.5 h	11.57 (0.86)	10.24 (0.71)	9.42 (0.43)	12.30 (0.85)	14.11 (0.78)	15.52 (1.02)	17.04 (0.97)	17.96 (1.06)
3 h	11.12 (0.79)	12.21 (0.53)	9.48 (0.47)	14.95 (1.46)	16.89 (1.41)	16.00 (1.26)	17.92 (1.40)	17.07 (1.46)
5 h	12.15 (0.82)	12.61 (0.51)	9.58 (0.48)	13.50 (0.99)	18.43 (1.51)	16.65 (1.20)	19.03 (1.35)	17.25 (1.24)
8 h	12.50 (0.76)	13.45 (0.36)	10.35 (0.43)	12.59 (1.16)	17.11 (1.19)	16.36 (0.92)	15.61 (1.01)	17.83 (1.50)
12 h	12.77 (0.81)	13.07 (0.30)	9.10 (0.37)	12.64 (0.83)	16.16 (0.88)	16.32 (0.92)	17.95 (1.19)	13.98 (1.06)
16 h	11.43 (0.72)	12.53 (0.36)	9.75 (0.42)	14.34 (0.86)	17.43 (1.08)	17.72 (1.44)	17.79 (1.34)	15.03 (1.24)
21 h	13.62 (1.27)	13.40 (0.28)	9.71 (0.38)	10.37 (0.67)	17.34 (0.98)	16.83 (0.90)	17.41 (1.14)	15.33 (1.48)
26 h	11.79 (0.65)	13.70 (0.35)	10.48 (0.52)	12.24 (0.83)	17.35 (1.06)	17.41 (1.05)	17.50 (1.25)	13.55 (0.92)
40 h	14.04 (0.95)	14.14 (0.21)	9.71 (0.35)	13.23 (1.00)	16.64 (0.95)	17.50 (0.88)	17.35 (1.3)	14.50 (1.27)
61 h	12.30 (0.73)	14.88 (0.20)	9.89 (0.37)	11.85 (0.64)	17.98 (1.05)	17.56 (0.81)	18.07 (0.95)	14.56 (1.00)

Mean kinetic energy and harmonic oscillator frequency of each atom were calculated from the Compton profile width squared and were tabulated in **Table 11** and **Table 12**.

DOI:10.14753/SE.2014.1974

Table 11. Calculated mean kinetic energy in meV for the heavy atoms with standard deviation in bracket.

Time	C	O	F	Na	Al	Si	P	Ca
0 h	113.69 (17.26)	58.86 (5.76)	24.30 (1.12)	42.60 (3.48)	66.25 (11.06)	90.48 (8.55)	53.48 (8.88)	22.03 (2.94)
1.5 h	69.95 (10.40)	41.09 (5.70)	29.29 (2.67)	41.25 (5.70)	78.88 (12.93)	53.94 (7.09)	58.73 (6.69)	50.57 (5.97)
3 h	64.61 (9.18)	58.43 (5.07)	29.66 (2.94)	60.93 (11.90)	67.99 (9.46)	57.33 (9.03)	64.96 (10.15)	45.68 (7.81)
5 h	77.14 (10.41)	62.32 (5.04)	30.29 (3.04)	49.69 (7.29)	60.65 (6.61)	62.08 (8.95)	73.25 (10.39)	46.65 (6.71)
8 h	81.65 (9.93)	70.90 (3.80)	35.35 (2.94)	43.21 (7.96)	70.56 (8.74)	59.94 (6.74)	49.29 (6.38)	49.84 (8.39)
12 h	85.21 (10.81)	66.95 (3.07)	27.33 (2.22)	43.56 (5.72)	60.65 (6.61)	59.65 (6.72)	65.17 (8.64)	30.64 (4.65)
16 h	68.27 (8.60)	61.53 (3.54)	31.37 (2.70)	56.06 (6.72)	70.56 (8.74)	70.32 (11.43)	64.02 (9.64)	35.41 (5.84)
21 h	96.93 (18.08)	70.37 (2.94)	31.12 (2.44)	29.32 (3.79)	69.83 (7.89)	63.43 (6.78)	61.31 (8.03)	36.84 (7.11)
26 h	72.64 (8.01)	73.56 (3.76)	36.25 (3.60)	40.85 (5.54)	69.91 (8.54)	67.88 (8.19)	61.95 (8.85)	28.78 (3.91)
40 h	103.00 (13.94)	78.36 (2.33)	31.12 (2.24)	47.72 (7.21)	64.31 (7.34)	68.58 (6.90)	60.89 (9.12)	32.96 (5.77)
61 h	79.06 (9.38)	86.77 (2.33)	32.28 (2.42)	38.28 (4.14)	75.08 (8.77)	69.06 (6.37)	66.05 (6.94)	33.23 (4.56)

Since the three parameters had similar trend over time on different scales, this trend was only displayed in **Figures 4.15-1~5** where mean kinetic energy values were plotted as a function of setting time.

DOI:10.14753/SE.2014.1974

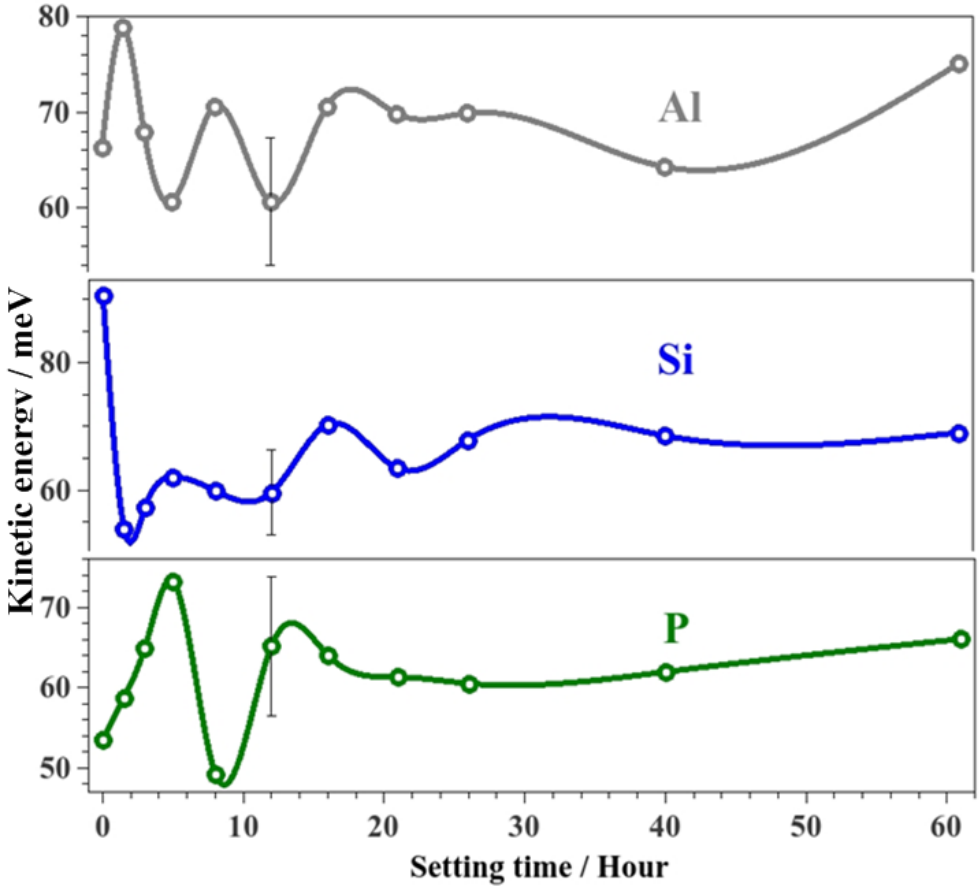

Figure 4.15-1 Calculated mean kinetic energy values (circles) and spline showing trend as a function of setting time for Al (grey), Si (dark blue) and P (green), with representative error bars at 12 h.

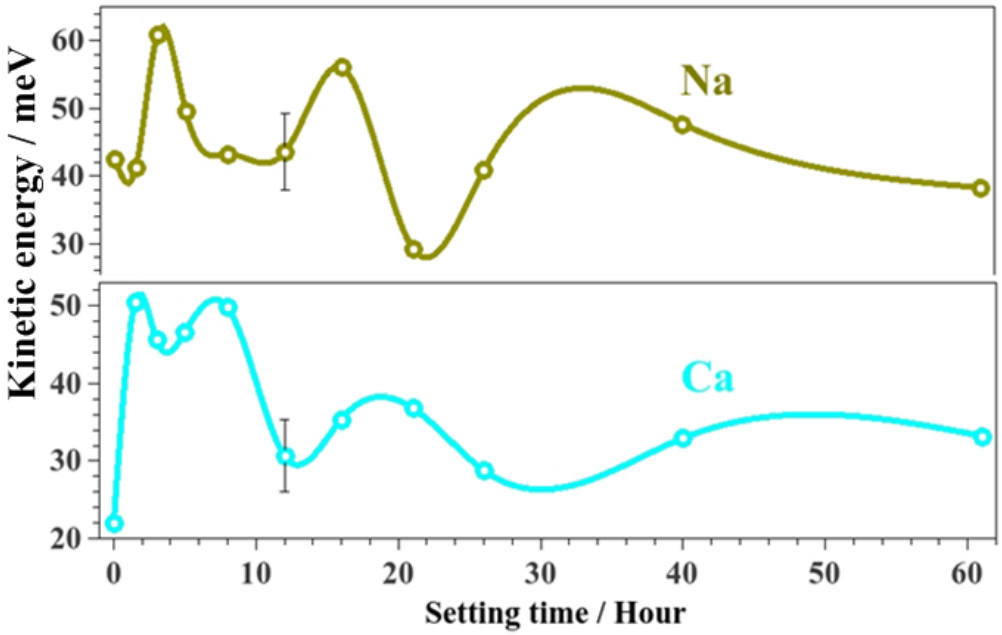

Figure 4.15-2 Calculated mean kinetic energy values (circles) and spline showing trend as a function of setting time for Na (yellow) and Ca (light blue) with representative error bars at 12 h.

DOI:10.14753/SE.2014.1974

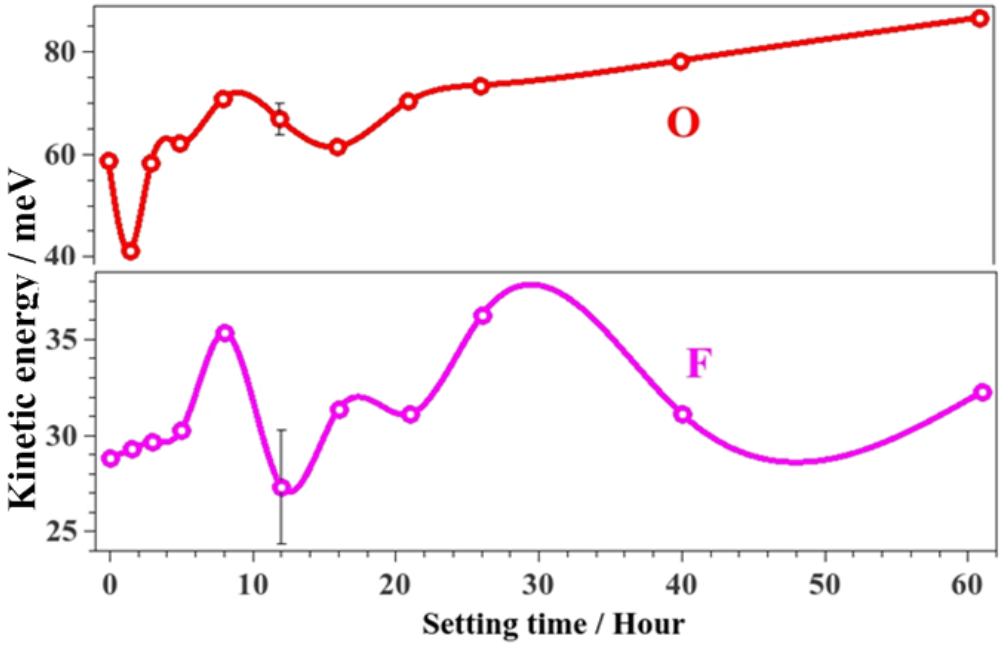

Figure 4.15-3 Calculated mean kinetic energy values (circles) and spline showing trend as a function of setting time for O (red) and F (magenta), with representative error bars at 12 h.

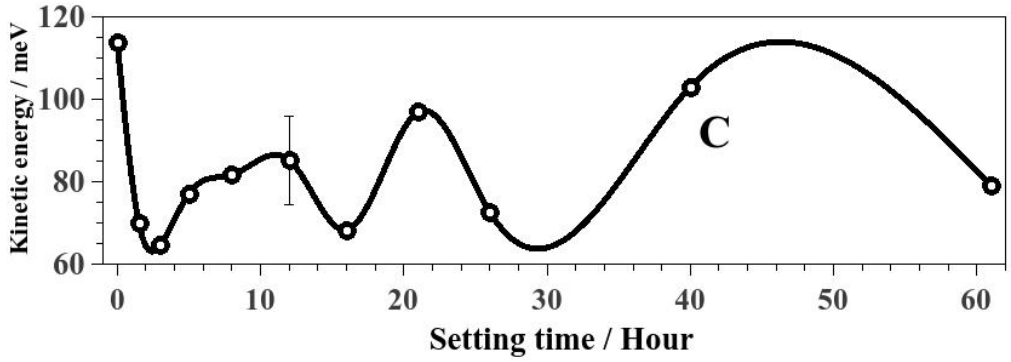

Figure 4.15-4 Calculated mean kinetic energy values (circles) and spline showing trend as a function of setting time for C, with representative error bar at 12 h.

The KE values of C and Al were co-plotted in **Figure 4.15-5**.

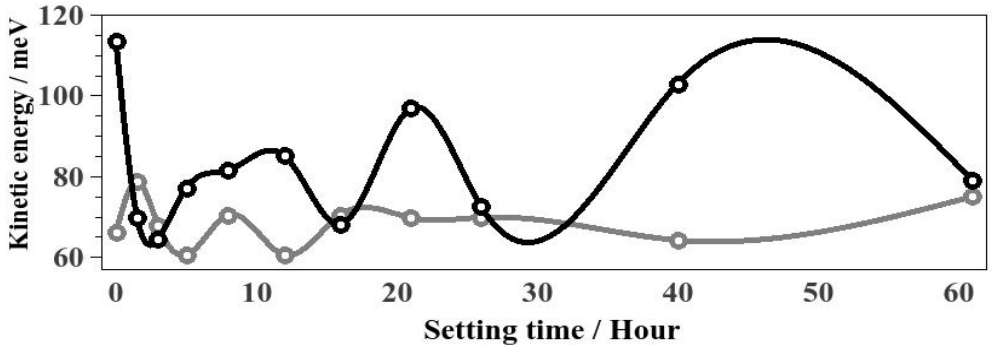

Figure 4.15-5 Calculated kinetic energy values (circles) and spline showing trend as a function of setting time for Al (grey) and C (black).

Table 12. Calculated harmonic oscillator frequency in cm^{-1} for the heavy atoms with standard deviation in bracket.

Time	C	O	F	Na	Al	Si	P	Ca
0 h	1222.58 (185.67)	633.48 (62.00)	261.27 (12.18)	458.11 (37.38)	493.72 (38.63)	972.99 (91.97)	575.11 (95.50)	236.91 (31.66)
1.5 h	752.25 (111.83)	441.85 (61.28)	314.94 (28.75)	443.57 (61.31)	497.24 (54.97)	580.10 (76.25)	631.62 (71.91)	543.79 (64.19)
3 h	694.87 (98.73)	628.33 (54.55)	318.96 (31.63)	655.28 (127.99)	712.48 (96.18)	616.53 (97.10)	698.54 (109.15)	491.23 (84.03)
5 h	829.56 (111.97)	670.17 (54.21)	325.73 (32.64)	534.34 (78.37)	848.32 (139.01)	667.64 (96.24)	787.75 (111.77)	501.64 (72.12)
8 h	878.04 (106.77)	762.43 (40.81)	380.19 (31.59)	464.73 (85.64)	731.16 (101.70)	644.59 (72.50)	530.05 (68.59)	535.94 (90.18)
12 h	916.38 (116.25)	719.96 (33.05)	293.90 (23.90)	468.43 (61.52)	652.22 (71.03)	641.44 (72.32)	700.88 (92.93)	329.48 (49.96)
16 h	734.15 (92.49)	661.69 (38.02)	337.39 (29.07)	602.90 (72.31)	758.76 (94.03)	756.21 (122.91)	688.44 (103.71)	380.83 (62.84)
21 h	1042.43 (194.40)	756.77 (31.63)	334.63 (26.19)	315.29 (40.74)	750.95 (84.88)	682.16 (72.96)	659.34 (86.35)	396.19 (76.50)
26 h	781.13 (86.13)	791.04 (40.42)	389.80 (38.68)	439.25 (59.57)	751.81 (91.86)	885.96 (92.38)	666.18 (95.17)	309.52 (42.03)
40 h	1107.72 (149.90)	842.66 (25.03)	334.63 (24.12)	513.18 (77.58)	691.54 (78.96)	737.55 (74.18)	654.81 (98.13)	354.45 (62.09)
61 h	850.17 (100.91)	933.17 (25.09)	347.15 (25.97)	411.70 (44.47)	807.40 (94.30)	742.62 (68.51)	710.28 (74.68)	357.39 (49.09)

4.2.1.3 Qualitative GIC NCS width

Since the composition of GIC contains H (forward scattering) and heavy atoms (back scattering) the NCS results of these must be combined to reflect the overall GIC atomic potential and cohesion to help elucidate the setting dynamics from the aspect of internal atomic cohesion. This was done by weighting H and each heavy atom NCS width values (**Tables 9-10**) with stoichiometry to obtain the GIC NCS width. The same was done for glass and polymer. GIC t=0 value was obtained by stoichiometrically weighting glass and polymer values (**Figure 4.16**). The values obtained for all three temperatures were co-plotted in **Figure 4.17**.

DOI:10.14753/SE.2014.1974

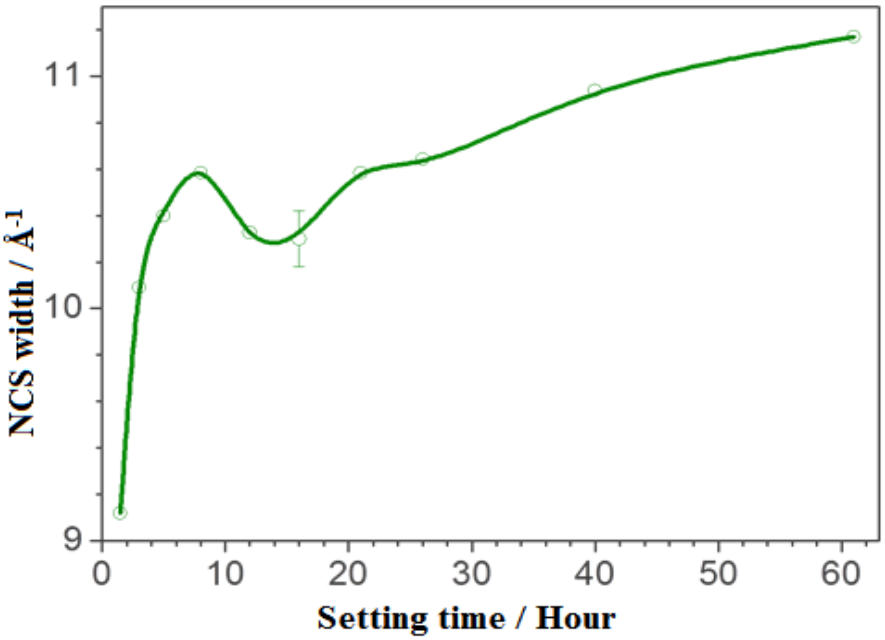

Figure 4.16 GIC NCS width value derived by weighting elemental NCS width value as a function of setting time at 300K.

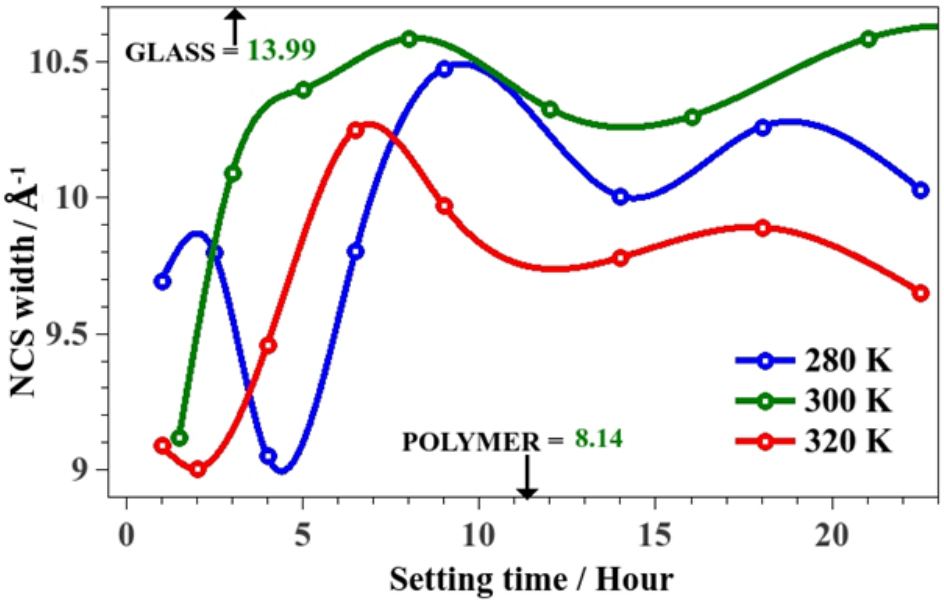

Figure 4.17 GIC NCS width value derived by weighting elemental NCS width value as a function of setting time at 280 K (blue), 300 K (green) and 320 K (red). Glass and polymer values are also marked.

DOI:10.14753/SE.2014.1974

4.2.1.4 Conversion of NCS values to engineering units

The calculated NCS peak width values of GIC and its components were plotted against their respective literature fracture toughness values and those of related materials in **Figure 4.18**.

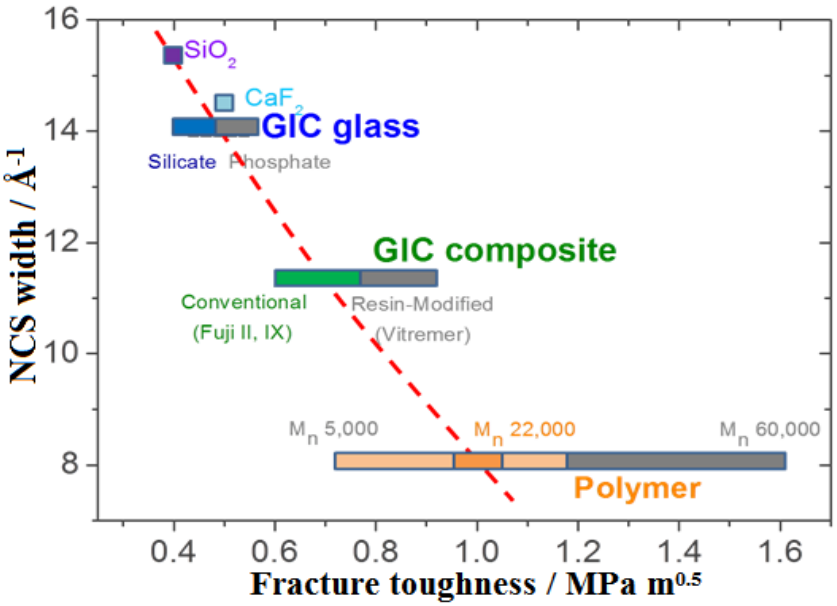

Figure 4.18 Calibrated NCS peak widths versus fracture toughness for GIC, its components and related materials. The inverse relation is represented by a fit curve (red broken line).

Using the dashed curve in **Figure 4.18** as a look-up-table for calibrating NCS widths in $Å^{-1}$ with fracture toughness in MPa $m^{0.5}$, the calibrated intrinsic fracture toughness of GIC at different temperatures as well as elemental fracture toughness were plotted in **Figures 4.19-21**.

DOI:10.14753/SE.2014.1974

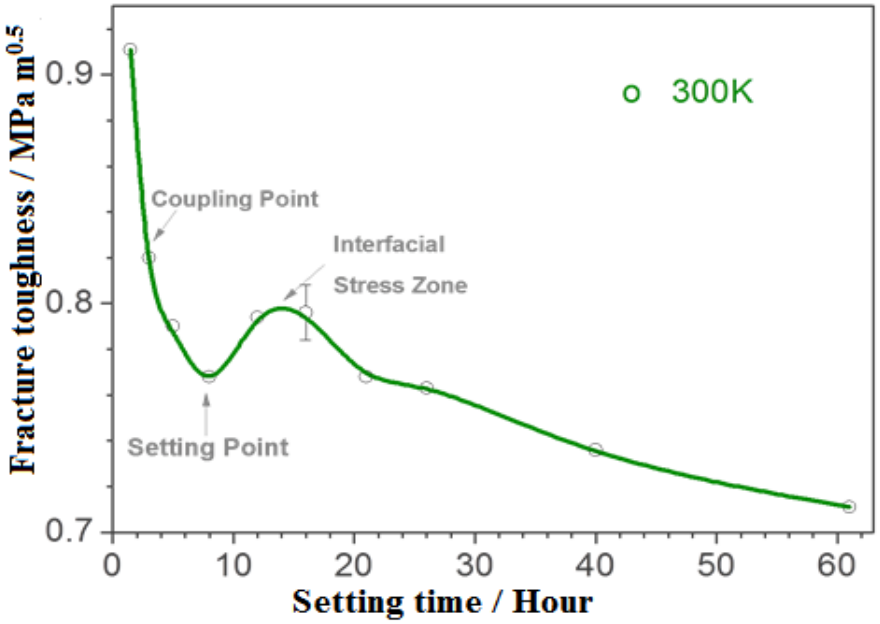

Figure 4.19 Calibrated fracture toughness of GIC at 300 K as a function of setting time with representative error bar. The assigned coupling point, setting point and interfacial stress zone are also marked.

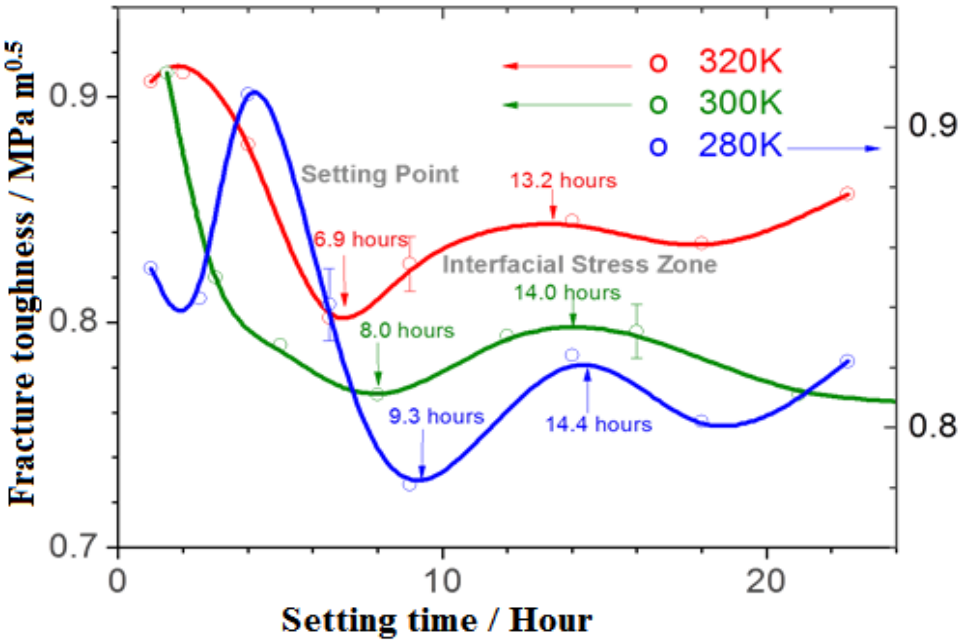

Figure 4.20 Calibrated fracture toughness of GIC at 280 K (red), 300 K (green) and 320 K (red) as a function of setting time. The assigned coupling point, setting point and interfacial stress zone are also marked.

DOI:10.14753/SE.2014.1974

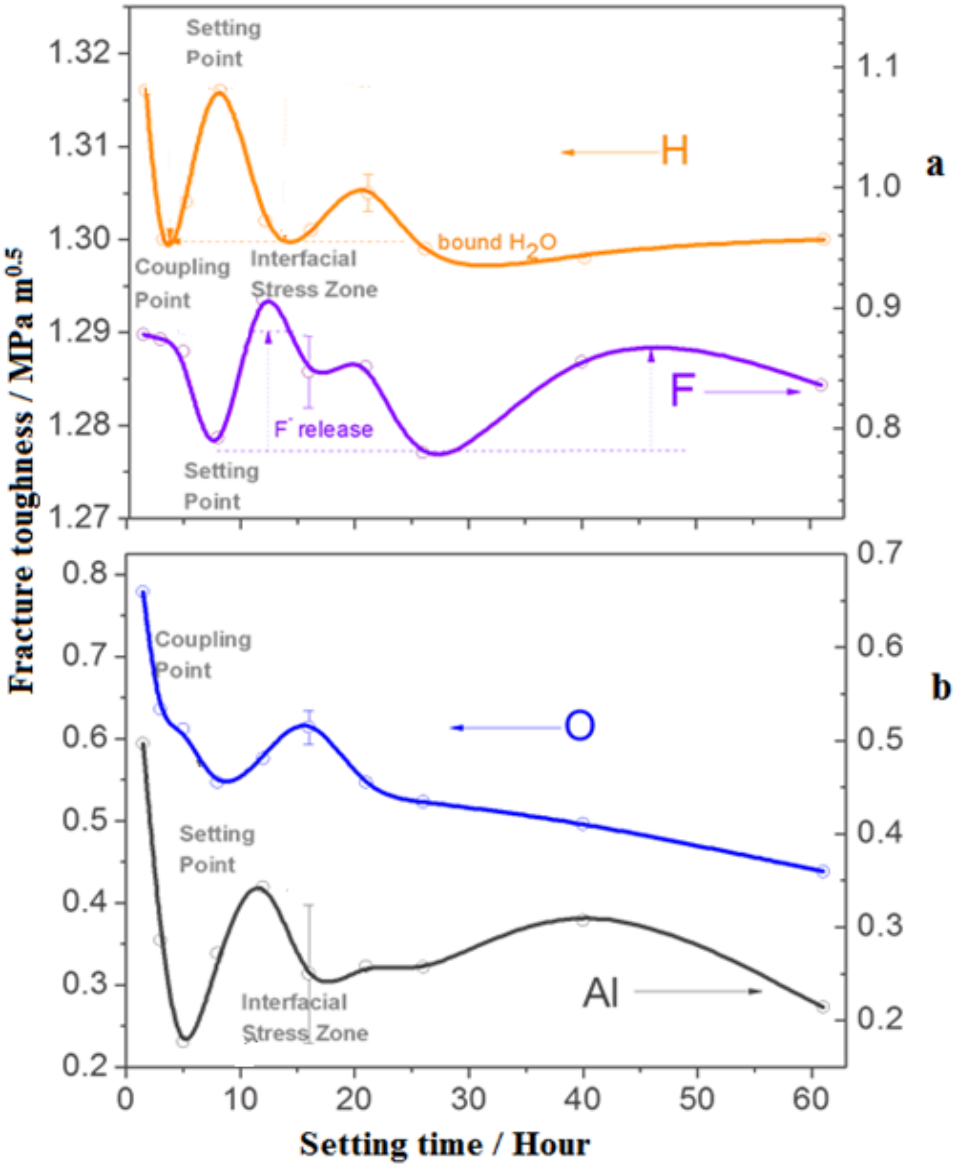

Figure 4.21 Calibrated elemental fracture toughness for (a) H and F; (b) O and Al as a function of setting time. The assigned coupling point, setting point and interfacial stress zone are also marked.

4.2.2 Neutron diffraction experiments

The measured experimental Total Structure Factor $F(Q)$ as a function of Q was shown in **Figure 4.22**.

DOI:10.14753/SE.2014.1974

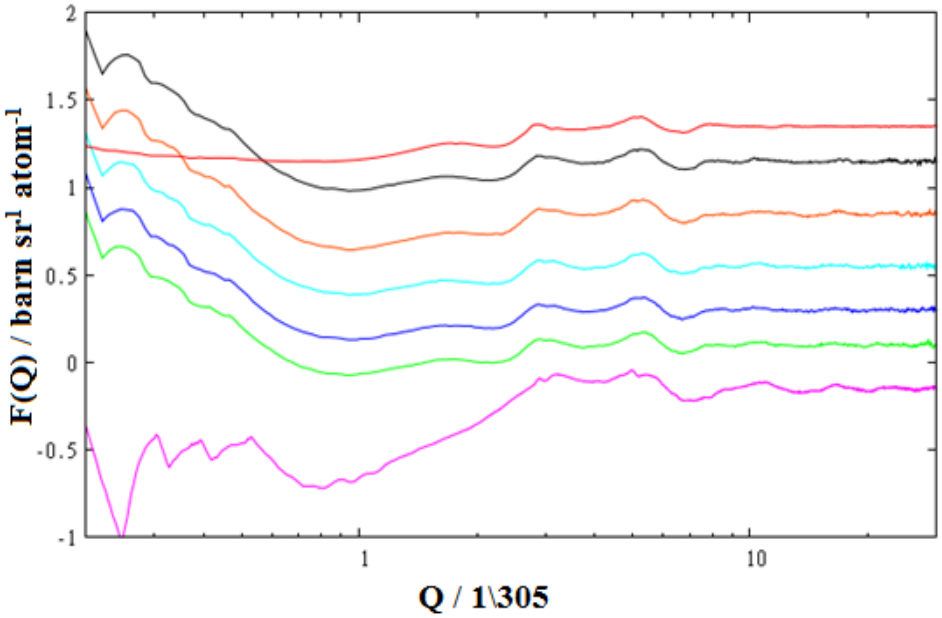

Figure 4.22 Differential cross sections as a function of *Q* on log scale of (bottom) polymer solution (magenta), (top) G338 glass (red) and (middle) GIC from bottom up at 0.5 h, 1.5 h, 4 h, 8 h, 14 h, 24 h, all offset vertically for clarity.

The structure factor *S*(*Q*) (**Figure 4.23**) was derived from *F(Q)* as the normalised form.

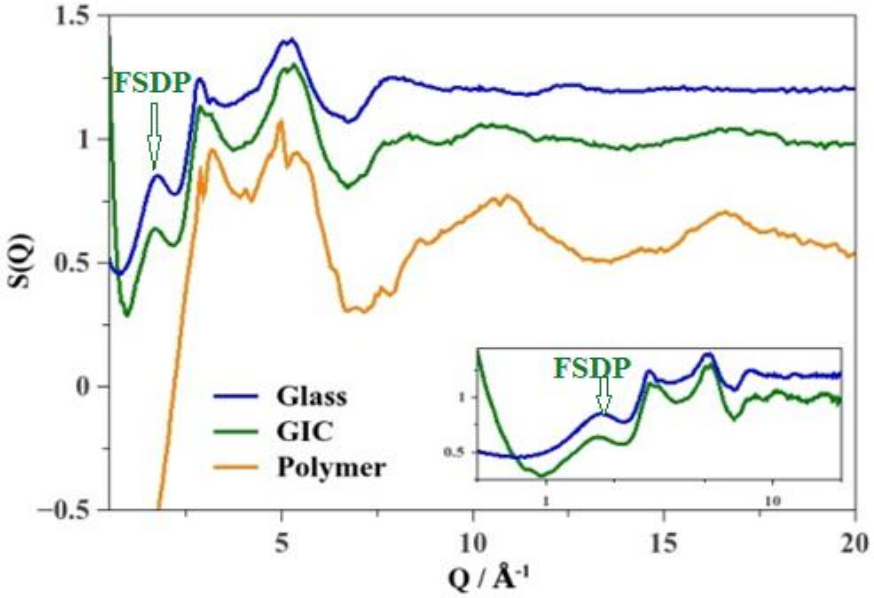

Figure 4.23 *S*(*Q*) of glass (blue), GIC average over 24 hours (green) and polymer solution (orange). Inset: *S*(*Q*) of glass (blue), GIC 24 h average (green) on log scale. Both with FSDP marked.

Figure 4.24-1 focuses on the near and intermediate range of *Q*=0.5-2 $Å^{-1}$ in **Figure 4.23** and is on the log scale for *Q*.

DOI:10.14753/SE.2014.1974

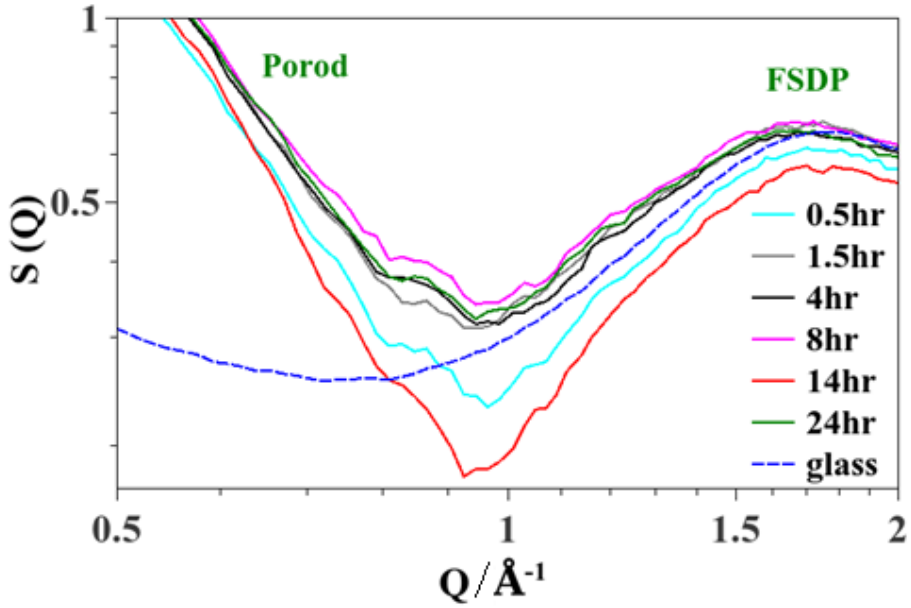

Figure 4.24-1 *S*(*Q*) of the GIC time series and glass (blue dashed line) in the range *Q*=0.5-2 Å^{-1} on log scale. Porod range and FSDP are marked.

The trend in **Figure 4.24-1** was presented with two parameters: Integrated small angle neutron scattering (SANS) peak area in the range Q=0.5-0.95 Å^{-1} (**Figure 4.24-2a**) and First sharp diffraction peak position Q_{FSDP} (**Figure 4.24-2b**).

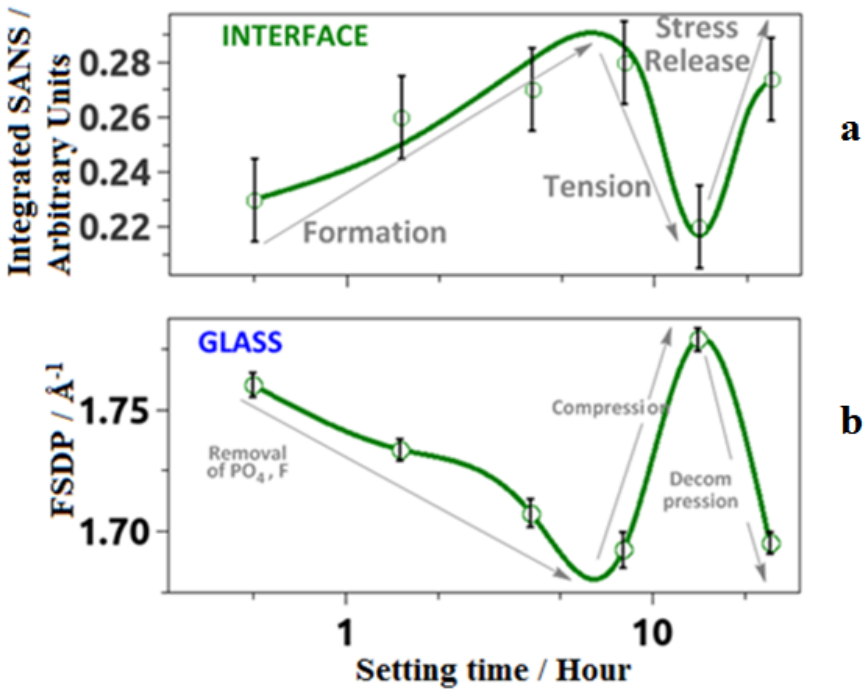

Figure 4.24-2 (a) Integrated peak area under the *S*(*Q*) curves in **Figure 4.24-1** in the range Q=0.5-0.95 Å^{-1}; (b) First sharp diffraction peak position Q_{FSDP} plotted with error bars as a function of setting time on *log* scale. The probable atomic events are marked.

DOI:10.14753/SE.2014.1974

Figure 4.25 is the total pair distribution functions *g*(*r*) for glass, GIC average and polymer.

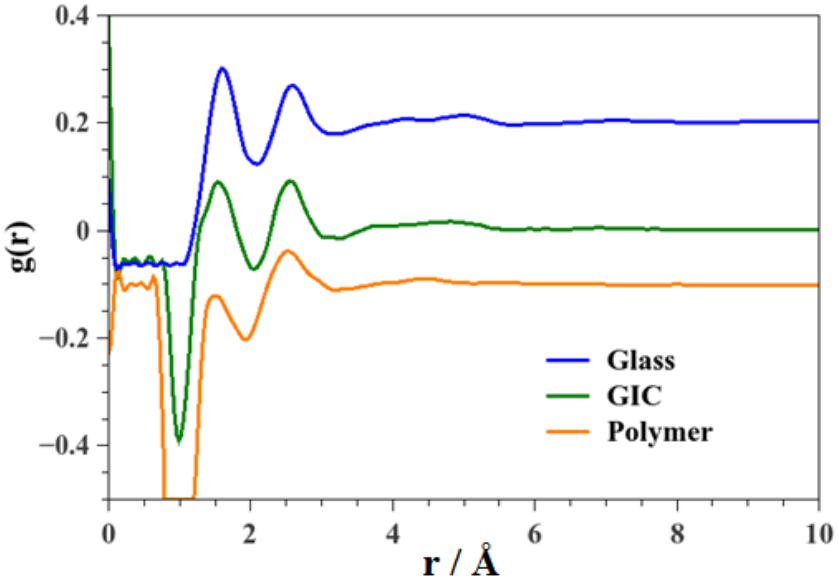

Figure 4.25 Total pair distribution functions as a function of inter-atomic distance *r* of glass (blue), GIC 24 h average (green) and polymer solution (orange), all offset vertically for clarity.

The total pair distribution functions *g*(*r*) of the cement at different setting times in the range 1 ~ 2 Å were plotted in **Figure 4.26**.

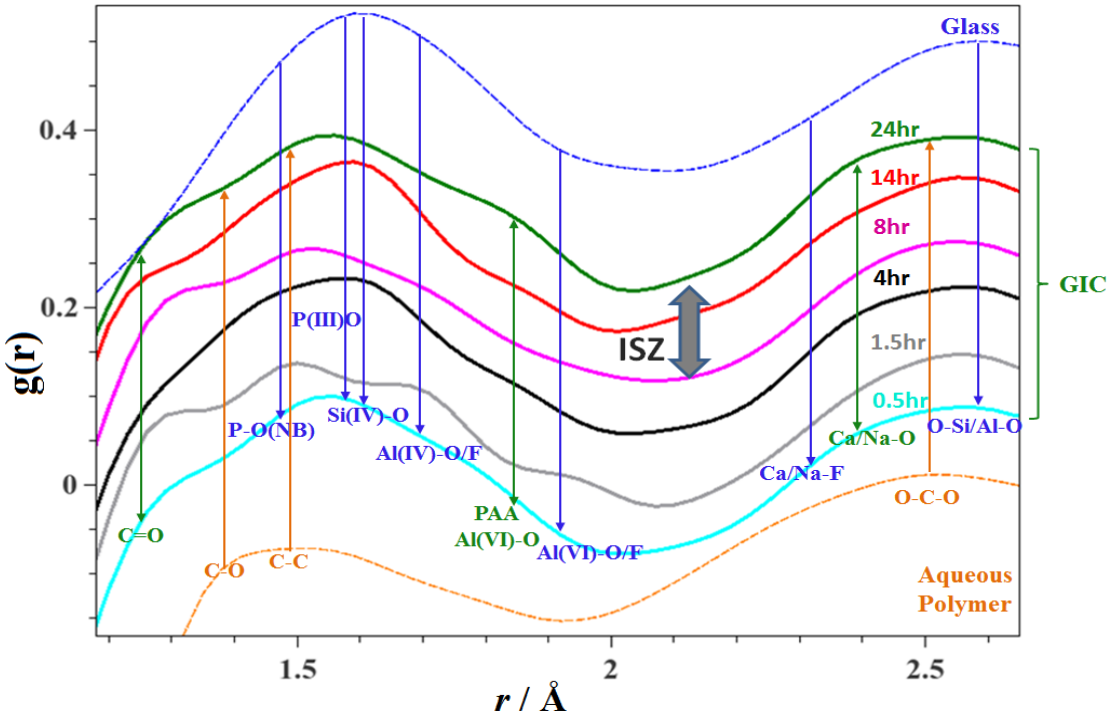

Figure 4.26 Total pair distribution functions as a function of inter-atomic distance *r* in the range 1.5-2.6 Å of (bottom) polymer solution (orange), (top) G338 glass (blue) and (middle) GIC from bottom up at 0.5h, 1.5h, 4h, 8h, 14h, 24h, all offset vertically for clarity. The possible atomic bonds are assigned.

DOI:10.14753/SE.2014.1974

By differentiating $g(r)$ between chosen time points we obtained $\Delta g(r)$ in **Figure 4.27**.

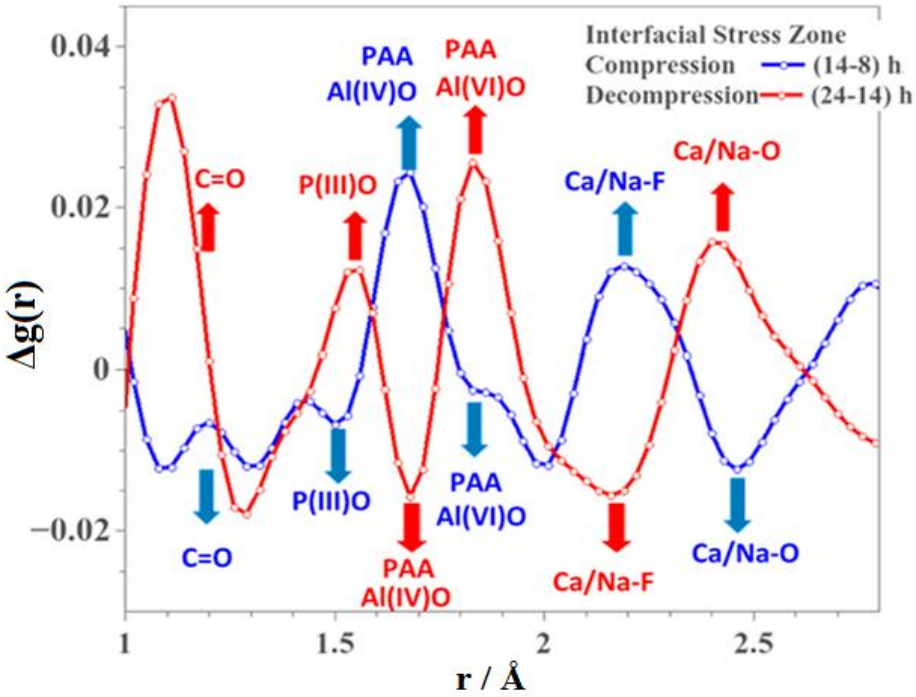

Figure 4.27 Difference of total pair distribution function, $\Delta g(r)$, between 14 h and 8 h, 24 h and 14 h cements as a function of inter-atomic distance r with the major atomic bonds change marked with arrows.

4.3 Complementary experiments

4.3.1 Differential Scanning Calorimetry (DSC)

The DSC results of the two glass upscans and one upscane of 60-h cement were shown in **Figure 4.28**.

DOI:10.14753/SE.2014.1974

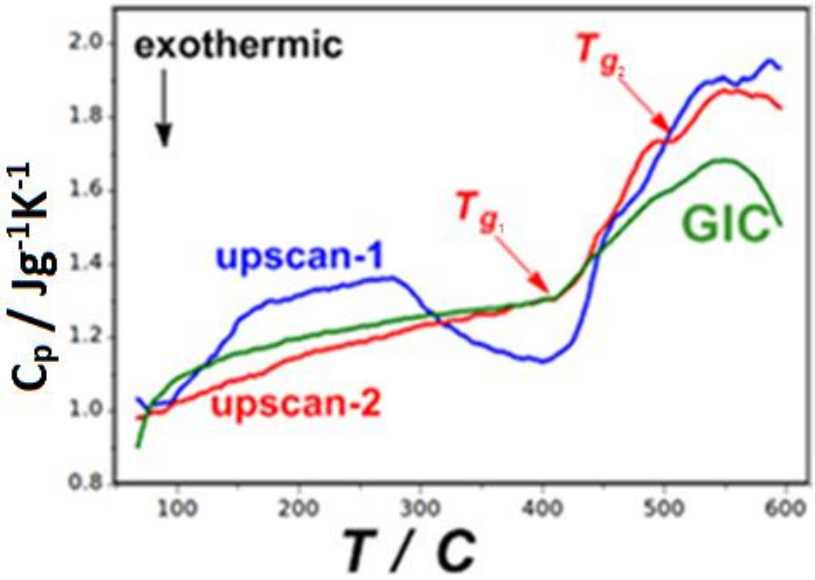

Figure 4.28 DSC output for 2 upscans of the glass (blue and red) and one scan of GIC cement (green) after 60 h of setting, where the second T_g almost disappears.

Figure 4.28 was only the first part of the heat response of G338 glass up to 600 °C, the whole DSC output up to 1200 °C co-plotted with the mass change as well as analysis marking the features present were shown in **Figure 4.29**.

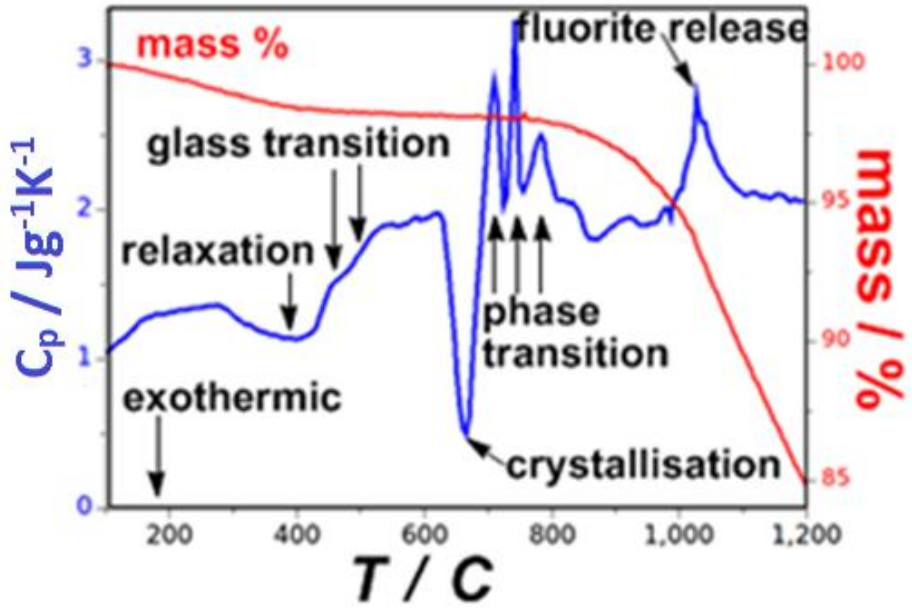

Figure 4.29 DSC output of glass up to 1200°C (blue) with profile-features highlighted; mass-% change as a function of temperature (red) is co-plotted.

DOI:10.14753/SE.2014.1974

4.3.2 Transmission Electron Microscopy (TEM)

TEM image of G338 powder was presented in **Figure 4.30**.

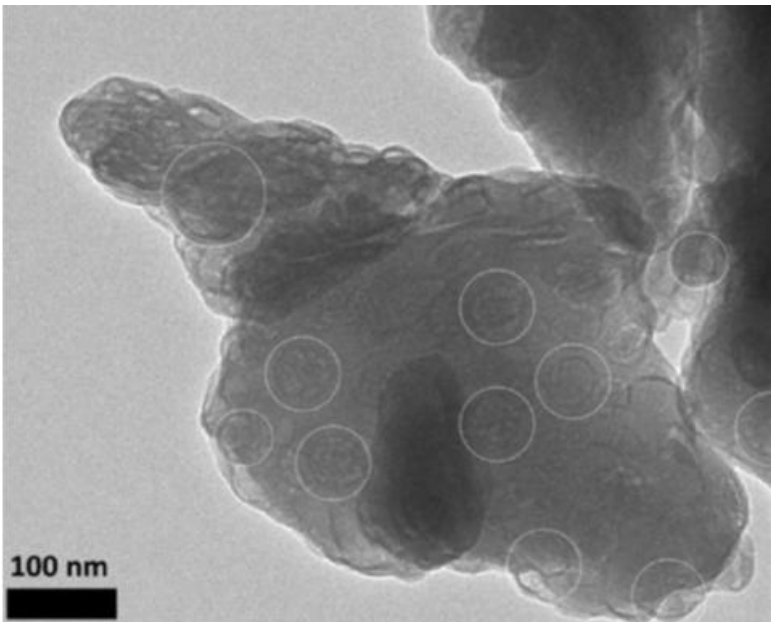

Figure 4.30 TEM image of a single particle, revealing complex phase separation of 50 nm globules within the matrix.

4.3.3 Coherent Terahertz Spectroscopy (CTS)

Insertion loss in CTS is usually measured in decibel (dB) units and is equivalent to intensity in other spectroscopy techniques.

Dispertive intensities at times of interest were presented in **Figure 4.31**.

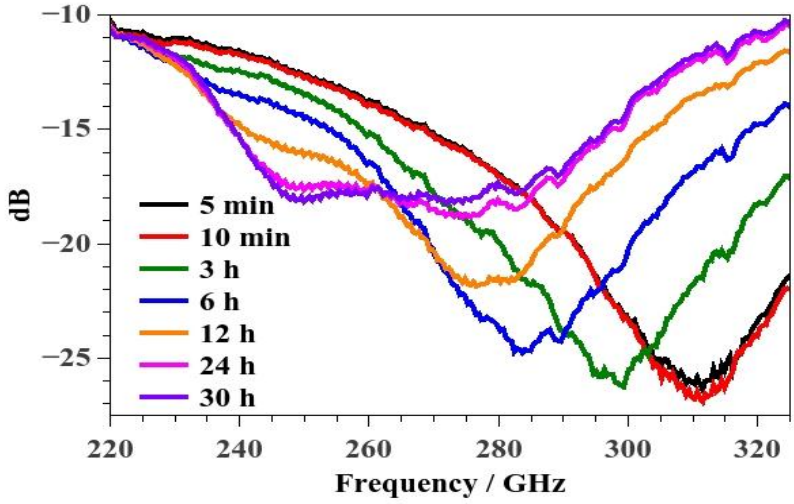

Figure 4.31 The measured insertion loss (dB) of GIC at selected setting times plotted as a function of frequency.

Recasting of these plots in **Figure 4.31** by subtracting from them the spectral response of the 5-minute trace helped elucidate the activity within this test setup **(Figure 4.32)**.

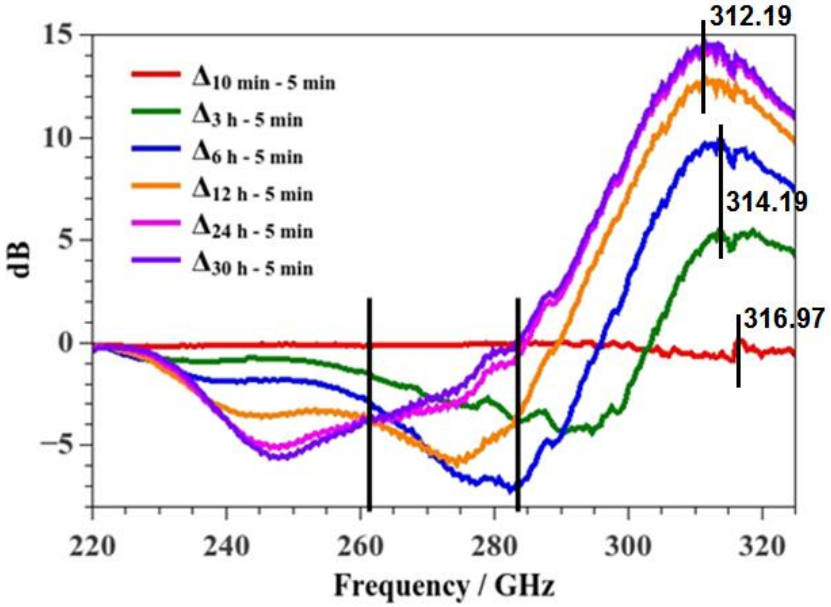

Figure 4.32 Differences in insertion loss (dB) of 3 h, 6 h, 12h, 24 h and 30 h GIC with respect to that of 5 min trace of spectral response. The two black lines are added to qualitatively subdivide the frequency domain into three for natural interpretation. The peak-centers are marked with short vertical lines and their frequency values marked.

The plots of intensity *vs.* setting time at selected frequencies at 20 GHz intervals in the spectral domain 220-320 GHz, as a function of setting time were shown in **Figure 4.33**.

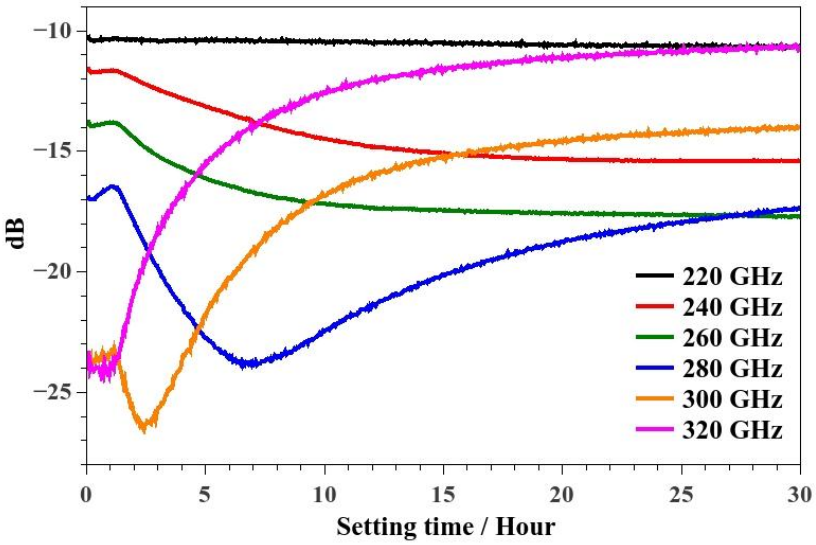

Figure 4.33 The measured insertion loss (dB) of selected frequencies as a function of setting time.

DOI:10.14753/SE.2014.1974

The time-dependent features as the sum of all of the 2001 frequency points from 220 to 325 GHz collected over the course of the experiment as a function of setting time was plotted in **Figure 4.34**. Those of the glass and polymer were horizontal lines because isolated from each other their response was unreactive and invariant. Since their dB values were outside the absolute value range of GIC their plots were not shown but only their values were marked.

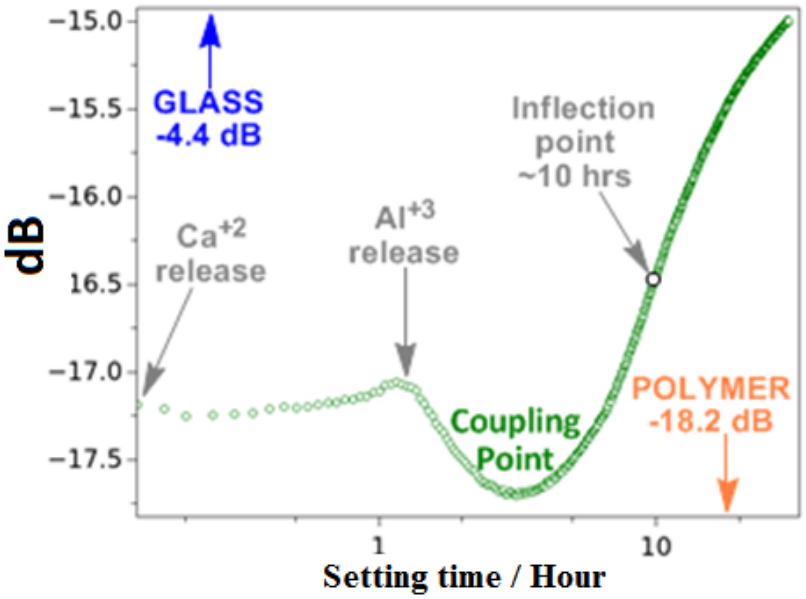

Figure 4.34 The green trace of GIC shows absorption response as the sum of all 2001 frequency points from 220-325 GHz with a resolution of 52.5 MHz. The constant dB *vs.* time plots of glass and polymer are outside the absolute value range of GIC and only the values are marked.

The frequency-dependent THz absorption coefficient α of the GIC were evaluated as a function of setting time (**Figure 4.35**). The inflection point was also ~10 hours.

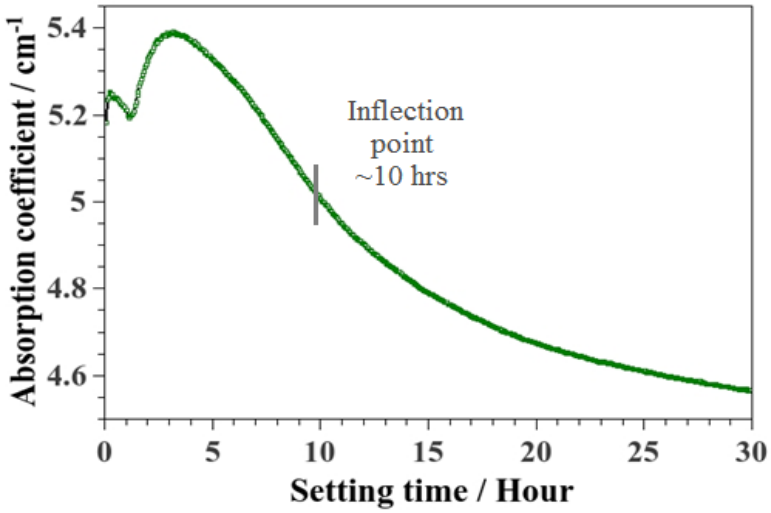

Figure 4.35 The absorption coefficient α of GIC as a function of setting time with the inflection point at 10 hours marked.

DOI:10.14753/SE.2014.1974

4.3.4 Computational Modeling

Preliminary Al-coordination permutation models (**Figure 3.5**) were constructed to characterise the influence of axial and equatorial ligands on ^{27}Al-NMR shifts relative to the experimental standard ($AlCl_3$•$6H_2O$).

NMR predictions for ^{27}Al-chemical shifts (relative to $AlCl_3$•$6H_2O$ set to 0 ppm) for multiple Al-polymer models were shown in **Figure 4.36**.

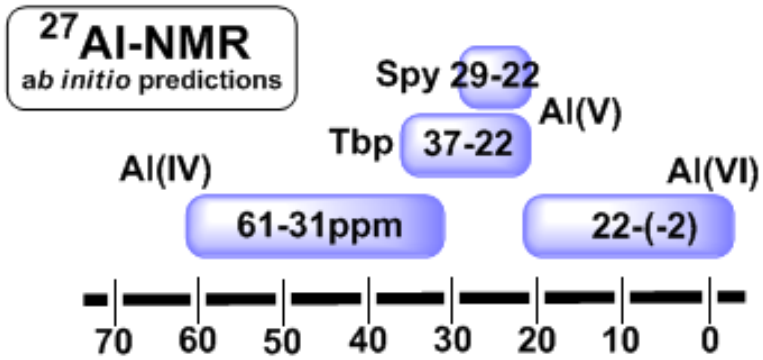

Figure 4.36 Shifts remain in the ~60-0 ppm experimentally-determined bounds; theory predicts shifts for Al(IV) and Al(VI) to extend further up- and down-field, respectively, than the experimental assignments.

The hydrated 8-unit molecular cluster ($Ca_8Al_{16}Si_{16}O_{64}H_{40}$, 164 atoms) was shown in **Figure 4.37**.

DOI:10.14753/SE.2014.1974

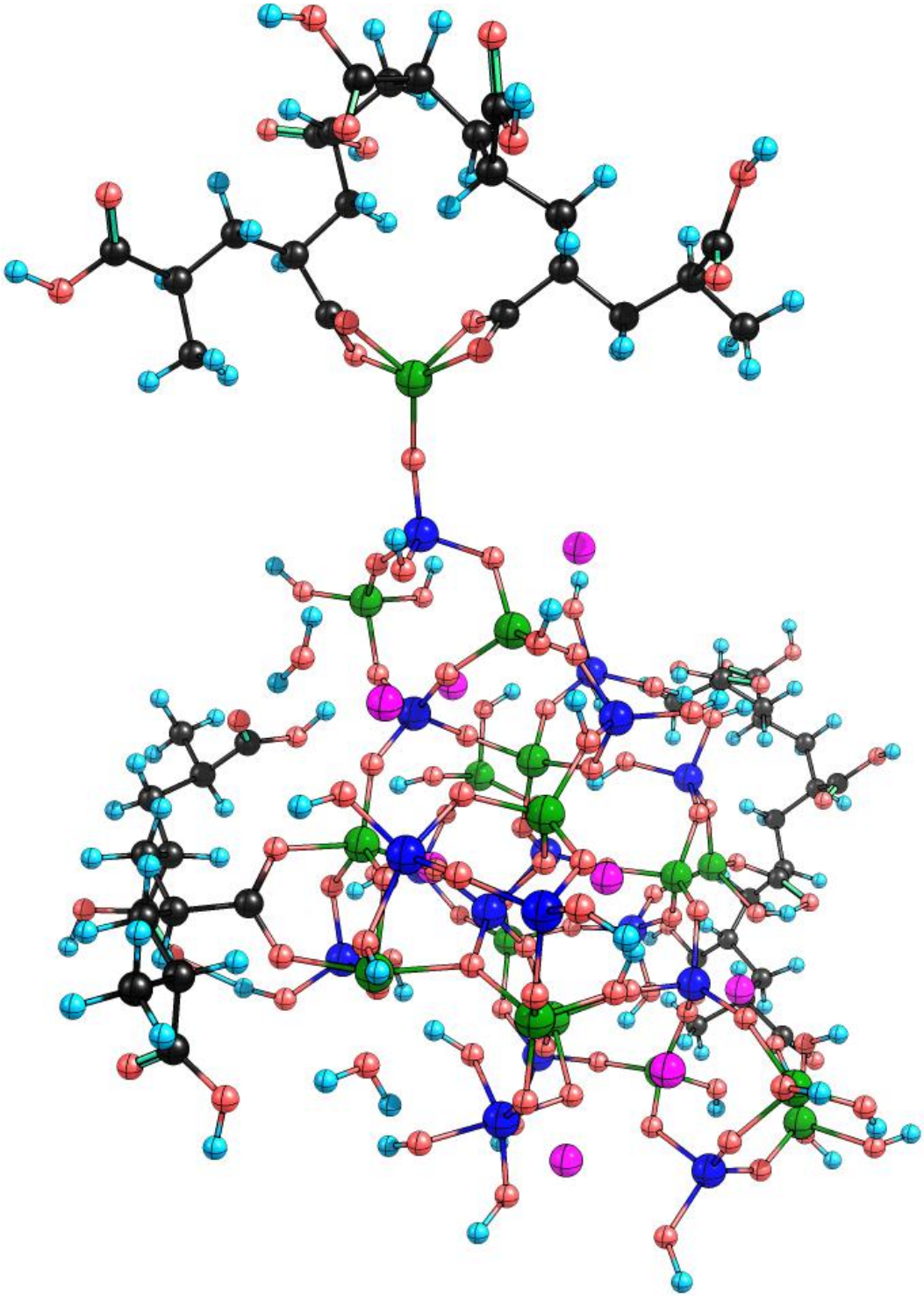

Figure 4.37 Collective organic-inorganic vibrations of a PAA strand attached to an alumina-silicate glass cluster pivoted by Al(V), including water and solvent correction.

DOI:10.14753/SE.2014.1974

The 78-atom, 396-electron, top-slice of the model polymer-glass linkages computed for the commercial GIC used in these experiments were illustrated in **Figure 4.38**, and were characterised by differing degrees of aluminium coordination.

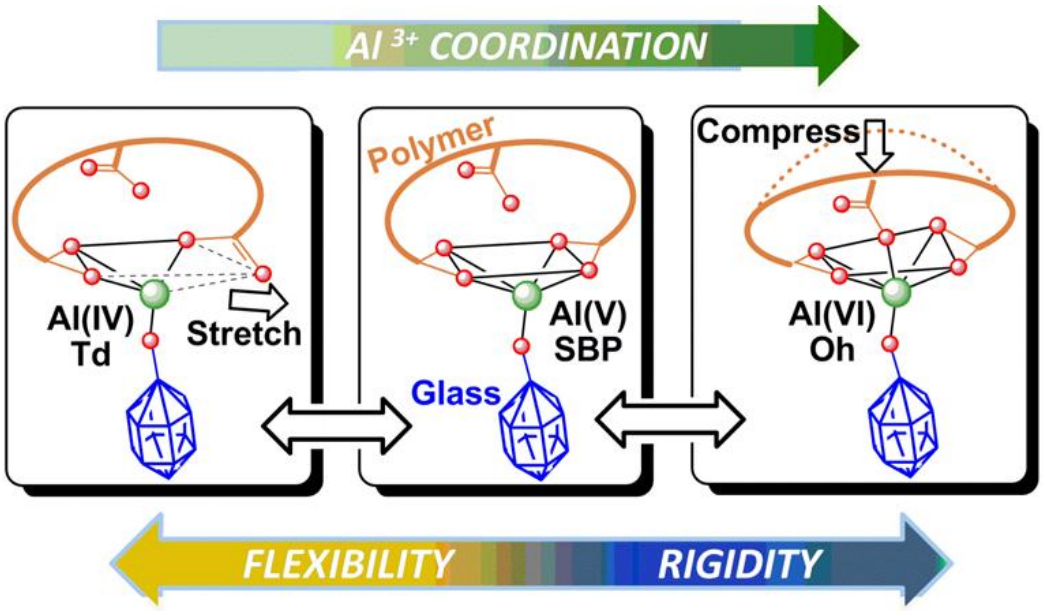

Figure 4.38 Cartoons of the Al-coordination changes as a result of stretching one equatorial Al-O bond to generate the tetrahedral Al (left). The influence of compression of the polymer chain towards the Al centre, results in a new axial Al-O bond being formed with an additional carboxylate group (right). Concurrent distortion of one Al-O bond in each of the equatorial carboxylate groups generates a distorted and strained Oh structure.

Difference in the relative contributions to Gibbs free-energy for V- vs. IV-coordinate and V- vs. VI-coordinate Al structures calculated from model in **Figure 4.37** was plotted in **Figure 4.39** together with the grouped vibrational modes.

DOI:10.14753/SE.2014.1974

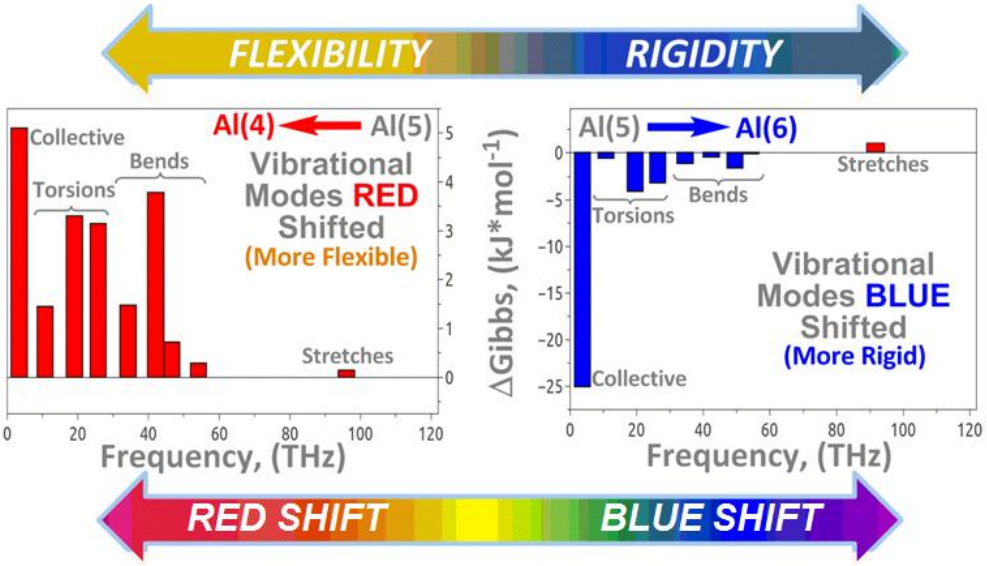

Figure 4.39 Difference in the relative contributions to Gibbs free-energy as a function of frequency for the V- vs. IV-coordinate (left) and V- vs. VI-coordinate Al structures. Vibrational modes have been grouped to address statistical dispersion.

Selected collective vibrational modes calculated for this Al(V) model (**Figure 4.37**) were plotted in **Figure 4.40** together with other experimental and theoretical results.

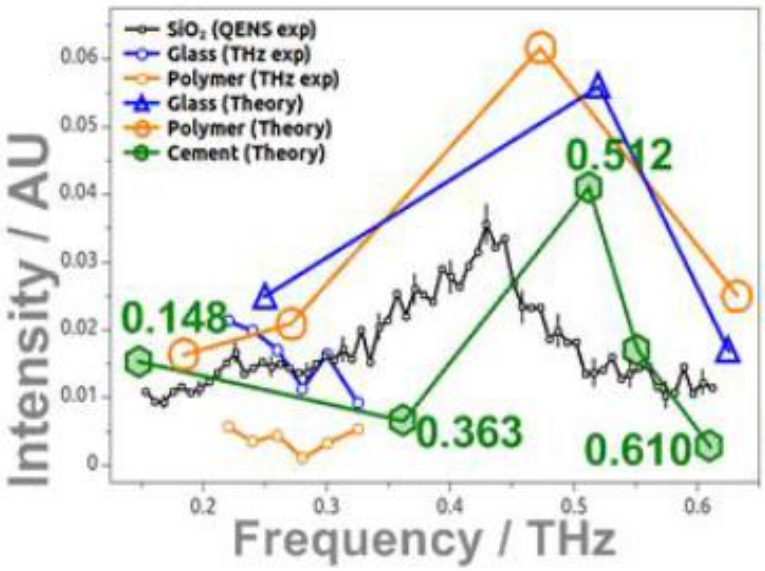

Figure 4.40 Relative intensity of THz 2-level modes for SiO_2 glass [318] and collective vibrations measured for glass and polymer components of GIC, compared to quantum chemical models of polymer, glass and GIC of the theory section.

DOI:10.14753/SE.2014.1974

5 DISCUSSION

5.1 Mechanical testing and fractography

5.1.1 Hertzian indentation test

The ratio of the failure load (**Figure 4.1**) approaches that of the geometrical dimensions, implying near-linear behaviour in failure load. The scale of scatter in failure load for normal size samples was relatively high, yet is typical of the variability expected in practical and clinical applications. It is expected that flaws other than those inherent in the material would influence the strength of the samples. Determination of the fracture origin was therefore carried out in order to rationally characterise the observed failure behaviour and variability.

The failure behaviour of GIC is controlled by its composition as well as setting mechanism and kinetics. Conventional GIC setting occurs by an acid-base reaction. During setting, the outer layer of the glass is attacked by the acid, with unreacted glass cores bonding the carboxylic groups (COO-) of the polyacid chains through ionic salt bridges with aluminium and calcium cations leached from the glass. The unreacted glass cores act as fillers within the resultant composite glass-polymer matrix [4].

Characterisation of Fuji IX is limited in the literature, with no Hertzian indentation tests reported to date. The values obtained in this study were in the range of those reported on other types of conventional GICs, in tests using the same sample geometry [165]. It is known that indentation size plays an important role in the failure mode of Hertzian indentation tests, hence can be controlled by choice of indenter size and sample thickness [284].

The present study used the same test geometry (2 mm thick × 10 mm diameter), and the samples were tested with a 20 mm diameter spherical indenter in a coating-substrate bi-layer structure, in order to reproduce bottom-surface initiated radial fracture which is the relevant clinical failure mode. During the indentation test, compression is generated on the top surface of the sample while tension builds at the bottom surface. For GIC samples of smaller thickness (2 mm), the intensity of the bottom tensile field for radial cracking is stronger than that of the top compressive field for cone cracking, hence, radial cracking occurs first [165]. Due to instrumental limitation for initial crack detection, the test termination was slightly delayed (<1 s) after maximum load was reached (sample failure), extra compression work may have been applied to the

samples. However, this does not affect failure load determination or principal crack recognition. More efficient means of crack detection, such as acoustic monitoring [165], will be applied in future work towards more effectively arresting the test once failure has occurred.

5.1.2 µCT imaging

As previously noted, fracture processes cannot be treated as 2-D phenomena, but instead as 3-D systems of branching cracks [285]; µCT imaging in 3-D facilitates imaging of such material failure. The size of the smaller samples used in this study (0.2 x1.0mm) was critical to the µCT resolution. Due to projection geometry of cone beam CTs, resolution varies inversely with sample diameter. Hence, the miniature sample size provides a compromise between optimal resolution and characteristic sample dimension and preparation. It is seen from **Figure 4.2** that the main crack propagated preferentially along the weak points of the material, specifically along the pores and the glass-matrix interfaces, implying filler-matrix binding does not possess material toughness.

The tendency of microcracks to propagate through the pores in the vicinity of the crack path was observed from **Figure 4.3** while the crack propagating from the origin was deflected at a point of low porosity, changing direction to form a 'T-shaped' crack connecting the main cracks. This implied locally increased failure resistance by crack branching, as well as cracking being linked to sample inhomogeneity.

Partial radial cracking was also observed initiating from the sample's bottom surface. These were effectively arrested prior to reaching the top surface, and prevented from joining the main crack(s). These observations demonstrate the important contribution of the pore-crack interaction to the fracture process in GICs. The conclusion from these observations was that the mechanical properties of GIC could be improved through strengthening the glass-matrix bonding, eliminating (or at least reducing) porosity as well as increasing sample homogeneity.

The nanoCT image in **Figure 4.4** presents the spatial relationship between the microcracks and the glass cores, as well as the microcracks propagated along the edges and sides of the glass cores (glass core-matrix interface). The effective porosity determined by nanoCT (15.1±4.0%) was higher than that of µCT (11.6±0.1%), due to the inclusion of pores of thickness <4.4 µm that could not be resolved by µCT. As these

values were not of significant statistical difference at P=0.05, it is concluded that the method used in this study generates reliable results with respect to the high variability of material preparation in practical and clinical settings.

5.1.3 Complementary imaging

Conventional GICs are known to be brittle materials with high elastic modulus, and very low fracture toughness compared to composite resins [57]. The typical brittle fracture patterns such as hackles (lines on the surface running in the local direction of cracking, separating parallel, but noncoplanar portions of the crack surface) radiating out across the fracture surfaces from fracture origin, similar to those observed in glasses but in smaller scale [286], were observed in the optical (**Figure 4.5a**) and scanning electron micrographs (**Figure 4.5b**). As GICs are translucent, this presents pronounced difficulty for effective optical examination of their fracture surfaces. Through optimisation of illumination under optical microscope (transillumination) the fracture origin could be recognised. The SEM micrograph in **Figure 4.5b** clearly reveals these radial hackles and enables the pinpointing of crack origin responsible for material failure. Nearly all recognised fracture origins were surface-exposed pores, or surface dimples created during sample preparation. The crack almost always initiated from these differently-sized recesses. Failure initiation by flaws was therefore shown to be independent of size and to generate a relatively high scatter in failure load. SEM micrographs of the bottom surface of the samples also revealed extensive surface-exposed pores that may also act as fracture origins at differing loading conditions. This indicated that much effort should be put into increasing the surface quality of the restoration in practice, in order to obtain optimal material performance. This is in addition to the previously mentioned requirement for improving sample homogeneity.

No cone cracking nor plastic zone under the contact area was observed (to what extent had plastic deformation occurred was unknown), confirming previous observations [284]. The smaller samples were not similarly examined by SEM. It was concluded that for the smaller samples radial cracking is also the primary failure mode, as in the standard dimension samples. Hence, it is deduced that the size of plastic zone has no significant effect even in this case.

Scanning electron micrographs of the fracture surface (**Figure 4.6**) revealed extensive microcracks and porosity. The smaller and larger pores distributed intermittently throughout the material were approximately at 13 μm and 26~28 μm in diameter, respectively. The microcracks preferentially linked the pores, propagating through the matrix and along the glass-matrix interface. The cement did not have well integrated surface texture and the angular glass cores appeared loosely bound to the polyacid matrix. Also the exposed glass cores had a defined smooth surface indicating that weak bonding between the glass cores and polyacid matrix was broken during the test. If this bond was strong enough the cracks would not propagate along the glass-matrix interface but would instead proliferate through the matrix as well as the glass particles near or exposed to the surface in **Figure 4.6**. However, a polymer layer should limit visibility of the latter. Some microcracks also preferentially propagated through the pores and were deflected at the glass cores, a tendency of cracks to avoid glass cores. The stress intensity difference between the top and bottom surfaces of the samples determined the failure mode and the microstructure and porosity locally influenced crack propagation direction. These observations are in direct agreement with the μCT observation for the fracture procedure assessment.

The high vacuum used in SEM could have changed the surface morphology, as well as caused some of the microcracks in the samples. GICs are known to contain loosely bonded water in their structure [96] which would evaporate in vacuo. This explains the observation that translucent samples turn chalky after SEM examination. This problem is avoided in the μCT imaging used in this study, as it is carried out under conditions of ambient pressure and temperature, mimicking the conditions of real practical applications and clinical use of GICs.

5.2 Neutron experiments

5.2.1 Neutron Compton scattering (NCS) experiments

This work represents the 1st inelastic neutron scattering reported on dental composites. Although neutron diffraction has been employed to study structure in static systems, our

work pioneers the application of neutron scattering in the characterisation of cementation dynamics in a dental composite.

5.2.1.1 Forward scattering

It was seen that the large peak at the lower time of flight in **Figure 4.7a** was the sole contribution of the scattering signal from H. **Figure 4.7b** lacked such a peak because having similar mass as H atoms, neutrons are exclusively scattered forwardly by H atoms. The discontinued spectrum in the region 100-120 μsec was due to the removal of data contribution from second gold foil absorption at 60 eV.

The other feature in **Figure 4.7a** was the supposition of peaks from the heavy atoms at the higher time of flight. This was the only feature present in the back scattering spectrum in **Figure 4.7b**. This heavy-atom feature was not examined in the forward scattering spectrum but rather in the back scattering spectrum where the signal is stronger because the majority of the neutrons are scattered backwards by heavy atoms.

In **Figure 4.8** the neutron Compton profiles of the cement at the two times in momentum space were compared and it could be seen that the 61 h cement had a shift to higher *y* values, and yet the H NCS width at 61 h was bigger than that at 1.5 h.

The tail of the distribution in **Figure 4.9** was due to the momentum along the bond direction since the proton is most tightly bound in this direction [288], and comparison of the radial momentum distributions clearly showed that 61 h cement had a larger second momentum as was confirmed by the higher Compton profile width values in **Table 9**. The momentum distribution is determined nearly entirely by quantum localisation effects, and hence is a sensitive probe of the local environment of the proton. It was seen that the proton moved from a slightly anharmonic well at 1.5 h to a deeply anharmonic potential at 61 h that had an oscillation in the momentum distribution. The appearance of an oscillation in the momentum distribution is characteristic of a population of protons that are coherently distributed in the ground state of a double well potential [293]. Since the local environment of H in GIC is complicated by the fact that H-atoms are in several widely differing chemical states, including: COOH, $COO^{(\delta-)}$---$^{(\delta+)}H$---$^{(\delta-)}OH_2$ (H-bonded) $H_3O^{(+)}$ and as (some) free $H^{(+)}$ (as it is an acid polymer). As NCS results represent an average of the H potential, deconvolution of this signal to the differing H-components was beyond the scope of this work. Further interpretation of

anharmonic features in the forward scattering results was therefore not attempted as the current focus was on the overall qualitative trend.

The 0 h cement H-width value of 4.93 $Å^{-1}$ resolved for the PAA liquid-polymer being above the literature value of 4.841 $Å^{-1}$ for H_2O under the same conditions [288] showed that H atoms in the PPA felt a higher effective potential due to their neighbouring covalently-bound C and O atoms. This potential is also a measure of atomic confinement as well as the average bonding strength (cohesion) to the neighboring atoms.

The H-value (**Figure 4.10**) droped upon initiation of cementation and never regainsed the initial value in the separate PAA over the entire ~3 day setting time. This was rationalised by the fact that the -COOH ↔ $COO^- + H^+$ dissociation equilibrium was pushed to the right-hand-side upon initiation of the acid-base cementation reaction and retained there due to subsequent binding of COO^- with Ca^{2+}/Al^{3+} and H^+ with F^- /$H_xPO_4^{(3-x)-}$, respectively (where x = 0-2).

The NCS width of H also reflected the state of water in the setting cement being the result of the interplay between unbound and bound water. When the unbound free water in the polymer solution took part in the setting reaction it became structurally bound either within the silica hydro gel ($Si(OH)_4$•$X(H_2O)$, X = 1-6 in the primary solvation sphere) or in the polyacrylate salt gel. Water is also a reaction product of the acid-base reaction. Without tracing the origin of the water, the drop of the H NCS width may be the result of unbound water exceeding the amount of bound water and *vice versa*.

It has been shown in **Figure 4.11** that the general trend for H-atoms over setting held for all three temperatures. The higher values at 320 K were expected due to the greater amount of thermal energy in the system, exciting the atom's translattional, rotatational and vibrational dynamics with rising temperature. A possible explanation of the anomalous 12-hour width value at 280 K being higher than 300 K was that at the lower temperature setting was retarded and less complete, thus a larger portion of H-atoms would remain in their original state as in PPA, where they were characterised as having a higher potential.

DOI:10.14753/SE.2014.1974

5.2.1.2 Back scattering

The stability and reliability could be appreciated through the simple comparisons made in **Figures 4.12-14**.

C, O, F and Ca being the common elements in the two sets of data analysis routines for stoichiometric-fitting of the back scattering data, their peak width values were obtained in each routine. These values were compared and they were not significantly different, also showing the reliability and feasibility of the technique.

Al, Si and P are glass-forming atoms and it was seen they had similar trend over time (**Figure 4.15-1**). In the glass powder, Al and Si are in tetrahedral oxide form where the O-Al/Si-O bonding is relatively strong. Upon mixing, H^+ ions from the acid attack the glass and hydrolyse it, breaking the tetrahedral linkages forming silicic acid together with release of Na^+, Ca^{2+} and Al^{3+} ions. These accumulate in the aqueous phase possibly as fluoride complexes, hence, the drop of Al and Si kinetic energy values at 1.5 h. Later, the silicic acid ($Si(OH)_4$) polymerises and forms silica gel [$(OH)_2Si$-$(SiO_4)_n$-$(Si(OH)_2)$•XH_2O] contributing to the increased mechanical strength as cement matures, as reflected in the rise of the Si-value from 8 h to 16 h, subsequently plateauing (terminus of silica gel formation). Al^{3+} cations form salt bridges with the polymer, reflected in the measured atomic cohesion for Al from 3 h to 5 h. P also forms complexes with Ca^{2+} and Al^{3+} shown as a rise followed by decomplexation as the cations form salt bridges with the polymer, reflected in the drop of value. Overall, within the first 5 h the glass-forming cations achieved the highest kinetic energy.

Similarly, the glass-forming Na^+ and Ca^{2+} atoms also achieved the highest kinetic energy early on at around 5 h (**Figure 4.15-2**).

O and F anions displayed a similar trend - the kinetic energy increased up to 5 h (O up to 3 h) then decreased through to 16 h before plateau (**Figure 4.15-3**). F^- ions were released from the glass and formed complexes with Ca^{2+} and Al^{3+} resulting in observed bonding strength increase, with F^- facilitating their release from the glass. Competitive cross-linking occured with the acid polymer, effectively decomplexing the F-Ca/Al species and freeing F^- ions evidenced by the decrease in fluorine's bonding strength. As O is highly electronegative an accompanying concentration of local electron density was expected, which became more pronounced with increased populations of O^- and O^{2-} (upon acid-attack on the glass) thus the raised bonding strength, peaking at 3 h. When

Ca^{2+} and Al^{3+} cross-link the acid polymer, they draw (-)-charge density from the O-atoms, attaining their highest kinetic energies in the setting while weakening the bonding-strength of O, which was reflected in the value drop after 5h.

C (**Figure 4.15-4**) exhibited the opposite trend of that of the glass-forming atoms: when the glass and liquid were first mixed the protons reacted with the glass leaving the vicinity of the polymer acid so the potential felt by C reduced - the initial drop in the plot. Then Ca^{2+} and Al^{3+} formed salt bridges with $–COO^-$ groups increasing C potential up to 12 h. The electrons oscillated between C and O atoms, which was reflected by the up and down trend established from 16 h onwards.

The opposite trend of C and Al could easily be seen from their kinetic energy values over time plotted together in **Figure 4.15-5**.

The majority of the elements responsible for the mechanical properties of the cement achieved the highest values early on within 5 h, which was in line with the results for H where the highest NCS peak width and KE values appeared around the same period.

5.2.1.3 Qualitative GIC NCS width

Figure 4.16 shows the evolution of derived GIC NCS width values over setting time. It is seen that early upon setting NCS width is in the incline and at ~8 h it reaches the first maximum followed by a dip between 12-16 h before it rises slowly again.

Figure 4.17 is the GIC NCS values of all three temperatures over cementation. Although these are qualitative the oscillatory trend persists. At 280K the trend is delayed due to the lower temperature slowing down the reactions. And the fact that GIC values lie between those of glass and polymer validates the trend.

5.2.1.4 Conversion of NCS values to engineering units

Few previous studies have characterised fracture toughness in the 1-24 h period - focus has always been on the post-24 h period - hence the literature is devoid of any comparative values. In the few studies that studied early K_C, the values at 5 h are the same and even higher than the 24 h value [94,95]. It was indicated that the fully set cement is over-crosslinked which may result in the brittleness [94].

In terms of single particle scattering NCS peak width is a measure of atomic potential and confinement (cohesion) effect. When NCS width is large the Morse

potential is narrow and deep, and shallow and wide when width is small. The calculated mean kinetic energy is proportional to the amount of energy needed to put an atom in recoil state. In terms of atomic fracture, this KE will be proportional to the amount of energy needed to break the bonds, which resembles fracture toughness. Therefore, NCS widths and intrinsic fracture toughness are expected to be related. Indeed it was found that measured peak width values for GICs and its related groups (**Figure 4.18**) vary inversely with reported values of K_C.

The inverse trend between K_C and NCS width shows NCS width increasing as literature K_C values decrease from glass, to GIC, to polymer. NCS peak widths predicted from elemental widths in the glass for SiO_2 and CaF_2 and their known K_C values, closely follow the empirical relationship in **Figure 4.18**.

The breadth of the K_C data for each material increases between silica glass and the polymers. This related to the statistical nature inherent in fracture mechanics methods (~10%) and sample-to-sample variability, governed, for example, by glass particle sizes in GICs, and by molecular weight in polymers. Nevertheless the dashed curve provides a practical look-up-table to calibrate NCS widths in $Å^{-1}$ with fracture toughness in MPa $m^{0.5}$. It has been used to convert the overall NCS widths of 300K GIC in **Figure 4.16** into overall GIC fracture toughness in **Figure 4.19**, the overall NCS widths of GIC at all three temperatures in **Figure 4.17** into overall GIC fracture toughness at three temperatures in **Figure 4.20** and the elemental NCS widths in **Table 10** into elemental toughness in **Figure 4.21**. Where K_C values can currently be calibrate to within 10%, the errors in measured NCS width, point by point, are typically $\leq$ 5% for the present neutron statistics. Fracture toughness calibration could be improved incorporating specimen-specific measurements of K_C in place of global literature values. Higher neutron counts would improve the relative precision further.

Marked non-monotonic changes also occur in the intrinsic fracture toughness developed over setting and this has an inverse trend of that of the NCS values in **Figure 4.16**.

In order to describe the setting mechanism from the features observed, the following three terms were assigned to mirror the three stages in setting reactions (**Section 1_1.4.3**):

1. *Coupling point* (or initial setting point): ~ 3 h where glass and polymer dynamically engage and K_C drops sharply, may correspond to the end of "decomposition of glass powder;"
2. *Setting point*: ~ 8 h, setting reactions continue into "gelation" stage and stress builds up at the interface, the decline abruptly changing to define an interim setting point;
3. *Interfacial stress zone*: between 12-16 h, the vigorous setting reactions are at a halt and the stress induced by the setting starts to relax - decreasing K_C unexpectedly recovers and from this point on stress-induced weakening of interfaces reduces overall toughness. Thereafter K_C levels out asymptotically in the next 2 days, towards baseline toughness of the starting mixture. This may be onset of "long-term setting and hardening."

The same trend persists at all three temperatures (**Figure 4.20**) and from the marked setting point of 6.9 h at 320 K, 8.0 h at 300 K and 9.3 h at 280 K as well as interfacial stress zone of 13.2 h, 14.0 h and 14.4 h at the three temperatures respectively, the setting reactions proceeded fastest at elevated temperature of 320 K and the slowest at 280 K.

Elemental fracture toughness fluctuates considerably, with hydrogen and fluorine (**Figure 4.21a**) having small NCS values and therefore wider inter-atomic potentials. With the NCS width of H reflecting the state of water in the setting cement and the fracture toughness being the macroscopic result, it makes perfect sense that the unbound water acts as plasticiser to contribute to the overall toughness. Same for fluorine, the released small molecule of fluoride also acts as plasticiser to contribute to higher toughness through flexibility.

By contrast the values for oxygen and aluminium (**Figure 4.21b**) display distinctively different setting time structures. Both elements have larger NCS values, thus narrower inter-atomic potentials, mainly contributing to the feature at 16 hours but also to eventual embrittlement. The evolution of different Al coordinations may be the cause of aluminium value fluctuation, which is best characterised with neutron diffraction.

The literature is devoid of any indication that the problem of brittleness in GICs may be solved through retention of maximal toughness by rational chemical manipulation.

The results here indicate that termination of the setting of GICs at early stage (~ 16 h in this particular composition studied in this work) may retain the maximal toughness and results in tougher and less brittle cements.

5.2.2 Neutron diffraction experiments

GIC structure is amorphous and non-periodic. There is no major changes in the high-*Q* region of the *F(Q)* plot (**Figure 4.22**) since the first (nearest) neighbouring atomic environment in GIC does not change on setting for the majority of atoms present. The major changes are expected to occur at the interface between the glass cores and the matrix. Thus, the greatest changes expected will be dependent on the proportion of this interface in the sample. The measurement was performed on a hydrogenous sample, hence the incoherent background is very large and the structural signal is only a small fraction of the total. Future measurements on deuterated polymers will afford the best chance of observing & quantitatively tracking structural changes in the bonding environment.

In situ S(*Q*) experiments (**Figure 4.23**) provide insight into developments in nano and atomic structure during setting. The long-range order exhibited by the polymer is also to some extent present in the GIC because not all the carboxyl groups covert to carboxylate groups [20] - the remaining carboxyl groups still retain the long-range order. The most changes in GIC take place in the organic-inorganic interface so focus is on the near and intermediate range of Q=0.5-2 $Å^{-1}$ (**Figure 4.24-1**).

The oscillatory trend of *S*(*Q*) of the time series in **Figure 4.24-1** is that the value goes up over time from 0.5 h on until 14 h when a drop appears and it goes back up at 24 h to the level of 4 h. This trend can also be represented with two parameters:

1. Integrated peak area in the Small Angle Neutron Scattering (SANS) region in the Porod range Q=0.5-0.95 $Å^{-1}$: SANS principally detects changes at the organic-inorganic interface (**Figure 4.24-2a**), first increasing, as gelation and chelation establish, then falling and rising again, indicating the development of internal strain subsequently released.
2. First Sharp Diffraction Peak (FSDP) position Q_{FSDP}: FSDP (**Figure 4.24-2b**) relates directly to intermediate range order in the glass [289], initially decreasing as the

fluoro-phosphate phase is depleted. The subsequent increase is consistent with compression in the remaining glass, followed by decompression.

Taken together, SANS and FSDP variations suggest interfacial weakness develops within the first 24 hours of setting. Indeed our previous Hertzian indentation study (**Sections 4_4.1 and 5_5.1**) has shown that this is where macroscopic cracks develop.

Since the majority of the pair distribution functions are in the range 1-2.6 Å (**Figure 4.25**), the focus is then on this region.

For the cement at different setting times (**Figure 4.26**) the changes on the short range cement structure take place between 1 ~ 2 Å. The atomic bond types originating from the polymer and persisting in the setting GIC are identified as C-O, C-C, O-C-O and are marked in orange; the ones originating from the glass and persisting in the setting GIC are identified as P-O (both non-bridging and bridging types), Si(IV)-O, Al(IV)-O/F, Al(IV)-O/F, Ca/Na-F, O-Si/Al-O and are marked in blue. C=O, PAA-Al(VI)-O and Ca/Na-O marked in green may arise from the setting reactions.

Allegedly, some of the above assigned features may simply be Fourier transform truncation ripples due to the low signal/noise ratio obtained with the protiated system. Even if not, the complicated change of each pair distribution function over setting is difficult to discern. This problem can be partially solved by taking the difference of $g(r)$, $\Delta g(r)$, between chosen time points (**Figure 4.27**).

$\Delta g(r)$ (**Figure 4.27**) is very effective in showing the Al-coordination switch during setting, notably in the vicinity of the K_C maximum at ~14-16 hours. The coordination of aluminium shifts from Al(VI) to Al(IV) and then back to Al(VI), following the rise and fall of toughness as internal interfacial stress is first generated and then released. Both swings in nanostructure (SANS and FSDP) and atomic structure ($g(r)$) coincide with the rise and fall of toughness *K*c around 14-16 hours.

As to how Al(IV) is related to higher *K*c (higher flexibility) and how Al(VI) is related to lower *K*c (lower flexibility), we need computational modelling to elucidate this.

5.3 Complementary experiments

5.3.1 Differential Scanning Calorimetry (DSC)

Upscan-1 curve (**Figure 4.28**) shows four clear enthalpy responses:

1. An endothermic process taking place in the temperature range of 94 - 316 °C, which could be related to the decomposition of the organic impurity in the glass powder.
2. A large exothermic process occurring in the temperature range of 316 - 460 °C, which is the manifestation of typical energy release in a hyper-quenched (>10^4 °C/s) glass upon thermal excitation.
3. An endothermic process overlapping with the end stage of 2. This response is attributed to the glass transition (T_{g1} = 425 °C).
4. An endothermic process occurring above ~ 480 °C, which has the feature of glass transition (T_{g2} = 513 °C). The two glass transition peaks indicate the co-existence of two glass phases, i.e. G338 is phase-separated.

From the upscan-2 curve, only the standard enthalpy responses of the two glass transitions can be seen, since both the decomposition of the organic impurity and the energy release of the hyper-quenched glass have been completed during upscan-1. At the same time we also see that the two glass transition peaks are more separated compared to upscan 1. This implies that the phase separation is enhanced during the first up- and down-scan (heating-cooling) cycle.

Based on these results, it is concluded that G338 glass possesses the following features:

1. The glass was hyper-quenched during casting of the glass melt. This means that this glass has a higher fictive temperature T_f well above T_g, i.e. it has a higher potential energy state than a normal glass, which makes the glass more reactive with the polyacid, and hence, improves the setting behavior of GIC cement and the high toughness of the final cement after setting.
2. The glass has a high tendency to phase separate, which is the direct result of hyper-quenching process. Such phase-separated glass is more reactive than a one-phase glass. This is also observed by other authors [126,290]. But they did not answer whether the two phases exist even in the as-quenched samples. The main phase

could be of aluminosilicate, whereas the minor phase could be fluro-apartite. However, close examination of upscan 2 shows an additional slight endothermic response between T_{g1} and T_{g2}, which may be a third unrecognised phase.

3. The main glass phase has a lower T_g compared to the minor phase, and to other types of GIC glasses [126,290-292]. A lower T_g is attributed to reactive glass.
4. The glass phase with T_{g1} = 425 °C exhibits a much larger C_{pl}/C_{pg} ratio than the glass phase with T_{g2} = 513 °C, indicating that the glass is a fragile composition since the ratio is proportional to the liquid fragility. The relation between the fragility and reactivity for this glass needs to be further explored.

Features 1-3 can impact significantly on GIC setting properties and the mechanical properties of the set cement. This might explain the initial drop of GIC potential shown as the drop in GIC NCS width values in **Figure 4.17**, the high potential of the strained glass caused by the hyper-quenching is first released from reaction with the acid polymer.

The 60-h GIC cement has similar features as the upscan-2 plot of G338. It seems cementation has the same effect as heat annealing in allowing the glass to release the stress created in the glass by hyper-quenching. And the similar features as upscan-2 is expected because with the un-reacted glass being the major phase (filler phase), the heat response of the cement resembles that of the glass.

In the whole DSC output up to 1200 °C in **Figure 4.29** the deep exothermic peak ~ 660 °C is a crystallisation peak. The three endothermic peaks above this temperature are phase transitions, the nature of which is unknown. The endothermic peak centered ~ 1050 °C is the result of fluorite evaporation. So the glass' thermal response displays two sharp glass transitions T_g, anticipated by a broad exothermic relaxation peak and crystallisation followed by phase transitions before polymer decomposition.

The initial 5% mass loss could be the evaporation of water and the drastic 10% mass drop is the result of the fluorite decomposition.

5.3.2 Transmission Electron Microscopy (TEM)

TEM image (**Figure 4.30**) showed obvious phase separation of 50 nm globules within a matrix, attributed to apatite and aluminosilicate respectively. Finer structure within the

globules may relate to hierarchical scaling or to a third glass phase, evidence for this coming from the shoulder between T_{g1} and T_{g2} in **Figure 4.28**.

5.3.3 Coherent Terahertz Spectroscopy (CTS)

As the cement sets the intensity of the peak > 325 GHz increases (**Figure 4.31**) indicating that the intra-molecular vibrations in the higher energy range get stronger over time, which is true as upon mixing the static glass and polymer start to react and the local environment of the molecules changes and their interactions increase. Due to the relatively narrow frequency range of 220 - 325 GHz accessible in this study, the two major peaks < 220 GHz and > 325 GHz cannot be resolved. Recasting of these plots in **Figure 4.31** by subtracting from them the spectral response of the 5-minute trace, helps elucidate the activity within this test setup.

The difference plots in **Figure 4.32** have been sectioned into three frequency sub-domains, 220-262 GHz, 262-284 GHz and 284-325 GHz, and the trend over setting could be qualitatively recognised:

- In the 220-262 GHz range, the intensity decreases as the cement sets.
- In the 262-284 GHz range, the same trend holds but it reverses from 12 h onwards. This is the transition region.
- In the 284-325 GHz range, the intensity increases as the cement sets. The change in this sub-domain is more marked than that in the lower set, being ~ 3 fold in scale. The peak centers red-shift over time, indicating more molecular interactions as the cement sets.

It is seen from **Figure 4.33** that:

- At the lowest frequency of 220 GHz, there is no significant change in the cement over 30 h of setting. The same is seen in **Figure 4.31** that at this frequency all the plots overlap. At 240 and 260 GHz the intensity initially plateaus and then asymptotically decreases.
- At the intermediate frequency of 280 GHz, the initial plateau shown at the lower frequencies initially rises before descending into and then climbing out of a trough at approximately the 6.5 h mark.

- At the higher frequencies of 300 and 320 GHz, the same trend is accentuated with the trough occurring earlier, approximately 2.4 h at 300 GHz and 1 h at 320 GHz. The scale of the initial intensity decrease diminishes, while the scale of the ensuing intensity increase climbs to level off asymptotically.

Taking the difference between the highest and lowest points at each frequency reveals the most change, ~ 50%, takes place at ~ 300 GHz.

GIC plots being in the middle of those of glass and polymer is expected as GIC is the mixture of these two components and setting features are the results of their reactions. Initially this falls after calcium is released and then recovers to the point where aluminium emerges, each initiating gel formation and chelation respectively [4]. As the polyacrylic acid component gradually hardens into a percolating matrix around the glass powder, THz modes first dampen approaching the absorbance of the polymer component (**Figure 4.34**). Interestingly the CTS frequencies fall amongst the collective modes found in inorganic glasses and zeolite structures, and are typical of two level systems [289,293]. Accordingly subsequent growth in absorbance points to increased THz coupling between polymer and glass components. Indeed the minimum at 3 hours setting, where this starts, aligns with the first feature in the elemental toughness of hydrogen and oxygen, elements which dominate the composition of GIC. Furthermore the inflection point in THz absorbance ~10 h coincides with the setting point in K_C (**Figure 4.19**). Low frequency collective vibrations clearly influence the setting of cement.

Although the changes in material absorption coefficient are usually correlated with changes in density, the ~ 18% change observed over setting in this study (**Figure 4.35**) being larger than the 2-3% GIC setting contraction, the oscillatory change observed is indeed due to cementation.

5.3.4 Computational Modeling

Preliminary Al-coordination permutation models (**Figure 3.5**) were constructed to characterise the influence of axial and equatorial ligands on ^{27}Al-NMR shifts relative to the experimental standard ($AlCl_3$•$6H_2O$). Tetrahedral (Td), trigonal bipyramidal (Tbp), square-based pyramidal (SBP) and octahedral (Oh) Al was ligated by H_2O and

DOI:10.14753/SE.2014.1974

carboxylic acid; the latter as CH_3COO^- in both mono- and bi-dentate configurations (**Figure 3.5**). Where required, a non-coordinated F^- was included to charge-balance the models to be neutral overall. All structures were geometry-optimised and confirmed as residing at a minimum on their respective potential energy hyper-surfaces (PEHSs) with analytical frequency computations.

NMR predictions (**Figure 4.36**) for ^{27}Al-chemical shifts (relative to $AlCl_3 \bullet 6H_2O$ set to 0 ppm) for multiple Al-polymer models show results basically in good agreement with experiment [110], except for that theory predicts shifts for Al(IV) and Al(VI) to extend further up- and down-field, respectively, than the experimental assignments. The experimental-theoretical agreement validates the preliminary models accuracy. However, a pronounced amount of region-overlap (i.e. Al(IV) upfield of V and VI coordinates) leads to the conclusion that further and more-extensive modeling is required. Thus the bigger model (**Figure 4.37**) was constructed.

The most stable structure is the Al(V)-coordinate square-based pyramidal (SBP) featuring two equatorial carboxylate links to the polymer with one bridging oxygen linking with the glass. This SBP configuration is dynamically linked to tetrahedral and octahedral arrangements. These frequencies influence the molecular conformations resulting in Al configurations. Interestingly transferring between aluminium coordinations involves local stress; expansion and compression of the Al(V) SBP structure yields tetrahedral Al(IV) and strained octahedral Al(VI) structures, respectively (**Figure 4.38**). The former occurs through a reduction of one carboxylate group, the latter via the formation of a new Al-carboxylate interaction, with concurrent twisting and weakening of the two carboxylate ligatures.

This emphasis show changes in the number of oxygen coordinated to aluminium are dictated more widely by conformational changes in the polysalt complex. Considering the compressive stresses that build up within the organic matrix during hardening through the formation of octahedral complexes, and the shrinkage of the glass particles (**Figure 4.24-2**), both should result in tension at the interface, which would explain the observation of the Al(IV) Td structure as the toughness maximum (**Figure 4.19**) is approached. Thereafter, the restoration of the octahedral Al(VI) structure concurs with internal interfacial stress being released (**Figure 4.38**). This is consistent in turn with the

DOI:10.14753/SE.2014.1974

development of interfacial flaws, ultimately reducing strength σ_Y, propagating when compressive stress is applied externally (**Sections 4_4.1 and 5_5.1**).

The majority of the numerous vibrational modes determined for these multi-atom models show a distinct red-shifting with increasing Al(IV) structures, indicating flexible sites consistent with increased deformability of the interface (**Figure 4.39**). Conversely, the majority of the modes blue-shift with increasing Al(VI) structures, indicative of a more rigid connection which would explain the increasing brittleness observed at later setting times. The difference in the relative contributions of the vibrational modes and zero point energies to the overall Gibbs Free-energies for these related models show the clear dominance of low-energy (<15 THz) collective modes (**Figure 4.39**). The predictions highlight the relationship between Al-coordination and overall flexibility or rigidity. Moreover, these coordination changes are reversible due to their being effected through changes in carboxylate ligatures, and mimic the Al(VI) – Al(V) – Al(IV) conversions found from this *in situ* structure factor experiments (**Figure 4.27**).

Selected collective vibrational modes calculated for this Al(V) model (**Figure 4.37**) are shown in **Figure 4.40**, with mode intensities matching other experimental and theoretical determinations on glasses and polymers. These THz frequencies clearly influence the molecular conformations that result in different aluminum configurations.

DOI:10.14753/SE.2014.1974

6 CONCLUSIONS

Glass ionomer cements (GICs) have been in use for over 40 years and show promise for continued evolution in extensive applications spanning dentistry to orthopedics, and beyond. The existing body of literature on GICs covers a broad range of approaches and techniques, all with common focus on the effective resolution of its structure, setting mechanism and final chemical, physical and mechanical properties as well as its biocompatibility. Current descriptions of GICs are as a composite of unreacted glass particles sheathed in silica gel and embedded in a polyacrylate salt gel matrix. They are the reaction product of an acid-base reaction between the liquid-polymer and powder-glass components. Interphase bonding is driven by the formation of Al^{3+}/Ca^{2+} - polyacrylate salt bridges at glass particle surfaces. Silica gel ($Si(OH)_4 \bullet X(H_2O)$) and various phosphates ($H_x(PO_4)^{(3-x)-}$, with x = 0-3) also form an inorganic network contributing to the long-term mechanical properties. GICs' inherent and durable adhesion results from an ion-exchange interface formed between GICs and teeth or bones. Fully set GICs are hard materials with sufficient service-strengths, yet their brittleness restricts them to non-load bearing applications. The salt bridge interphase and interfacial bonding is responsible for the brittleness evidenced by preferential crack-propagation along interfaces under material failure. Extensive characterisation of the Al-polyacrylate salt bridge using differing techniques (IR, NMR, etc.) has led to the conclusion that a portion of the Al coordination evolves from IV→V→VI during cementation, driving relevant time-dependent property changes of GICs. Specifically, maximising Al(VI) coordination and cross-linking was thought to be most desirable for increasing strength. However, several recent works evidence GICs as being over-crosslinked, and potentially the underlying aspect of their observed low fracture toughness (i.e. brittleness); increase of strength at the detriment of toughness is well established in materials science.

DS/ISO/R 1565:1978 - directed mandates have orphaned material and mechanical characterisations of GICs to the post-setting domain (i.e. > 24 hours), whilst atomistic descriptions are severely lacking or entirely absent.

DOI:10.14753/SE.2014.1974

In the work presented in this dissertation:

Mechanical testing and fractographic studies confirmed that apart from the high porosity, the weak interfacial bonding between glass cores and the polyacrylate salt gel matrix is responsible for the brittle failure of GICs under Hertzian indentation.

Neutron Compton Scattering (NCS) results showed the changes of elemental Compton profile width, mean kinetic energy and 3-D harmonic oscillator frequencies as well as the hydrogen momentum distribution over setting-time. These were used to derive overall NCS width for the GIC composite, subsequently converted to intrinsic fracture toughness in MPa $m^{0.5}$. Fracture toughness showed an overall decreasing, yet non-monotonic trend over setting time, with an unexpected recovery of toughness at the ~16 hour mark. Small and Wide Angle Neutron Scattering (SANS and WANS, respectively) results showed complementary oscillatory trends, evidenced by a recovery of Al(IV) at the ~10-16 hour mark.

Coherent Terahertz Spectroscopy (CTS) reflected the non-monotonic trends with an overall undulating signal over the first ~16 hours of setting, including a 'coupling point' at ~3 hours where gelation dominates, followed by subsequent interfacial growth between the polymer and glass components. Transmission Electron Microscopy (TEM) imaging showed that the glass nanostructure comprises extensive phase-separated domains, supported by two sharp glass transitions T_g in the DSC determinations of the glass component.

Quantum chemical computations showed general agreement with NMR determinations, with Al(IV) being downfield of V and VI coordinates; the experimental-theoretical agreement validating the models accuracy. However, a pronounced amount of region-overlap (i.e. Al(IV) upfield of V and VI coordinates) lead to the conclusion that further and more-extensive modeling is required. Larger interfacial models involving a model-glass and a polyacrylic-acid heptamer were built and showed the square-pyramidal Al(V) structure to be the most stable in Gibbs free-energy. Structural modulation of the heptamer models built simulated stretching ($Al^{V\rightarrow IV}$) and compression ($Al^{V\rightarrow VI}$), showing a distinctive red- and blue-shifting, respectively, affirming Al(IV) coordination to be more flexible and Al(VI) to be more rigid (and thus brittle).

DOI:10.14753/SE.2014.1974

An unexpected oscillatory setting profile has been observed both in high-energy neutron scattering, small and wide-angle neutron diffraction and low-energy CTS experiments, with complementary results provided by computational models using density functional theory.

The initial expectations and beliefs that setting is monotonic or '1st order' and thus that the oscillatory trends observed were somehow flawed or 'unphysical' in nature. However, exhaustive literature searches turned up several works showing an oscillatory trend over setting time in GICs, measured with differing techniques and spanning several decades (**Figure 6.1**), including cation-precipitation, extrinsic fracture toughness and NMR characterisation of changing coordination ratios Al(VI)/Al(V) +Al(IV). This further supported the possibility that cementation in these glassy cementitous systems may in fact not be monotonic, as previously thought. In each of these works, these trends occurred in the ~1-16 hour time period, mirroring the pre-24 hour times highlighted in this dissertation.

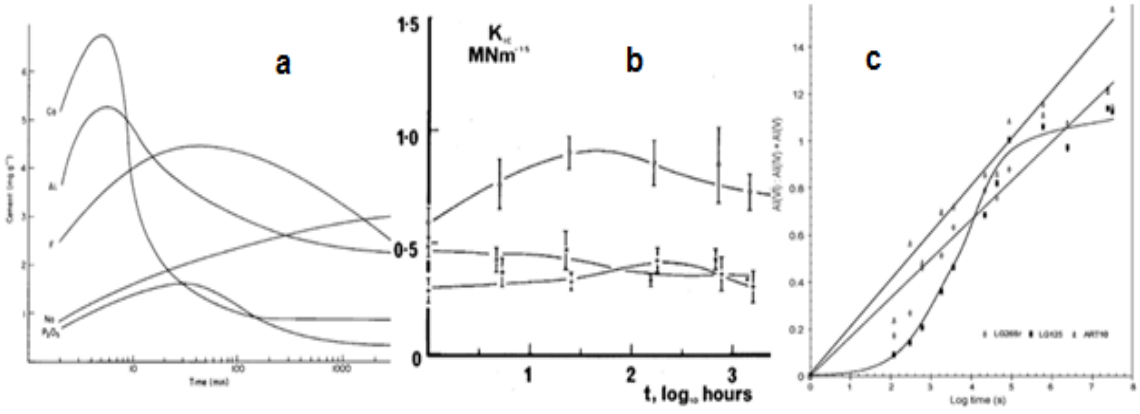

Figure 6.1 Time-dependent ordinating trends adopted: (a) from [51]; (b) from [85]; (c) from [110].

The explanation for this observation is discussed in detail in the previous sections, and may be summarised in the following key conclusive points:

1. Mechanical yield strength σ_Y and fracture toughness K_C of materials generally form groups [3] (**Figure 6.2**), ranging from soft to hard and with brittle to ductile behaviour. Within this scheme GICs and their components cluster around dentin and amalgam, the conventional restorative, in the zone occupied by industrial polymers. Although the plastic-zone size of dental materials is comparable with the

DOI:10.14753/SE.2014.1974

geometry of caries in the initial stage, GICs clearly have less toughness and strength than dentin.

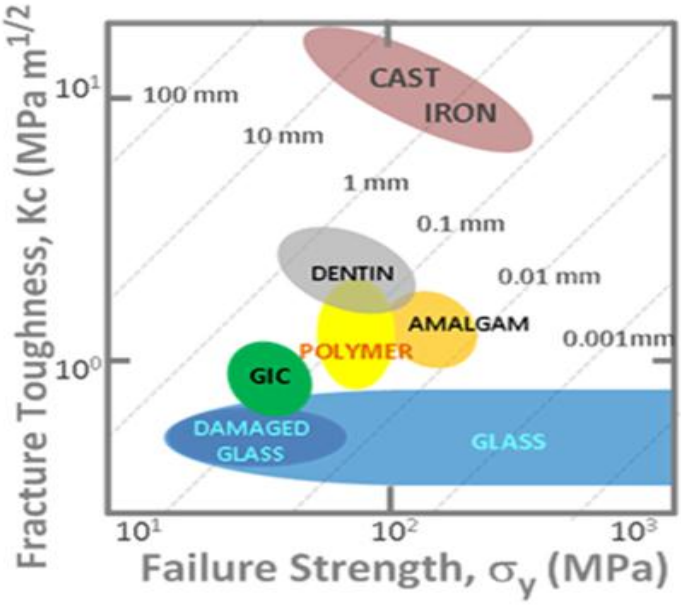

Figure 6.2 Toughness K_C versus Strength σ_F for dental materials, plastic zones $K_C^2/\pi\sigma_F^2$ shown by dotted lines, values taken from literature values, adapted from [3].

2. While strength σ_Y lies extrinsically in existing defects, such as cracks and voids, fracture toughness K_C, or damage tolerance, is intrinsic to the material. For composites like GICs both σ_Y and K_C clearly develop during the setting process from a deformable incompressible slurry to a compressible gel, then rigid cement. Usually, the more rigid a material is, the higher its shear modulus G, the lower the toughness K_C and the more brittle it is. Conversely deformability correlates with toughness and ductility. Atomistically, compressibility κ relates directly to the shape of the interatomic or Morse potential [91], the narrower this is, the stronger and more rigid the chemical bond and *vice versa*. In particular, Poisson's ratio ν [91], a function of $1/G\kappa$, reveals a sharp demarcation around ν=1/3 between brittleness and ductility when this is expressed through the Fracture Energy G_C [294] (**Figure 1.7**). As setting advances, ν falls from around 0.5 to 0.3 leaving GICs marginally more brittle than dentin or amalgam. During this process inter-component bonding in GICs develops as the rigid μm size glass particles come into contact with the deformable aqueous polyacrylic acid. Macroscopically, these

organic-inorganic interfaces are where mechanical failure eventually occurs with the generation of extrinsic faults which affects σ_Y.

3. At the molecular level water leaches into the glass, as for other tetrahedral oxide glasses, rupturing bridging oxygens to form SiOH and AlOH groups, and initially creating an alumina-siliceous gel at the surface. Ca^{2+} and Na^{+} ions, that charge-compensate AlO_4 polyhedra in the glass powder, are released ahead of Al^{3+} ions, the latter predominately cross-linking the polymer acid to form a strong polysalt matrix. Al-chelation accompanies the conversion of $Al\text{-}O_4$ to high coordinate sites and appears pivotal in the resulting mechanical properties of GICs. Hydration has two effects: 1. weakens the glass network and facilitate ion leaching; 2. promotes ionisation of the polymeric carboxylic acid, formation of salt bridges to a stronger Al network. Hydration is accompanied by increase in strength and decrease of plasticity (toughness) [295]. So the origin of brittleness is the bonding at the matrix-filler interface, especially the higher Al-coordination at the later setting stage (stronger but more brittle, proved from DFT results in **Sections 4_4.3.4 and 5_5.3.4**) and loss of water from the matrix.

By juxtaposing *in situ* neutron methods with CTS and DSC, underpinned by computational models, it has been shown how complexities occurring during the setting of GIC dental composites can be unravelled structurally, energetically and dynamically at the atomic level. The unexpected non-linear/non-monotonic setting reveals repeated toughness episodes where atomic cohesion is reduced, with evidence of the circumstances promoting micro-cracking at the glass-matrix interface. Fracture toughness has been monitored non-destructively *in situ* during GIC setting and the source of evolving brittleness has been uncovered as the bonding at the matrix-filler interface. This battery of techniques will also offer advantages for studying mechanical toughness in other types of cement non-destructively during setting. It is envisioned that chemical or physical termination of cementation at an early stage (i.e. pre-24 hours) may allow for retention of the composites fracture toughness intrinsic to its gel-phase. With elevated fracture toughness GICs may be subjected to extended applications including load-bearing applications.

DOI:10.14753/SE.2014.1974

It is expected that the insight afforded by this battery of *in situ* non-destructive techniques will assist in improving the performance and rational design of cementitious materials, by quantifying the incipient atomistic processes during setting that dictate long-term mechanical toughness.

Ongoing work includes measurement of extrinsic fracture toughness at early stages of cementation using traditional toughness testing (i.e. double torsion and Hertzian indentation tests) and quantitatively characterising the relationship between glass thermal history and the mechanical properties of set GICs. Time-resolved tracking of hydration using Quasi-Elastic Neutron Scattering (QENS), and SANS/WANS will provide the atomistic complements to these bulk determinations. Isotopic-labeling of the polymer component will allow for better resolution in the QENS and SANS/WANS determinations and is currently under-development.

Future focus is to apply this multivariate methodology to characterise the structure and mechanical properties of other cementitious materials including cements, concretes and adhesives.

DOI:10.14753/SE.2014.1974

7 SUMMARY

Bio-cements, exemplified by glass-ionomer cements (GIC), have been in widespread use for over 40 years in dentistry, and more recently in a variety of orthopedic and related surgical applications. Comprised of a polymeric acid and an aluminosilicate glass powder, GICs exhibit good biocompatibility and bioactivity, stimulating tooth and bone remineralisation. Optimisation of their mechanical properties has, however, been less successful, with these composites continuing to fall short of the toughness requisite for permanent implants. The continued use of conventional mechanical (failure) testing methods, which are necessarily retrospective, has been a significant impediment to improvement. This, coupled with the complete lack of atomistic details of structure and cementation dynamics, has relegated GICs to non-load bearing applications.

The focus of this dissertation is to remedy these shortcomings through a trans-disciplinary approach spanning micro- through macro-scopic determinations. A novel combination of Hertzian indentation testing and subsequent fractographic studies with *in situ* neutron scattering, complimented by differential scanning calorimetry, coherent terahertz spectroscopy, and quantum chemical modeling, has been employed towards the quantitative and *non-destructive* characterisation of practically-relevant GIC systems. Results show how complexities occurring during GIC-setting can be unraveled structurally, energetically, temporally and dynamically at the atomic level. Time-resolved trends reveal a recovery of toughness at ~10-16 hours after initiation of the cementation reaction. It is envisioned that chemical or physical termination or modulation of setting at an early stage (i.e. pre-24 hours) may allow for retention of the composites fracture toughness intrinsic to its gel-phase.

It is expected that the insight afforded by this battery of *in situ* non-destructive techniques will assist in improving the performance and rational design of cementitious materials, by quantifying the incipient atomistic processes during setting that dictate long-term mechanical toughness.

DOI:10.14753/SE.2014.1974

8. ÖSSZEFOGLALÓ

A biocementeket, ahogy az üveg-ionomer cementeket (GIC) is, az elmúlt negyven év alatt a fogászatban elterjedten alkalmazták. Újabban az orthopédiai és csontsebészetben is használják ezeket az anyagokat. A polimersav és alumínium szilikátüvegpor összetevőkből álló GIC kiváló biokompatibilitással és bioaktivitással bír. Ennek köszönhetően serkenti a csont és fog keményszöveteinek a remineralizációs folyamatait. A tartós beültetéssel szembeni elvárásoknak nem sikerült teljes mértékben eleget tenni, mert ezeknek a kompozitoknak a törési ellenállása alacsony, ez annak köszönhető, hogy eddig még nem sikerült a mechanikai tulajdonságaikat a kívánt mértékben javítani. A konvencionálisan alkalmazott mechanikai tesztek, melyek retrospektív vizsgálatokban hasznosak ugyan, de a fejlesztést nem segítették. Ez, valamint az atomi struktúra elemzése, valamint a kötési dinamika vizsgálatának teljes mellőzése vezetett oda, hogy a GIC teherbíró képessége nem javult az idők során.

Ez a disszertáció transzdiszciplináris mikro- és makroszkópos vizsgálatok sorozatával pótolja ezt a hiányt. Hertzes indentációt követő fraktográfiai vizsgálatok, valamint az *in situ* neutronszórás, a differenciál pásztázó kalorimetria, a koherens tetrahertz spektroszkópia vizsgálatok mellett a kvantumkémiai modellezést alkalmaztuk, hogy az anyag roncsolása nélkül kvantitatív jellemzését nyújtsuk a kereskedelmi forgalomban lévő GIC-nek megfelelő kísérleti anyagnak. Az eredmények igazolják, hogy mennyire komplex folyamat megy végbe a kötés során, amelyet atomi szinten tisztáztunk a szerkezet, az energetikai az idő és a dinamika függvényében. Idő függvényében az ellenállás visszaalakulását mutattuk ki a kötés kezdetétől számított tíz óra múlva. Úgy véljük, hogy fizikai vagy kémiai úton történő megszakítása, vagy befolyásolása a kötési folyamat kezdeti szakában (az első 24 óra előtt) meg tudnánk őrizni a kompozit törési ellenállását annak gél fázisában.

Arra számítunk, hogy ezeknek az *in situ* roncsolás mentes technikáknak az alkalmazásával kvantifikálni tudjuk a kezdeti atomi szintű folyamatait a kötésnek, amely a hosszútávú mechanikai ellenálló képességet befolyásolja, minek következménye a cementek továbbfejlesztését segíti.

9 REFERENCES

[1] Westbroek P, Marin F. (1998) A marriage of bone and nacre. Nature, 392:861-862.

[2] Irish JD. (2004) A 5,500 year old artificial human tooth from Egypt: a historical note. Int J Oral Maxillofac Implants, 19: 645-647.

[3] Ritchie RO. (2011) The conflict between strength and toughness. Nature Mater, 10:817-822.

[4] Crisp S, Wilson AD. (1974) Reactions in glass ionomer cements: I. Decomposition of the powder. J Dent Res, 53:1408-1413.

[5] Mount GJ. Atlas of Glass-Ionomer Cements. 3rd ed, Martin Dunitz, London, 2002: 1-7.

[6] Nicholson JW. (2010) Glass ionomer dental cements: update. Mater Technol Adv Perf Mater, 25:8-13.

[7] Jonck LM, Grobbelaar CJ, Strating H. (1989) Biological evaluation of glass-ionomer cement (Ketac-O) as an interface material in total joint replacement: a screening test. Clin Mater, 4: 201-224.

[8] Brook IM, Hatton PV. (1998) Glass-ionomers: bioactive implant materials. Biomater, 19: 565-571.

[9] Bauer M, Pytel J, Vona I, Gerlinger I. (2007) Combination of ionomer cement and bone graft for ossicular reconstruction. Eur Arch Otorhinolaryngology, 264: 1267-1273.

[10] Hehl K, Schumann K, Beck C, Schottle W. (1989) Middle-ear surgery-glass ionomer cement at the incudostapedial joint. Laryngorhinootologie, 68: 490-492.

[11] Dicks F, Zollner W. (1988) Practicability of glass ionomer cement for veterinary dental practice. Praktische Tierarzt, 69: 32-36.

[12] Vujaskovic M, Karadzic B, Bacetic D. (2011) Histopathology of subcutaneous tissue reaction to endodontic root canal sealers. Acta Veterinaria (Beograd), 61: 327-336.

[13] Davidson CL. (2006) Advances in glass-ionomer cements. J Appl Oral Sci, 14(sp. issue): 3-9.

[14] Ten Cate JM, van Duinen RNB. (1995) Hypermineralization of dentinal lesions adjacent to glass-ionomer cement restorations. J Dent Res, 74: 1266-1271.

[15] Hotz P, McLean JW, Sced I, Wilson AD. (1977)The bonding of glass ionomer cements to metal and tooth substrates. Brit Dent J, 142: 41-47.

[16] Powis DR, Folleras T, Merson SA, Wilson AD. (1982) Improved adhesion of a glass ionomer cement to dentin and enamel. J Dent Res, 61: 1416-1422.

[17] McLean JW, Wilson AD. (1977) The clinical development of the glass ionomer cements. I. Formulations and properties. Aus Dent J, 22: 31-36.

[18] McCabe JF, Yan ZQ, Al Naimi OT, Mahmoud G, Rolland SL. (2009) Smart materials in dentistry–future prospects. Dent Mater J, 28: 37-43.

[19] Wilson AD. (1978) The chemistry of dental cements. Chem Soc rev, 7: 265-296.

[20] Culbertson BM. (2001) Glass-ionomer dental restoratives. Prog Polym Sci, 26: 577-604.

[21] McLean JW, Wilson AD. (1977) The clinical development of the glass ionomer cement. II. Some clinical applications. Aus Dent J, 22: 120-127.

[22] McLean JW, Powis DR, Prosser HJ, Wilson AD. (1985) The use of glass-ionomer cements in bonding composite resins to dentine. Br Dent J, 158: 410-414.

[23] Mount GJ. (1989) Clinical requirements for a successful 'sandwich'-dentine to glass ionomer cement to composite resin. Aust Dent J, 34: 259-265.

[24] Croll TP. (1989) Replacement of defective class I amalgam restoration with stratified glass ionomer-composite resin materials. Quin-tessence Int, 20: 711-716.

[25] Davidson CL. (1994) Glass-ionomer bases under posterior composites. J Esthet Dent, 6: 223-224.

[26] Croll TP, Cavanaugh RR. (2002) Posterior resin-based composite restorations: a second opinion. J Esthet Restor Dent, 14: 303-312.

[27] Croll TP, Nicholson JW. (2002) Glass-ionomer cements in pediatric dentistry: review of the literature. Pediatric Dentistry, 24: 423-429.

[28] Loguercio AD, Alessandra R, Mazzocco KC, Dias AL, Busato AL, Singer Jda M, Rosa P. (2002) Microleakage in class II composite resin restorations: total bonding and open sandwich technique. J Adhes Dent, 4: 137-144.

[29] Wibowo G, Stockton L. (2001) Microleakage of Class II composite restorations. Am J Dent, 14: 177-185.

[30] Dietrich T, Losche AC, Losche GM, Roulet JF. (1999) Marginal adaptation of direct composite and sandwich restorations in Class II cavities with cervical margins in dentine. J Dent, 27: 119-128.

[31] Gladys S, Van Meerbeek B, Lambrechts P, Vanherle G. (2001) Microleakage of adhesive restorative materials. Am J Dent, 14: 170-176.

[32] Hewlett ER, Mount GJ. (2003) Glass ionomers in contemporary restorative dentistry - a clinical update. J Calif Dent Assoc, 31: 483-492.

[33] Croll TP and Helpin ML. (1994) Space maintainer cementation using light-hardened glass ionomer/resin restorative cement. J Dent Child, 61: 246-248.

[34] Omar R. (1988) A comparative study of the retentive capacity of dental cementing agents. J Prosthet Dent, 60: 35-40.

[35] Kvam E, Broch J, Nissen-Meyer IH. (1983) Comparison between a zinc phosphate cement and a glass ionomer cement for cementation of orthodontic bands. Eur J Orthodont, 5: 307-313.

[36] Mount GJ. (1998) Clinical performance of glass ionomers. Biomaterials, 19: 573-579.

[37] Burke FJT, Watt DC. (1990) Cermet - an ideal core material for posterior teeth? Dent Update, 17: 364-370.

[38] Taleghani M, LeinFelder KF. (1988) Evaluation of a new glass ionomer cement with silver as a core build up under a cast restoration. Quintessence Int, 19: 19-24.

[39] Yardley RM. Custom core construction using glass ionomer cements. Dent Update, 17: 124-127.

[40] Shimokobe H, Komatsu H, Matsui J. (1982) Fluoride content in human enamel after removal of the applied cement. J Dent Res, 66(special issue): 131 (abstract 96).

[41] Frencken JE. (2009) Evolution of the ART approach: highlights and achievements. J Appl Oral Sci, 17(sp. Issue): 78-83.

[42] Frencken JE. (2010) The ART approach using glass-ionomers in relation to global oral health care. Dent Mater, 26: 1-6.

[43] Eden E, Topaloglu-Ak A, Frencken JE, Van 't Hof MA. (2006) Two-year survival of composite ART and traditional restorations. Am J Dent, 19: 359-363.

[44] Ersin NK, Candan U, Aykut A, Onçağ O, Eronat C, Kose T. (2006) A clinical evaluation of resin-based composite and glass ionomer cement restorations placed in primary teeth using the ART approach. J Am Dent Assoc, 137: 1529-1536.

[45] Frencken JE, Leal SC. (2010) The correct use of the Atraumatic Restorative Treatment (ART) approach. J Appl Oral Sci, 18: 1-4.

[46] Frencken JE, Makoni F, Sithole WD. (1998) ART restorations and glass ionomer sealants in Zimbabwe: survival after 3 years. Community Dent Oral Epidemiol, 26: 372-381.

[47] Frencken JE, Songpaisan Y, Phantumvanit P, Pilot T. (1994) An Atraumatic Restorative Treatment (ART) technique: evaluation after one year. Int Dent J, 44: 460-464.

[48] Frencken JE, Van't Hof MA, Van Amerongen WE, Holmgren CJ. (2004) Effectiveness of single-surface ART restorations in the permanent dentition: a meta-analysis. J Dent Res, 83: 120-123.

[49] Ho TF, Smales RJ, Fang DT. (1999) A 2-year clinical study of two glass ionomer cements used in the Atraumatic Restorative Treatment (ART) technique. Community Dent Oral Epidemiol, 27: 195-201.

[50] Holmgren CJ, Figueiredo M. (2009) Two decades of ART - Improving on success through further research. J Appl Oral Sci, 17 (sp. issue): 122-133.

[51] Prosser HJ, Wilson AD. (1979) Litho-ionomer cements and their technological applications. J Chem Technol Biotechnol, 29: 69-87.

[52] Barry TI, Clinton DJ, Wilson AD. (1979) The structure of a glass-ionomer cement and its relationship to the setting process. J Dent Res, 58: 1072-1079.

[53] Wasson EA, Nicholson JW. (1993) New aspects of the setting of glass-ionomer cements. J Dent Res, 72: 481-483.

[54] Wilson AD. (1996) Secondary reactions in glass-ionomer cements. J Mater Sci Lett, 15: 275-276.

[55] Wilson AD. (1974) Alumino-silicate polyacrylic acid and related cements. Br Polym J, 6: 165-179.

[56] Nomoto R, Komoriyama M, McCabe JF, Hirano S. (2004) Effect of mixing method on the porosity of encapsulated glass ionomer cement. Dent Mater, 20: 972-978.

[57] Walls AWG. (1986) Glass polyalkenoate (glass-ionomer) cements: a review. J Dent, 14: 231-246.

[58] Dahl BL, Tronstad L. (1976) Biological tests of an experimental glass ionomer (silicopolyacrylate) cement. J Oral Rahabil, 3: 19-24.

[59] Hanks CT, Anderson M, Craig RG. (1981) Cytotoxic effects of dental cements in two cell culture systems. J Oral Pathol, 10: 101-112.

[60] Meryon SD, Stephens PG, Browne RM. (1983) A comparison of the in vitro cytotoxicity of two glass ionomer cements. J Dent Res, 62: 769-773.

[61] Hume WR, Mount GJ. (1988) In vitro studies on the potential for pulpal cytotoxicity of glass-ionomer cements. J Dent Res, 67: 915-918.

[62] Kawahara T, Imanishi Y, Oshima H. (1979) Biological evaluation of glass ionomer cements. J Dent Res, 58: 1080-1086.

[63] Cooper IR. (1980) The response of the human dental pulp to glass ionomer cements. Int Endodont J, 13: 76-88.

[64] Plant CG, Browne RM, Knibbs PJ, Britton AS, Sorahan T. (1984) Pulpal effects of glass ionomer cements. Int Endodont J, 17: 51-59.

[65] Ucok M. (1986) Biological evaluation of glass ionomer cements. Int Endodont J, 19: 285-297.

[66] Tobias RS, Browne RM, Plant GC, Ingram DV. (1978) Pulpal response to a glass ionomer cement. Br Dent J, 144: 345-350.

[67] Nordenval KJ, Brannstrom M, Torstenson B. (1979) Pulpal reactions and microorganisms under ASPA and concise composite fillings. J Dent Child, 46: 449-453.

[68] Pameijer CH, Segal E, Richardson J. (1981) Pulpal response to a glass ionomer cement in primates. J Prosthet Dent, 46: 36-40.

[69] Garcia R, Charbeneau GT. (1981) Gingival tissue response to restoration of deficient cervical contours using a glass-ionomer material. A 12 month report. J Prosthet Dent, 46: 393-398.

[70] Hotz P, McLean JW, Sced I, Wilson AD. (1977) The bonding of glass ionomer cements to metal and tooth substrates. Br Dent J, 142: 41-47.

[71] Wilson AD, Prosser HJ, Powis DM. (1983) Mechanism of adhesion of polyelectrolyte cements to hydroxyapatite. J Dent Res, 62: 590-592.

[72] Ngo H, Mount GJ, Peters MC. (1997) A study of glass-ionomer cement and its interface with enamel and dentin using a low-temperature, high-resolution scanning electron microscopic technique. Quintessence Int, 28: 63-69.

[73] Nicholson JW, Aggarwal A, Czarnecka B, Limanowska-Shaw H. (2000) The rate of change of pH of lactic acid exposed to preliminary study of glass-ionomer dental cements. Biomaterials, 20: 1989-1993.

[74] Forsten L. (1998) Fluoride release and uptake by glass-ionomers and related materials and its clinical effect. Biomater, 19: 503-508.

[75] Tyas MJ. (1991) Cariostatic effect of glass ionomer cement: a five-year clinical study. Aust Dent J, 36: 236-239.

[76] Kidd EAM, Ricketts DNJ, Beighton D. (1996) Criteria for caries removal at the enamel-dentin junction: a clinical and microbiology study. Brit Dent J, 180: 287-291.

[77] ten Cate JM, van Duinen RNB. (1995) Hypermineralization of dentinal lesions adjacent to glass-ionomer cement restorations. J Dent Res, 74: 1266-1271.

[78] Wilson AD, Paddon JM, Crisp S. (1979) The hydration of denal cements. J Dent Res, 58: 1065-1071.

[79] Williams JA, Billington RW, Pearson GJ. (2002) The effect of the disc support system on biaxial tensile strength of a glass ionomer cement. Dent Mater, 18: 376-379.

[80] Akinmade AO, Nicholson JW. Poisson's ratio of glass-polyalkenoate ("glass-ionomer") cements determined by an ultrasonic pulse method. (1995) J Mater Sci Mater Med, 6: 483-485.

[81] Denisova LA, Maev RG, Poyurovskaya IY, Grineva TV, Denisov AF, Maeva EY, Bakulin EY. (2004) The use of acoustic microscopy to study the mechanical properties of glass-ionomer cement. Dental Materials, 20: 358-363.

[82] Xie D, Brantley WA, Culbertson BM, Wang G. (2000) Mechanical properties and microstructures of glass-ionomer cements. Dent Mater, 16: 129-138.

[83] Cefaly DFG, Franco EB, Mondelli RF, Francisconi PA, Navarro MF. (2003) Diametral tensile strength and water sorption of glass-ionomer cements used in Atraumatic Restorative Treatment. J Appl Oral Sci, 11: 96-101.

[84] Guggenberger R, May R, Stefan KP. (1998) New trends in glass ionomer chemistry. Biomater, 19: 479-483.

[85] Goldman M. (1985) Fracture properties of composite and glass ionomer dental restorative materials. J Biomed Mater Res, 19: 771-783.

[86] dos Reis RF, Borges PC. (2005) Alternative methodology for flexural strength testing in natural teeth. Braz Dent J, 16: 45-49.

[87] Kinney JH, Marshall SJ, Marshall GW. (2003) The mechanical properties of human dentin: a critical review and re-evaluation of the dental literature. Crit Rev Oral Biol Med, 14: 13-29.

[88] el Mowafy OM, Watts DC. (1986) Fracture toughness of human dentin. J Dent Res, 65: 677-681.

[89] Nalla RK, Kinney JH, Ritchie RO. (2003) Effect of orientation on the in vitro fracture toughness of dentin: the role of toughening mechanisms. Biomater, 24: 3955-3968.

[90] Davies RA, Ardalan S, Mu WH, Tian K, Farsaikiya F, Darvell BW, Chass GA. (2010) Geometric, electronic and elastic properties of dental silver amalgam γ-(Ag3Sn), γ1-(Ag2Hg3), γ2-(Sn8Hg) phases, comparison of experiment and theory. Intermetal, 18: 756-760.

[91] Greaves GN, Greer AL, Lakes RS, Rouxel T. (2011) Poisson's ratio and modern materials. Nature Mater, 10: 823-837.

[92] Williams JA, Billington RW. (1989) Increase in compressive strength of glass ionomer restorative materials with respect to time: a guide to their suitability for use in posterior primary dentition. J Oral Rehab, 16: 475-479.

[93] Mitra SB, Kedrowski BL. (1994) Long-term mechanical properties of glass ionomers. Dent Mater, 10: 78-82.

[94] Hill RG. (1993) The fracture properties of glass polyalkenoate cements as a function of cement age. J Mater Sci, 28: 3851-3858.

[95] Lloyd CH, Adamson M. (1987) The development of fracture toughness and fracture strength in posterior restorative materials. Dent Mater, 3: 225-231.

[96] Nicholson JW. (1998) Chemistry of glass-ionomer cements: a review. Biomater, 19: 485-494.

[97] Crisp S, Pringuer MA, Wardleworth D, Wilson AD. (1974) Reactions in glass ionomer cements: II. An infrared spectroscopic study. J Dent Res, 53: 1414-1419.

[98] Crisp S, Wilson AD. (1974) Reactions in glass ionomer cements: III. The precipitation reaction. J Dent Res, 53: 1420-1424.

[99] Hatton PV, Brook IM. (1992) Characterization of the ultrastructure of glass-ionomer (polyalkenoate) cement. Brit Dent, 173: 275-277.

[100] Crisp S, Wilson AD. (1976) Reactions in glass ionomer cements: V. Effect of incorporating tartaric acid in the cement liquid. J Dent Res, 55: 1023-1031.

[101] Darvell BW. Materials science for Dentistry. 8th edition, Hong Kong, 2006: 238-245.

[102] Wilson AD. (1996) A hard decade's work: steps of the invention of the glass-ionomer cement. J Dent Res, 75: 1723-1727.

[103] McLean JW, Wilson AD. (1977) The clinical development of the glass ionomer cement. III. The erosion lesion. Aus Dent J, 22: 190-195.

[104] Griffin S, Hill R. (1998) Influence of poly(acrylic acid) molar mass on the fracture properties of glass polyalkenoate cements. J Mater Sci, 33: 5383-5396.

[105] Wilson AD, Crisp S, Ferner AJ. (1976) Reactions in glass ionomer cements: IV. Effect of chelating comonomers on setting behavior. J Dent Res, 55: 489-495.

[106] Hill RG, Wilson AD. (1988) A rheological study of the role of additives on the setting of glass-ionomer cements. J Dent Res, 67: 1446-1450.

[107] Cook WD. (1983) Dental polyelectrolyte cements: III: Effect of additives on their rheology. Biomater, 4: 85-88.

[108] Wilson AD, Crisp S, Prosser HJ, Lewis BG, Merson SA. (1980) Aluminosilicate glasses for polyelectrolyte cements. Ind Eng Chem Prod Res Dev, 19: 263-270.

[109] Griffin SG, Hill RG. (2000) Influence of glass composition on properties of glass polyalkenoate cements. Part II: influence of phosphate content. Biomater, 21: 399-403.

[110] Zainuddin N, Karpukhina N, Hill RG, Law RV. (2009) A long-term study on the setting reaction of glass ionomer cements by ^{27}Al MAS-NMR spectroscopy. Dent Mater, 25: 290-295.

[111] Crisp S, Lewis BG, Wilson AD. (1977) Characterization of glass-ionomer cements. 3. Effect of polyacid concentration on the physical properties. J Dent, 5: 51-56.

[112] Kent BE, Lewis BG, Wilson AD. (1979) Glass ionomer cement formulations: I. The preparation of novel fluoroaluminosilicate glasses high in fluorine. J Dent Res, 58: 1607-1619.

[113] Moshaverinia A, Roohpour N, Chee WWL, Schricker SR. (2011) A review of powder modifications in conventional glass-ionomer dental cements. J Mater Chem, 21: 1319-1328.

[114] Crisp S, Lewis BG, Wilson AD. (1979) Characterization of glass ionomer cements. 5. The effect of the tartaric acid concentration in the liquid component. J Dent, 7: 304-312.

[115] Brandt B, Lohbauer U, Göken M, Durst K. (2010) The influence of particle size on the mechanical properties of dental glass ionomer cements. Adv Eng Mater, 12: B684-689.

[116] Prentice LH, Tyas MJ, Burrow MF. (2005) The effect of particle size distribution on an experimental glass-ionomer cement. Dent Mater, 21: 505-510.

[117] Gu YW, Yap AUJ, Cheang P, Kumar R. (2004) Spheroidization of glass powders for glass ionomer cements. Biomater, 25: 4029-4035.

[118] Wood D, Hill R. (1991) Structure-property relationships in ionomer glasses. Clin Mater 7: 301-312.

[119] Griffin SG, Hill RG. (2000) Influence of glass composition on properties of glass polyalkenoate cements. Part IV: influence of fluorine content. Biomater, 21: 693-698.

[120] Crisp S, Kent BE, Lewis BG, Ferner AJ, Wilson AD. (1980) Glass-ionomer cement formulations. II. The synthesis of novel polycarboxylic acids. J Dent Res, 59: 1055-1063.

[121] Crisp S, Ferner AJ, Lewis BG, Wilson AD. (1975) Properties of improved glass-ionomer cement formulations. J Dent, 3: 125-130.

[122] Wilson AD, Crisp S, Abel G. (1977) Characterization of glass-ionomer cements. 4. Effect of molecular weight on physical properties. J Dent, 5: 117-120.

[123] Prosser HJ, Powis DR, Wilson AD. (1986) Glass-ionomer cement of improved flexural strength. J Dent Res, 65: 146-148.

[124] Wilson AD, Hill RG, Warrens CP, Lewis BG. (1989) The influence of polyacid molecular weight on some properties of glass-ionomer cements. J Dent Res, 68: 89-94.

[125] Hill RG, Wilson AD, Warrens CP. (1989) The influence of poly(acylic acid) molecular weight on the fracture toughness of glass-ionomer cements. J Mater Sci, 24: 363-371.

[126] Stanton K, Hill R. (2009) The role of fluorine in the devitrification of SiO_2-Al_2O_3-P_2O_5-CaO-CaF_2 glasses. J Mater Sci, 35: 1911-1916.

[127] Reimer L, Kohl H. Transmission Electron Microscopy: Physics of Image Formation. 5th edition, Springer, Germany, 2008: 1-9.

[128] Meyer JC, Girit CO, Crommie MF, Zettl A. (2008) Imaging and dynamics of light atoms and molecules on graphene. Nature, 454: 319-322.

[129] Höhne G, Hemminger WF, Flammersheim HJ. Differential scanning calorimetry. 2nd edition, Springer, Germany, 2003: 1-16.

[130] Young AM, Sherpa A, Pearson G, Schottlander B, Waters DN. (2000) Use of Raman spectroscopy in the characterisation of the acid–base reaction in glass-ionomer cements. Biomaterials, 21: 1971-1979.

[131] O'Neill IK, Prosser HJ, Richards CP, Wilson AD. (1982) NMR spectroscopy of dental materials. I. 31P studies on phosphate/bonded cement liquids. J Biomed Mater Res, 16: 39-49.

[132] Pires R, Nunes TG, Abrahams I, Hawkes GE, Morais CM, Fernandez C. (2004) Stray-field imaging and multinuclear magnetic resonance spectroscopy studies on the setting of a commercial glass-ionomer cement. J Mater Sci Mater Med, 15: 201-208.

[133] Stamboulis A, Matsuya S, Hill RG, Law RV, Udoh K, Nakagawa M, Matsuya Y. (2006) MAS-NMR spectroscopy studies in the setting reaction of glass ionomer cements. J Dent, 34: 574-581.

[134] Munhoz T, Karpukhina N, Hill RG, Law RV, De Almeida LH. (2010) Setting of commercial glass ionomer cement Fuji IX by ^{27}Al and ^{19}F MAS-NMR. J Dent, 38: 325-330.

[135] Matsuya S, Maeda T, Ohta M. (1996) IR and NMR analysis of hardening and materuration of glass-ionomer cement. J Dent Res, 75: 1920-1927.

[136] Pires RA, Nunes TG, Abrahams I, Hawkes GE. (2008) The role of aluminium and silicon in the setting chemistry of glass ionomer cements. J Mater Sci Mater Med, 19: 1687-1692.

[137] Prosser HJ, Richards CP, Wilson AD. (1982) NMR spectroscopy of dental materials. II. The role of tartaric acid in glass-ionomer cements. J Biomed Mater Res, 16: 431-445.

[138] Maeda T, Matsuya S, Ohta M. (1998) Effects of CaF2 addition on the structure of CaO–Al2O3–SiO2 glasses. Dent Mater J, 17: 104-114.

[139] Stamboulis A, Law RV, Hill RG. (2004) Characterisation of commercial ionomer glasses using magic angle nuclear magnetic resonance (MAS-NMR). Biomater, 25: 3907-3913.

[140] Hill RG, Stamboulis A, Law RV. (2006) Characterisation of fluorine containing glasses by 19F, 27Al, 29Si and 31P MAS-NMR spectroscopy. J Dent, 34: 525-532.

[141] Matsuya S, Stamboulis A, Hill RG, Law RV. (2007) Structural characterisation of ionomer glasses by multinuclear solid state MAS-NMR spectroscopy. J Non-Cryst Sol, 353: 237-243.

[142] Pires RA, Abrahams I, Nunes TG, Hawkes GE. (2009) The role of alumina in aluminoborosilicate glasses for use in glass-ionomer cements. J Mater Chem, 19: 3652-3660.

[143] Nicholson JW, Brookman PJ, Lacy OM, Wilson AD. (1988) Fourier transform infrared spectroscopic study of the role of tartaric acid in glass-ionomer dental cements. J Dent Res, 67: 1451-1454.

[144] Darvell BW. (1990) Uniaxial compression tests and the validity of indirect tensile strength. J Mater Sci, 25: 757-780.

[145] McCabe JF, Watts DC, Wilson HJ, Worthington HV. (1990) An investigation of test-house variability in the mechanical testing of dental materials and the statistical treatment of results. J Dent, 18: 90-97.

[146] Kelly JR. (1995) Perspectives on strength. Dent Mater, 11: 103-110.

[147] Mitchell CA, Douglas WH, Cheng YS. (1999) Fracture toughness of conventional, resin-modified glass–ionomer and composite luting cements. Dent Mater, 15: 7-13.

[148] Dowling AH, Fleming GJP, McGinley EL, Addison O. (2012) Improving the standard of the standard for glass ionomers: An alternative to the compressive fracture strength test for consideration? J Dent, 40: 189-201.

[149] Bonilla ED, Mardirossian G, Caputo AA. (2000) Fracture toughness of various core build-up materials. J Prosthod, 9: 14-18.

[150] Beatty MW, Pidaparti RMV. (1993) Elastic and fracture properties of dental direct filling materials. Biomater, 14: 999-1002.

[151] Lloyd CH, Butchart DGM. (1990) The retention of core composites, glass ionomers, and cermets by a self-threading dentin pin: The influence of fracture toughness upon failure. Dent Mater, 6: 185-188.

[152] Miyazaki M, Moore BK, Onose H. (1996) Effect of surface coatings on flexural properties of glass ionomers. Eur J Oral Sci, 104: 600-604.

[153] Bapna MS, Gadia CM, Drummond JL. (2002) Effects of aging and cyclic loading on the mechanical properties of glass ionomer cements. Eur J Oral Sci, 110: 330-334.

[154] Pidaparti RMV, Beatty MW. (1995) Fracture toughness determination of dental materials by laboratory testing and finite element models. J Biomed Mater Res, 29: 309-314.

[155] Ryan AK, Orr JF, Mitchell CA. (2001) A comparative evaluation of dental luting cements by fracture toughness tests and fractography. J Eng Med, 215: 65-73.

[156] Hill RG, Wilson AD, Warrens CP. (1989) The influence of poly(acylic acid) molecular weight on the fracture toughness of glass-ionomer cements. J Mater Sci, 24: 363-371.

[157] Lloyd CH, Mitchell L. (1984) The fracture toughness of tooth coloured restorative materials. J Oral Rehab, 11: 257-272.

[158] Lucksanaesombool P, Higgs WAJ, Higgs RJED, Swain MV. (2002) Time dependence of the mechanical properties of GICs in simulated physiological conditions. J Mater Sci Mater Med, 13: 745-750.

[159] Knobloch LA, Kerby RE, Seghi R, Berlin JS, Lee JS. (2000) Fracture toughness of resin-based luting cement. J Prosthet Dent, 83: 204-209.

[160] Yamazaki T, Schricker SR, Brantley WA, Culbertson BM, Johnston W. (2006) Viscoelastic behaviour and fracture toughness of six glass-ionomer cements. J Prosthet Dent, 96: 266-272.

[161] Lawn BR, Deng Y, Thompson VP. (2001) Use of contact testing in the characterization and design of all-ceramic crownlike layer structures: a review. J Prosthet Dent, 86: 495-510.

[162] Lawn BR, Deng Y, Miranda P, Pajares A, Chai H, Kim DK. (2002) Overview: damage in brittle layer structures from concentrated loads. J Mater Res, 17: 3019-3036.

[163] Kelly JR. (1999) Clinically relevant approach to failure testing of all-ceramic restorations. J Prosthet Dent, 81: 652-661.

[164] Kelly JR, Giordano R, Pober R, Cima MJ. (1990) Fracture surface analysis of dental ceramics: clinically failed restorations. Int J Prosthodont, 3: 430-440.

[165] Wang Y, Darvell BW. (2007) Failure mode of dental restorative materials under Hertzian indentation. Dent Mater, 23: 1236-1244.

[166] Wang Y, Darvell BW. (2008) Failure behaviour of glass ionomer cement under Hertzian indentation. Dent Mater, 24: 1223-1229.

[167] Wang Y, Darvell BW. (2009) Hertzian load-bearing capacity of a ceramic-reinforced glass ionomer cement stored wet and dry. Dent Mater, 25: 952-955.

[168] Quinn JB, Quinn GD. (2010) Material properties and fractography of an indirect dental resin composite. Dent Mater, 26: 589-599.

[169] Hull D. Fractography: Observing, measuring and interpreting fracture surface topography. Cambridge: University Press, Cambridge, 1999: 1-6.

[170] Scherrer SS, Kelly JR, Quinn GD, Xu K. (1999) Fracture toughness of a dental porcelain determined by fractographic analysis. Dent Mater, 15: 342-348.

[171] Stock SR. Microcomputed tomography: methodology and applications. Boca Raton: CRC press; 2008: 1-6.

[172] Landis EN, Nagy EN, Keane DT. (2003) Microstructure and fracture in three dimensions. Eng Fract Mech, 70: 911-925.

[173] Sinnett-Jones PE, Browne M, Ludwig W, Buffiere JY, Sinclair I. (2005) Microtomography assessment of failure in acrylic bone cement. Biomater, 26: 6460-6466.

[174] Dobo-Nagy C, Keszthelyi G, Szabo J, Sulyok P, Ledeczky G, Szabo J. (2000) A computerized method for mathematical description of three-dimensional root canal axis. J Endodon, 26: 639-643.

[175] Mayo CV, Montgomery S, Rio C. (1986) A computerized method for evaluating root canal morphology. J Endodon, 12: 2-7.

[176] Berutti E. (1993) Computerized analysis of the instrumentation of the root canal system. J Endodon, 19: 236-238.

[177] Nielsen RB, Alyassin AM, Peters DD, Carnes DL, Lancaster J. (1995) Microcomputed tomography: an advanced system for detailed endodontic research. J Endodon, 21: 561-568.

[178] Bauman MA, Doll GM. (1997) Spatial reproduction of the root canal system by magnetic resonance microscopy. J Endodon, 23: 49-51.

[179] Dowker SE, Davis GR, Elliot JC. (1997) X-ray microtomography: non-destructive three-dimensional imaging for in vitro endodontic studies. Oral Surg OralMed Oral Pathol Oral Radiol Endod, 83: 510-516.

[180] Magne P, Tan DT. (2008) Incisor compliance following operative procedures: A rapid 3-D finite element analysis using micro-CT data. J Adhes Dent, 10: 49-56.

[181] Ichim I, Li Q, Loughran J, Swain MV, Kieser J. (2007) Restoration of non-carious cervical lesions. Part I. Modelling of restorative fracture. Dent Mater, 23: 1553-1561.

[182] Ichim IP, Schmidlin PR, Li Q, Kieser JA, Swain MV. (2007) Restoration of non-carious cervical lesions. Part II. Restorative material selection to minimise fracture. Dent Mater, 23: 1562-1569.

[183] Simmons JJ. (1983) The miracle mixture: glass ionomer and amalgam alloy powder. TX Dent J, 1: 6-9.

[184] Sarkar NK. (1999) Metal-matrix interface in reinforced glass ionomers. Dent Mater, 15: 421-425.

[185] McLean JW, Gasser O. Powdered dental material and process for the preparation thereof. US Patent No. 4527979, 1985.

[186] Kerby RE, Bleiholder RF. (1991) Physical-properties of stainless steel and silver-reinforced glass-ionomer cements. J Dent Res, 70: 1358-1361.

[187] Neve AD, Piddock V, Combe EC. (1992) Development of novel dental cement. I. Formation of aluminoborate glasses. Clin Mater, 9: 13-20.

[188] Neve AD, Piddock V, Combe EC. (1992) Development of novel dental cement. II. Cement properties. Clin Mater, 9: 21-29.

[189] Neve AD, Piddock V, Combe EC. (1993) The effect of glass heat treatment on the properties of a novel polyalkenoate cement. Clin Mater, 12: 113-115.

[190] Darling M. Hill R. (1994) Novel polyakenoate (glass ionomer) dental cements based on zinc silicate glasses. Biomater, 15: 299-306.

[191] Deb S, Nicholson JW. (1999) The effect of strontium oxide in glass-ionomer cements. J Mater Sci Mater Med, 10: 471-474.

[192] Lohbauer U, Walker J, Nikolaenko S, Werner J, Clare A, Petschelt A, Greil P. (2003) Reactive fibre reinforced glass ionomer cements. Biomater, 24: 2901-2907.

[193] Lohbauer U, Frankenberger R, Clare A, Petschelt A, Greil P. (2004) Toughening of dental glass ionomer cements with reactive glass fibres. Biomater, 25: 5217-5225.

[194] Yli-Urpo H, Narhi M, Narhi T. (2005) Compound changes and tooth mineralization effects of glass ionomer cements containing bioactive glass (S53P4), an in vivo study. Biomater, 26: 5934-5941.

[195] Yli-Urpo H, Lassila LVJ, Narhi T, Vallittu PK. (2005) Compressive strength and surface characterization of glass ionomer cements modified by particles of bioactive glass. Dent Mater, 21: 201-209.

[196] Lucas ME, Arita K, Nishino M. (2002) Flexural strength of hydroxyapatite-added glass ionomer cement. J Dent Res, 81(SI): A36.

[197] Arita K, Lucas ME, Nishino M. (2003) The effect of adding hydroxyapatite on the flexural strength of glass ionomer cement. Dent Mater J, 22: 126-136.

[198] Lucas ME, Arita K, Nishino M. (2003) Toughness, bonding and fluoride-release properties of hydroxyapatite-added glass ionomer cement. Biomater, 24: 3787-3794.

[199] Moshaverinia A, Ansari S, Moshaverinia M, Roohpour N, Darr J, Rehman I. (2008) Effects of incorporation of hydroxyapatite and fluoroapatite nanobioceramics into conventional glass ionomer cements (GIC). Acta Biomater, 4: 432-440.

[200] Gu YW, Yap AUJ, Cheang P, Khor KA. (2005) Effects of incorporation of HA/ZrO2 into glass ionomer cement (GIC). Biomater, 26: 713-720.

[201] Gu YW, Yap AUJ, Cheang P, Koh YL, Khor KA. (2005) Development of zirconia-glass ionomer cement composites. J Non-Cryst Solids, 351: 508-514.

[202] Culbertson BM. (2006) New polymeric materials for use in glass-ionomer cements. J Dent, 34: 556-565.

[203] Culbertson BM, Xie D, Thakur A. (1999) New matrix resins for glass polyalkenoates or glass-ionomers with pendant amino acid residues. J Macromol Sci Pure Appl Chem, A36: 681-696.

[204] Culbertson BM, Xie D, Thakur A. (1998) Amino acid functionalized ionomeric materials in biomedical applications. Macromol Symp, 131: 11-18.

[205] Culbertson BM, Dotrong MH. (2000) Preparation and evaluation of acrylic acid, itaconic acid, and N-methacryloylglutamic acid copolymers for use in glass-ionomer type dental restoratives. J Macromol Sci Pure Appl Chem, 37: 419-431.

[206] Kao EC, Culbertson BM, Xie D. (1996) Preparation of glass ionomer cement using N-acryloyl-substituted amino acid monomers - Evaluation of physical properties. Dent Mater, 12: 44-51.

[207] Xie D, Culbertson BM, Johnston WM. (1998) Improved flexural strength of N-vinyl-pyrrolidone modified acrylic acid copolymers for glass-ionomers. J Macromol Sci Pure Appl Chem, A35: 1615-1629.

[208] McLean JW, Nicholson JW, Wilson AD. (1994) Proposed nomenculture for glass-ionomer dental cements and related materials. Quint Int, 25: 587-589.

[209] Mitra SB. (1991) Adhesion to dentine and physical properties of a light-cured glass-ionomer liner/base. J Dent Res, 70: 72-74.

[210] Mitra SB. (1991) In vitro fluoride release from a light-cured glass-ionomer liner/base. J Dent Res, 70: 75-78.

[211] Forss H. (1993) Release of fluoride and other elements from light-cured glass ionomers in neutral and acidic conditions. J Dent Res, 72: 1257-1262.

[212] Mathis RS, Ferracane JL. (1989) Properties of a glass-ionomer/resin-composite hybrid material. Dent Mater, 5: 355-358.

[213] Attin T, Buchalla W, Kielbassa AM, Hellwig E. (1995) Curing shrinkage and volumetric changes of resin-modified glass ionomer restorative material. Dent Mater, 11: 359-362.

[214] Nicholson JW, Anstice HM, McLean JW. (1992) A preliminary report on the effect of storage in water on the properties of commercial light-cured glass-ionomer cements. Brit Dent J, 173: 98-101.

[215] Nicholson JW, Czarnecka B. (2008) The biocompatibility of resin-modified glass-ionomer cements for dentistry. Dent Mater, 24: 1702-1708.

[216] Nicholson JW. (1994) The physical chemistry of light-curable glass-ionomers. J Mater Sci Mater Med, 5: 119-122.

[217] Ellis J, Wilson AD. (1990) Polyphosphonate cements: a new class of dental materials. J Mater Sci Lett, 9: 1058-1060.

[218] Ellis J, Wilson AD. (1991) A study of the cements formed between metal oxides and polyvinylphosphonic acid. Polym Int, 24: 221-228.

[219] Ellis J, Wilson AD. (1992) The formation and properties of metal-oxide poly(vinylphosphonic aid) cements. Dent Mater, 8: 79-84.

[220] Braybrook JH, Nicholson JW. (1993) Incorporation of crosslinking agents into poly(vinyl phosphonic acid) as a route to glass-polyalkenoate cements of improved compressive strength. J Mater Chem, 3: 361-365.

[221] O'Donnell MD, Hill RG, Karpukhina N, Law RV. (2011) Real time neutron diffraction and NMR of the Empress II glass-ceramic system. Dent Mater, 27: 990-996;

[222] Sears VF. (1992) Neutron scattering lengths and cross sections. Neutron News, 3: 26-37.

[223] Newville M. (1969) Compilation of x-ray cross sections based on the tables of W.H. McMaster, N. Kerr Del Grande, J.H. Mallett, and J.H. Hubbell, Lawrence Livermore National Laboratory Report UCRL-50174 Section II revision I.

[224] ISIS webpage: http://www.isis.stfc.ac.uk/

[225] Soper AK. Gudrun and GudrunX - programs for correcting raw neutron and x-ray diffraction data to differential scattering cross section. ISIS, Rutherford Appleton Laboratory, UK, 2010.

[226] Mayers J, Abdul-Redah T. (2004) The measurement of anomalous neutron inelastic cross-sections at electronvolt energy transfers. J Phys Condens Matter, 16: 4811-4832.

[227] Andreani C, Colognesi D, Mayers J, Reiter GF, Senesi R. (2005) Measurement of momentum distribution of light atoms and molecules in condensed matter systems using inelastic neutron scattering. Adv Phys, 54: 377-469.

[228] Krzystyniak M, Adams MA, Lovell A, Skipper NT, Bennington SM, Mayers J, Fernandez-Alonso F. (2011) Probing the binding and spatial arrangement of molecular hydrogen in porous hosts via neutron Compton scattering. Faraday Discuss, 151: 171-197.

[229] Mayers J, Adams MA. (2011) Calibration of an electron volt neutron spectrometer. Nucl Inst Method Phys Res A, 625: 47-56.

[230] Tardocchia M, Gorini G, Pietropaolo A, Andreani C, Senesi R, Rhodes N, Schooneveld EM. (2004) YAP scintillators for resonant detection of epithermal neutrons at pulsed neutron sources. Rev Sci Instrum, 75: 4880-4890.

[231] Andreani C, Pietropaolo A, Senesi R, Gorini G, Perelli-Cippo E, Tardocchi M, Rhodes N, Schooneveld EM. (2004) A resonant detector for high-energy inelastic neutron scattering experiments. Appl Phys Lett, 85: 5454-5456.

[232] Schooneveld EM, Mayers J, Rhodes NJ, Pietropaolo A, Andreani C, Senesi R, Gorini G, Perelli-Cippo E, Tardocchi M. (2006) Foil cycling technique for the VESUVIO spectrometer operating in the resonance detector configuration. Rev Sci Instrum, 77: 095103.

[233] Mayers J. (2011) Calculation of background effects on the VESUVIO eV neutron spectrometer. Meas Sci Technol, 22: 015903.

[234] Mayers J, Fielding AL, Senesi R. (2002) Multiple scattering in deep inelastic neutron scattering: Monte Carlo simulations and experiments at the ISIS eVS inverse geometry spectrometer. Nucl Inst Methods A, 481; 454-463.

[235] Chatzidimitriou-Dreisman CA, Abdul-Redah T, Krzystyniak M. (2005) Anomalous neutron Compton scattering from molecular hydrogen. Phys Rev B, 72: 054123.

[236] Chatzidimitriou-Dreisman CA, Abdul-Redah T, Streffer RMF, Mayers J. (1997) Anomalous deep inelastic neutron scattering from liquid H_2O-D_2O: Evidence of nuclear quantum entanglement. Phys Rev Lett, 79: 2839-2842.

[237] Pietropaolo A, Senesi R, Andreani C, Botti A, Ricci MA, Bruni F. (2008) Excess of proton mean kinetic energy in supercooled water. Phys Rev Lett, 100: 127802.

[238] Pantalei C, Pietropaolo A, Senesi R, Imberti S, Andreani C, Mayers J, Burnham C, Reiter G. (2008) Proton momentum distribution in liquid water from room temperature to the supercritical phase. Phys Rev Lett, 100: 177801.

[239] Reiter G, Burnham C, Homouz D, Platzman PM, Mayers J, Abdul-Redah T, Moravsky AP, Li JC, Loong CK, Kolesnikov AI. (2006) Anomalous behaviour of proton zero point motion in water confined in carbon nanotubes. Phys Rev Lett, 97: 247801.

[240] Senesi R, Pietropaolo A, Bocedi A, Pagnotta SE, Bruni F. (2007) Proton momentum distribution in a protein hydration shell. Phys Rev Lett, 98: 138102.

[241] Senesi R, Andreani C, Colognesi D, Cunsolo A, Nardone M. (2001) Deep-inelastic neutron scattering determination of the single-particle kinetic energy in solid and liquid ^{3}He. Phys Rev Lett, 86: 4584-4587.

[242] Colognesi D, Andreani C, Senesi R. (2000) Single-particle mean kinetic energy in low-density supercritical ^{4}He. Europhys Lett, 50: 202-208.

[243] Mayers J, Albergamo F, Timms DN. (2000) Measurements of the atomic kinetic energy of ^{4}He close to the superfluid transition. Physica B, 276: 811-813.

[244] Mayers J, Andreani C, Colognesi D. (1997) Measurement of the kinetic energy in ^{4}He through the superfluid transition by very high-energy neutron scattering. J Phys Condens Matter, 9: 10639-10649.

[245] Seel AG, Sartbaeva A, Mayers J, Ramirez-Cuesta AJ, Edwards PP. (2011) Neutron Compton scattering investigation of sodium hydride: From bulk material to encapsulated nanoparticulates in amorphous silica gel. J Chem Phys, 134: 114511.

[246] Gersten JI, Smith FW. The physics and chemistry of materials. John Wiley & Sons, Inc. New-York, 2001: 77-78.

[247] Bowron DT, Soper AK, Jones K, Ansell S, Birch S, Norris J, Perrott L, Riedel D, Rhodes NJ, Wakefield SR, Botti, A, Ricci MA, Grazzi F, Zoppi M. (2010) NIMROD: the near and intermediate range order diffractometer of the ISIS second target station. Rev Sci Instru, 81: 033905.

[248] Keen DA. (2001) A comparison of various commonly used correlation functions for describing total scattering. Appl Crystallograph, 34: 172-177.

[249] Wilmink G, Grundt J. (2011) Invited review article: current state of research on biological effects of terahertz radiation. J Infrared Milli Terahz Waves, 32: 1074-1122.

[250] Sirtori C. (2002) Applied physics: bridge for the terahertz gap. Nature, 417: 132-133.

[251] Hu BB, Nuss MC. (1995) Imaging with terahertz waves. Optics Lett, 20: 1716-1718.

[252] McIntosh AI, Yang B, Goldup SM, Watkinson M, Donnan RS. (2012) Terahertz spectroscopy: a powerful new tool for the chemical sciences? Chem Soc Rev, 41: 2072-2082.

[253] Nagatsuma T. (2011) Terahertz technologies: present and future. IEICE Electron Express, 8: 1127-1142.

[254] Varberg TD, Evenson KM. (1993) Laser spectroscopy of carbon-monoxide - a frequency reference for the far-infrared. IEEE Trans Instrum Meas, 42: 412-414.

[255] Drouin BJ, Maiwald FW. (2006) Extended THz measurements of nitrous oxide, N_2O. J Mol Spectrosc, 236: 260-262.

[256] Drouin BJ, Pearson JC, Walters A, Lattanzi V. (2006) THz measurements of propane. J Mol Spectrosc, 240: 227-237.

[257] Strachan CJ, Rades T, Newnham DA, Gordon KC, Pepper M, Taday PF. (2004) Using terahertz pulsed spectroscopy to study crystallinity of pharmaceutical materials. Chem Phys Lett, 390: 20-24.

[258] Ning L, Shen J, Jinhai S, Laishun L, Xu X, Lu M, Yan J. (2005) Study on the THz spectrum of methamphetamine. Opt Express, 13: 6750-6755.

[259] Chen YQ, Liu HB, Deng YQ, Schauki, D, Fitch MJ, Osiander R, Dodson C, Spicer JB, Shur M, Zhang XC. (2004) THz spectroscopic investigation of 2,4-dinitrotoluene. Chem Phys Lett, 400: 357-361.

[260] Li RY, Zeitler JA, Tomerini D, Parrott EP, Gladden LF, Day GM. (2010) A study into the effect of subtle structural details and disorder on the terahertz spectrum of crystalline benzoic acid. Phys Chem Chem Phys, 12: 5329-5340.

[261] Zeitler JA, Kogermann K, Rantanen JT, Rades T, Taday PF, Pepper M, Aaltonen J, Strachan CJ. (2007) Drug hydrate systems and dehydration processes studied by terahertz pulsed spectroscopy. Int J Pharm, 334: 78-84.

[262] Allis DG, Fedor AM, Korter TM, Bjarnason JE, Brown ER. (2007) Assignment of the lowest-lying THz absorption signatures in biotin and lactose monohydrate by solid-statedensity functional theory. Chem Phys Lett, 440: 203-209.

[263] Hakey PM, Hudson MR, Allis DG, Ouellette W, Korter TM. (2009) Examination of phencyclidine hydrochloride via cryogenic terahertz spectroscopy, solid-state density functional theory, and X-ray diffraction. J Phys Chem A, 113: 13013-13022.

[264] King MD, Buchanan WD, Korter TM. (2011) Identification and quantification of polymorphism in the pharmaceutical compound diclofenac acid by terahertz spectroscopy and solid-state density functional theory. Anal Chem, 83: 3786-3792.

[265] Wittlin A, Genzel L, Kremer F, Häseler S, Poglitsch A, Rupprecht A. (1986) Far-infrared spectroscopy on oriented films of dry and hydrated DNA.Phys Rev A, 34: 493-500.

[266] Markelz AG, Roitberg A, Heilweil EJ. (2000) Pulsed terahertz spectroscopy of DNA, bovine serum albumin and collagen between 0.1 and 2.0 THz. Chem Phys Lett, 320: 42-48.

[267] Yada H, Nagai M, Tanaka K. (2009) The intermolecular stretching vibration mode in water isotopes investigated with broadband terahertz time-domain spectroscopy. Chem Phys Lett, 473: 279-283.

[268] Heugen U, Schwaab G, Bründermann E, Heyden M, Yu X , Leitner DM, Havenith M. (2006) Solute-induced retardation of water dynamics probed directly by terahertz spectroscopy. Proc Natl Acad Sci USA, 103: 12301-12306.

[269] Zeitler JA, Taday PF, Gordon KC, Pepper M, Rades T. (2007) Solid-state transition mechanism in carbamazepine polymorphs by time-resolved terahertz spectroscopy. Chem Phys Chem, 8: 1924-1927.

[270] Nguyen KL, Friscic T, Day GM, Gladden LF, Jones W. (2007) Terahertz time-domain spectroscopy and the quantitative monitoring of mechanochemical cocrystal formation. Nature Mater, 6: 206-209.

[271] Rosenblueth A, Wiener N. (1945) The role of models in science. Phil Sci, 12: 316-321.

[272] Leach AR. Molecular modelling: Principles and applications. Pearson Education Limited, Essex, 2001: 1-8.

[273] Simons S. Introduction to the principles of quantum mechanics. Logos Press Limited, London, 1968: 1-30.

[274] Engel T, Reid P. Physical chemistry. Pearson, Benjamin Cummings, San-Francisco, 2005: 614-615.

[275] Tian KV, Nagy PM, Chass GA, Fejerdy P, Nicholson JW, Csizmadia IG, Dobó-Nagy C. (2012) Qualitative assessment of microstructure and Hertzian indentation failure in biocompatible glass ionomer cements. J Mater Sci Mater Med, 23: 677-685.

[276] Soper AK, Howells WS, Hannon AC. ATLAS - analysis of time-of-flight diffraction data from liquid and amorphous samples. RAL technical report, RAL-89-046, 1989.

[277] Soper AK, Luzar A. (1992) A neutron diffraction study of dimethyl sulphoxide-water mixtures. J Chem Phys, 97: 1320.

[278] Frisch MJ, Trucks GW, Schlegel HB, Scuseria GE, Robb MA, Cheeseman JR, Scalmani G, Barone V, Mennucci B, Petersson GA, Nakatsuji H, Caricato M., Li X, Hratchian HP, Izmaylov AF, Bloino J, Zheng G, Sonnenberg JL, Hada M., Ehara M, Toyota K, Fukuda R, Hasegawa J, Ishida M, Nakajima T, Honda Y, Kitao O, Nakai H, Vreven T, Montgomery JA Jr, Peralta JE, Ogliaro F, Bearpark M., Heyd JJ, Brothers E, Kudin KN, Staroverov VN, Kobayashi R, Normand J, Raghavachari K, Rendell A, Burant JC, Iyengar SS, Tomasi J, Cossi M, Rega N, Millam NJ, Klene M, Knox JE, Cross JB, Bakken V, Adamo C, Jaramillo J, Gomperts R, Stratmann RE, Yazyev O, Austin AJ, Cammi R, Pomelli C, Ochterski JW, Martin RL, Morokuma K, Zakrzewski VG, Voth GA, Salvador P, Dannenberg JJ, Dapprich S, Daniels AD, Farkas Ö, Foresman JB, Ortiz JV, Cioslowski J, Fox DJ. Gaussian 09, Revision A.01, Gaussian, Inc., Wallingford CT, 2009.

[279] Becke AD. (1993) Density-functional thermochemistry. III. The role of exact exchange. J Chem Phys, 98: 5648-5652.

[280] Sosa C, Andzelm J, Elkin BC, Wimmer E, Dobbs KD, Dixon DA. (1992) A local density functional Study of the structure and vibrational frequencies of molecular transition-metal compounds. J Phys Chem, 96: 6630-6636.

[281] Wolinski K, Hinton JF, Pulay P. (1990) Efficient implementation of the Gauge-Independent Atomic Orbital method for NMR chemical shift calculations. J Am Chem Soc, 112: 8251-8260.

[282] Head-Gordon M, Pople JA, Frisch MJ. (1988) MP2 energy evaluation by direct methods. Chem Phys Lett, 153: 503-506.

[283] Reiter GF, Mayers J, Noreland J. (2002) Momentum-distribution spectroscopy using deep inelastic neutron scattering. Phys Rev B, 65: 104305.

[284] Wang Y, Darvell BW. (2010) Interactive effect of indenter size and sample thickness in Hertzian indentation test. Dent Mater, 26: 539-544.

[285] Landis E, Keane DT. (1999) X-ray microtomography for fracture studies in cement-based materials. Development in X-ray Tomography II. Bonse. Bellingham, WA. SPIE. SPIE Proc Vol 3772: 105-113.

[286] Kaplan AE, Williams J, Billington RW, Braden M, Pearson GJ. (2004) Effects of variation in particle size on biaxial flexural strength of two conventional glass-ionomer cements. J Oral Rehab, 31: 373-378.

[287] Crisp S, Wilson AD. (1973) Formation of glass ionomer cement based on an ion-leachable glass and polyacrylic acid. J Appl Chem Biotechnol, 23: 811-815.

[288] Reiter G, Li GC, Mayers J, Abdul-Redah T, Platzman P. (2004) The proton momentum distribution in water and ice. Braz J Phys, 34: 142-147.

[289] Greaves GN, Sen S. (2007) Inorganic glasses, glass-forming liquids and amorphizing solids. Adv Phys, 56: 1-166.

[290] Rafferty A, Hill R, Wood D. (2000) Amorphous phase separation of ionomer glasses. J Mater Sci, 35: 3863-3869.

[291] Gu YW, Fu YQ. (2004) Heat treatment and thermally induced crystallization of glass for glass ionomer cement. Thermalchim Acta, 423: 107-112.

[292] Boyd D, Towler MR, Watts S, Hill RG, Wren AW, Clarkin OM. (2008) The role of Sr^{2+} on the structure and reactivity of SrO-CaO-ZnO-SiO_2 ionomer glasses. J Mater Sci Mater Med, 19: 953-957.

[293] Greaves GN, Meneau F, Majérus O, Jones DG, Taylor J. (2005) Identifying the vibrations that destabilize crystals and characterizes the glassy state. Science, 308: 1299-1302.

[294] Lewandowski, J. J. Wang, W. H. & Greer, A. L. (2005) Intrinsic plasticity or brittleness of metallic glasses. Phil Mag Lett, 85: 77-87.

[295] Wilson AD, Crisp S, Paddon JM. (1981) The hydration of a glass-ionomer (ASPA) cement. Brit Polym J, 13: 66-70.

DOI:10.14753/SE.2014.1974

10 LIST OF PUBLICATIONS

The candidate's publications related to the content of this dissertation:

1. **Tian KV**, Nagy PM, Chass GA, Fejerdy P, Nicholson JW, Csizmadia IG, Dobó-Nagy C. (2012) Qualitative assessment of microstructure and Hertzian indentation failure in biocompatible glass ionomer cements. J Mater Sci Mater Med, 23: 677-685.

2. Davies RA, Ardalan S, Mu WH, **Tian K**, Farsaikiya F, Darvell BW, Chass GA. (2010) Geometric, electronic and elastic properties of dental silver amalgam γ-(Ag3Sn), γ1-(Ag2Hg3), γ2-(Sn8Hg) phases, comparison of experiment and theory. Intermetallics, 18 : 756-760.

The candidate's other publications :

1. **Tian K**, Darvell BW. (2010) Determination of flexural modulus of elasticity of orthodontic archwires. Dent Mater, 26: 821-829.

DOI:10.14753/SE.2014.1974

11 ACKNOWLEDGEMENT

I would like to thank my supervisor, Dr. Dobó Nagy Csaba, for his support, especially the leniency and independence he gave me.

I am truly grateful to professor Neville Greaves of Aberystwyth University and professor Chass Gregory of Queen Mary University of London for their dedication, valuable advice and guidance. CG is thanked for help with calculations. I would also like to thank professor Yue Yuanzheng of Aalborg University for accommodating my visit to his department and assistance with DSC experiments as well as helpful discussions.

Professor John Nicholson of St. Mary's University College is thanked for generous donation of samples and helpful discussions. Dr. Jerry Mayers and Dr. Daniel Bowron from ISIS pulsed neutron source are acknowledged for their assistance with neutron experiments, as well as helpful discussions. Dr. Yang Bin of University of Bolton, Dr. Alexander McIntosh and Dr. Robert Donnan of Queen Mary University of London are acknowledged for assistance with THz experiments. Dr. Jibran Khaliq is thanked for help with TEM imaging. Tóbiás Edit, Szabó Bence, Al-Katib Kamil and Gimesi Brigitte of Semmelweis University, and Budapest University of Technology and Economics Materials laboratory staff Mark and Nagy Peter are acknowledged for technical support.

Thanks are extended to professor Csizmadia Imre of University of Toronto, professor Fang Decai of Beijing Normal University and professor Lindsay Greer of University of Cambridge for useful discussions.

Last but not least I would like to thank my family for their unmatched love, commitment and selfless support. Without these I would not have completed this work. You two are the inspiration for everything I do.